

**Recent advances in MOF-based photocatalysis:  
environmental remediation under visible light**

Journal:	<i>Inorganic Chemistry Frontiers</i>
Manuscript ID	QI-REV-09-2019-001120.R1
Article Type:	Review Article
Date Submitted by the Author:	02-Oct-2019
Complete List of Authors:	Wang, Qi; School of Environment Sciences and Engineering, Zhejiang Gongshang University, Gao, Qiaoyuan; School of Environment Sciences and Engineering, Zhejiang Gongshang University, Al-Enizi, Abdullah; King Saud University, Chemistry Nafady, Ayman; King Saud University, Chemistry Department; College of Science, King Saud University, Chemistry Ma, Shengqian; University of South Florida, Department of Chemistry

# Recent advances in MOF-based photocatalysis: environmental remediation under visible light

Qi Wang<sup>a,b\*</sup>, Qiaoyuan Gao<sup>a</sup>, Abdullah M Al-Enizi<sup>c</sup>, Ayman Nafady<sup>c</sup>, Shengqian Ma<sup>b,\*</sup>

<sup>a</sup>*School of Environmental Science and Engineering, Zhejiang Gongshang University, Hangzhou 310018, China*

<sup>b</sup>*Department of Chemistry, University of South Florida, Tampa, FL 33620, USA*

<sup>c</sup>*Chemistry Department, College of Science, King saud University, Riyadh, 11451, Saudi Arabia*

**Abstract:** Visible light-induced photocatalysis is a promising way for environmental remediation due to efficient utilization of solar energy. Recently, metal–organic frameworks (MOFs) have attracted increasing attention in the field of photocatalysis. In comparison with traditional metal oxide semiconductors, MOFs have many advantages, such as high specific surface area, rich topology and easily tunable porous structure. In this review, we aim to summarize and illustrate recent advances in MOF-based photocatalysis for environmental remediation under visible light, including wastewater treatment, air purification and disinfection. A series of strategies have been designed to modify and regulate pristine MOFs for enhanced photocatalytic performance, such as ligand functionalization, mixed-metal/linker strategy, metal ions/ligands immobilization, dye sensitization, metal nanoparticles loading, carbon materials decoration, semiconductor coupling, MOF/COF coupling, carrier loading and magnetic recycling. The above modifications may result in extended visible light absorption, efficient generation, separation and transfer of photogenerated charges, as well as good recyclability. However, there are still many challenges and obstacles. In order to meet the requirements of using MOF photocatalysis as a friendly and stable technology for low-cost practical applications, its future development prospects are also discussed.

---

\* To whom correspondence should be addressed: wangqi8327@zjgsu.edu.cn (QW); sqma@usf.edu (SM)

## 1. Introduction

In the 21st century, environmental pollution and fossil energy crisis have become two major problems that plague human survival and development. Among various renewable energy sources, solar energy is a kind of abundant and clean choice. Thus, solar light-driven technologies for environmental remediation have attracted great attention. Herein, heterogeneous photocatalysis, as represented by  $\text{TiO}_2$ , was proved to be a feasible way. Upon UV light irradiation, electron-hole ( $e^-h^+$ ) pairs can be generated in  $\text{TiO}_2$ , leading to reductive and oxidative reactions.<sup>1</sup> In this way, various kinds of refractory organic pollutants can be degraded and heavy metal ions can be reduced by  $\text{TiO}_2$  photocatalysis.<sup>2</sup> However, UV light accounts less than 5% of incident solar light, the utilization of visible light (nearly 45%) is more promising for better utilization of solar energy and future large-scale practical applications. Consequently, there is an urgent need to develop more visible light-responsive photocatalysts with high activity and stability.

Metal-organic frameworks (MOFs) are a class of porous crystalline materials consisting of metallic nodes (metal ions or clusters) and organic linkers.<sup>3</sup> Due to ultra-high specific surface area (over 6000  $\text{m}^2/\text{g}$ ),<sup>4</sup> rich topology and easily tunable porous structure,<sup>5</sup> MOFs have recently attracted increasing attention in the field of photocatalysis.<sup>6-10</sup> Distinct from classical inorganic semiconductors with delocalized conduction band (CB) and valence band (VB), MOFs can be identified as molecules arranged in a crystalline lattice. In addition, some MOFs displayed semiconductor-like behavior, such as MOF-5 ( $\text{Zn}_4\text{O}(\text{BDC})_3$ , BDC: 1,4-benzenedicarboxylate), UiO-66 ( $\text{Zr}_6\text{O}_4(\text{OH})_4(\text{BDC})_6$ , UiO: University of Oslo) and MIL-125 ( $\text{Ti}_8\text{O}_8(\text{OH})_4(\text{BDC})_6$ , MIL: Materials Institute Lavoisier). Herein, the metal-oxo clusters and organic linkers can be regarded as isolated semiconductor quantum dots and light-absorbing antenna, respectively.<sup>11-13</sup> In the past decades, with the development of water/acid-resistant MOF materials,<sup>14</sup> more and more light-responsive MOFs have been reported for photocatalytic removal of pollutants,<sup>2,8</sup> disinfection of bacteria,<sup>15</sup> production of  $\text{H}_2$ ,<sup>16,17</sup> fixation of  $\text{CO}_2$ ,<sup>18</sup> selective transformation of organics<sup>19</sup> and etc.<sup>20,21</sup>

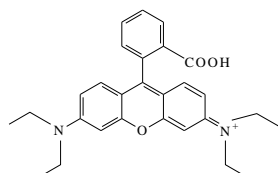
Since there are a large number of selections between metal ions/clusters and organic linkers, MOFs are endowed as extremely tunable photocatalysts for efficient utilization of solar light. In the past five years, there are many reviews discussing various aspects of MOFs,<sup>6-9, 16, 22-26</sup> including environmental applications. For example, Wang et al. summarized the photocatalytic degradation of

organic pollutants from wastewater in 2014.<sup>27</sup> At that moment, most photoactive MOFs were applied for the degradation of dyes under UV or UV-Vis light irradiation. Very small numbers of MOFs utilizing visible light were listed and usually need the assistance of H<sub>2</sub>O<sub>2</sub> as oxidant. Later in 2016, Wang et al. further conducted a mini-review on photocatalytic reduction of Cr(VI) by MOFs.<sup>8</sup> In the same year, Ye's group also summarized the progress in MOF photocatalysis. They mainly focused on several representative MOFs, including MOF-5, UiO-66(Zr), MIL-125(Ti) and MIL-101(Fe). In comparison with traditional semiconductors, the reported MOFs or MOF-based composites displayed promising photocatalytic performance, especially in CO<sub>2</sub> reduction.<sup>28</sup> The modified MOFs as photocatalysts were also reviewed by Qiu et al.<sup>29</sup> They focused on the progress of various modification strategies to typical light-responsive MOFs. Enhanced photocatalytic performance (pollutants removal, CO<sub>2</sub> reduction, H<sub>2</sub> production or organic transformation) were reported utilizing UV, UV-Vis or visible light. Meanwhile, Bedia et al. conducted a review on the synthesis and characterization of MOFs for photocatalytic water purification.<sup>30</sup> Besides, a short review concerning iron-based MOFs for visible light-induced photocatalysis were also reported.<sup>31</sup> In this year, Jiang's group summarized their recent contributions toward MOF-based photocatalysis and photothermal catalysis, mainly focusing on H<sub>2</sub> production and selective organic transformations.<sup>24</sup> However, there were limited reviews focusing on visible light-responsive MOFs, especially for environmental remediation. With the increasing variety of MOFs and MOF-based composites, invaluable application prospects will be expected.

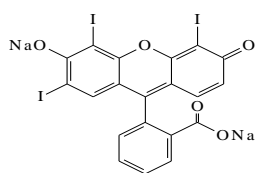
Thus, based on the above analysis, this review aims at recent advances in MOF-based photocatalysis for environmental remediation under visible light, including wastewater treatment, air purification and disinfection. For example, various kinds of organic dyes, phenolic compounds, insecticides, pharmaceuticals and personal care products (PPCPs) in aqueous media can be photodegraded. The structures of typical organic pollutants photodegraded by MOFs were presented in Fig. 1. Besides, the highly migratable Cr(VI) and radiative U(VI) can be photoreduced to corresponding trivalent states,<sup>8, 32</sup> which can be easily precipitated and separated from aqueous solution. Gaseous pollutants such as NO and toluene can be photo-oxidized into harmless products.<sup>33</sup> Inactivation of bacterial was also reported.<sup>34</sup> Thus, for better understanding and easy reading, this review begins with pristine MOFs that can work under visible light. Strategies for engineering MOFs for enhanced performance are further presented, including ligand functionalization,

mixed-metal/linker strategy, metal ions/ligands immobilization, dye sensitization, metal nanoparticles loading, carbon materials decoration, semiconductor coupling, MOF/COF coupling, carrier loading and magnetic recycling.

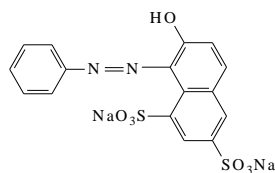
### Chemical structures of typical dye pollutants



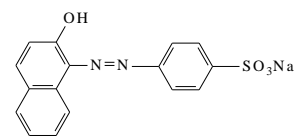
Rhodamine B (RhB)



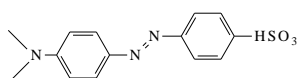
Erythrosine (ER)



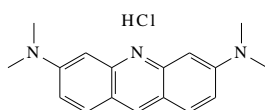
Orange G (OG)



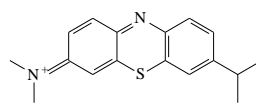
Acid Orange 7 (AO7)



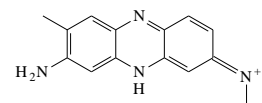
Methyl Orange (MO)



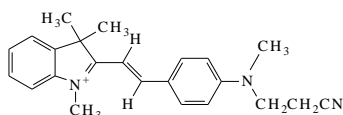
Acridine Orange (AO)



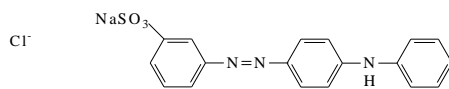
Methylene Blue (MB)



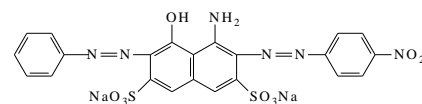
Neutral red (NR)



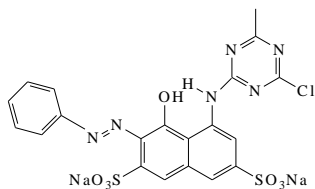
Basic red 14 (BR14)



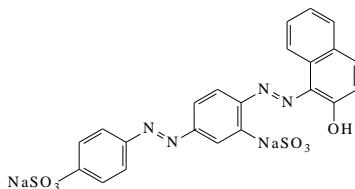
Metanil yellow (MY)



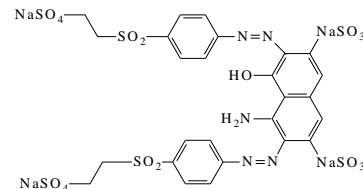
Amido-Black (AB)



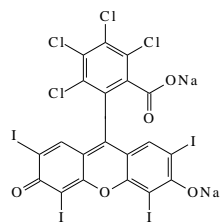
Reactive Brilliant Red X-3b (X-3B)



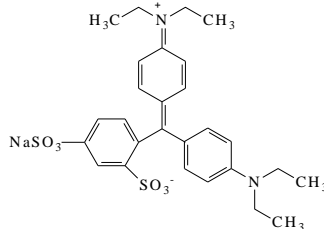
Ponceau BS (PBS)



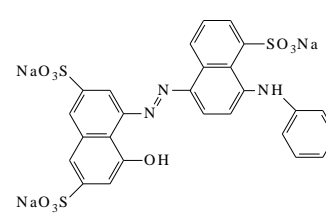
Remazol black B (RBB)



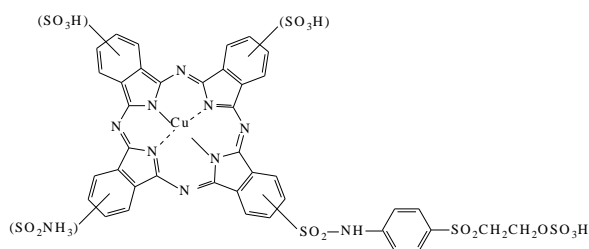
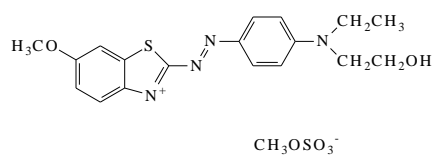
Rose Bengal (RB)



Disulfine blue 17 (DB17)

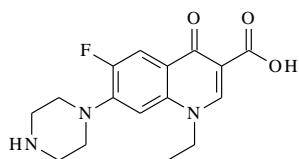


Acid blue 92 (AB92)

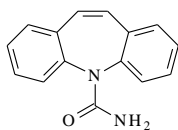


Basic Blue 41 (BB41)

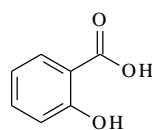
Reactive blue 21 (RB21)

**Chemical structures of typical PPCPs and insecticides**

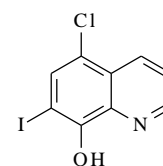
Norfloxacin (Noroxin)



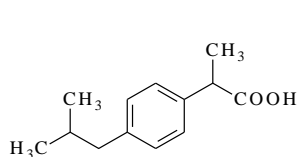
Carbamazepine (CBZ)



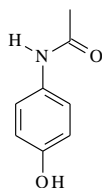
Salicylic acid (SA)



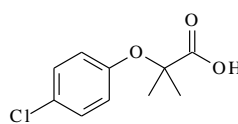
Acetaminophen (ACE)



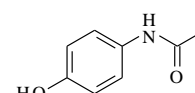
Ibuprofen (IBP)



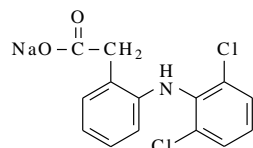
Cloquinol (CLQ)



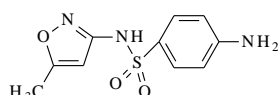
Clofibric acid (CA)



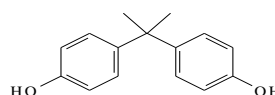
Acetaminophen (ACT)



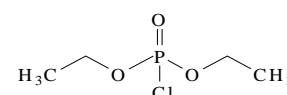
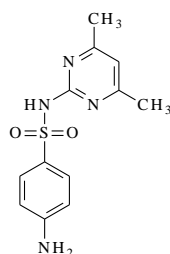
Diclofenac sodium (DS)



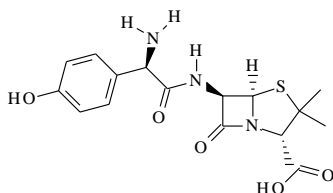
Sulfamethoxazole (SMZ)



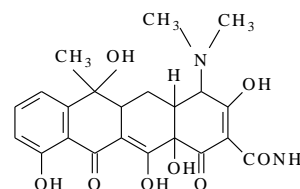
Bisphenol A (BPA)

Dimethyl chlorophosphate  
(DMCP)

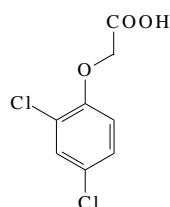
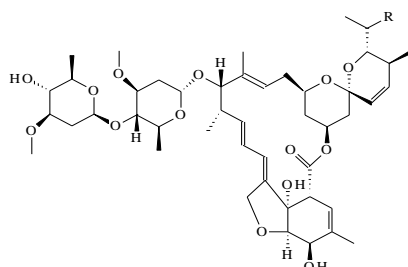
Sulfamethazine (SMT)



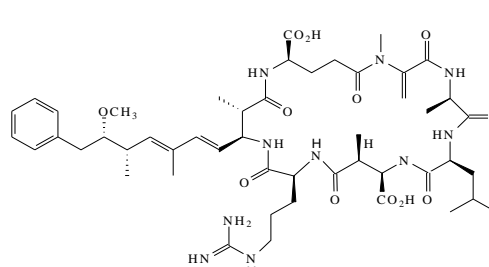
Amoxicillin (AMX)



Tetracycline (TC)

2,4-dichlorophenoxyacetic acid  
(2,4-D)

Abamectin



Microcystin-LR (MC-LR)

**Fig. 1.** Chemical structures of typical dyes, PPCPs and insecticides reported in literatures.

## 2. The development of photoactive MOFs from UV to visible light

Early in 1999, MOF-5 was synthesized by Yaghi's group.<sup>35</sup> In 2004, optical and vibrational properties of MOF-5 was investigated by Zecchina's group using UV-Vis Diffuse Reflectance Spectroscopy (UV-Vis DRS), Photoluminescence (PL) spectroscopy and Raman spectroscopy. It was proposed that  $Zn_4O_{13}$  clusters and organic ligands in MOF-5 can behave as ZnO quantum dots (QDs) and light-absorbing antenna, respectively.<sup>36</sup> Until 2007, the semiconductor behavior of MOF-5 was demonstrated by Garcia's group *via* later laser flash photolysis, and the application of MOF-5 as a photocatalyst for phenol degradation was first tested.<sup>37</sup> The charge-transfer processes on MOF-5 were further studied *via* photoluminescence.<sup>38</sup> Despite of these, MOF-5 decomposed gradually upon exposure to moisture in air or in water.<sup>35</sup> The instability of MOF-5 motivated researchers to find or synthesize more stable photocatalytic MOFs.

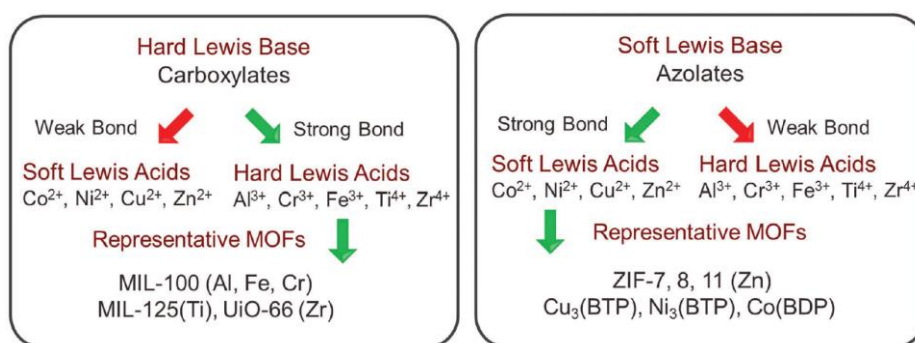


**Fig. 2.** Strategies to construct stable MOFs guided by HSAB theory. Adapted with permission from ref.<sup>39</sup>, © 2018 WILEY-VCH.

According to metal–ligand bond strengths and the HSAB (hard/soft acid/base) principle,<sup>5</sup> stable MOFs can be synthesized *via* either hard or soft Lewis base. As show in Fig. 2, high-valent metal ions (such as Ti<sup>4+</sup>, Zr<sup>4+</sup>, Al<sup>3+</sup>, Fe<sup>3+</sup> and Cr<sup>3+</sup>) with hard Lewis base (carboxylates) can lead to the formation of stable MOFs. The MIL series (MIL: Material Institute Lavoisier) and UiO-66(Zr) (UiO: University of Oslo) are representative MOFs with good stability. Besides, divalent metal ions (such as Zn<sup>2+</sup>, Co<sup>2+</sup>, Cu<sup>2+</sup> and Ni<sup>2+</sup>) with soft Lewis base (azolates) resulted in several stable MOFs. Among which, the zeolitic imidazolate frameworks (ZIFs) constructed by Zn<sup>2+</sup> and imidazolate linkers were the most representative examples. Consistent with the above classifications, water-stable UiO-66(Zr) was fabricated and displayed photocatalytic activity for H<sub>2</sub> evolution.<sup>40, 41</sup> Besides, MIL-125(Ti) was highly photosensitive and water-stable, which can be photoexcited by UV light

leading to reduction of Ti(VI) center and oxidation of adsorbed alcohol molecules.<sup>42</sup>

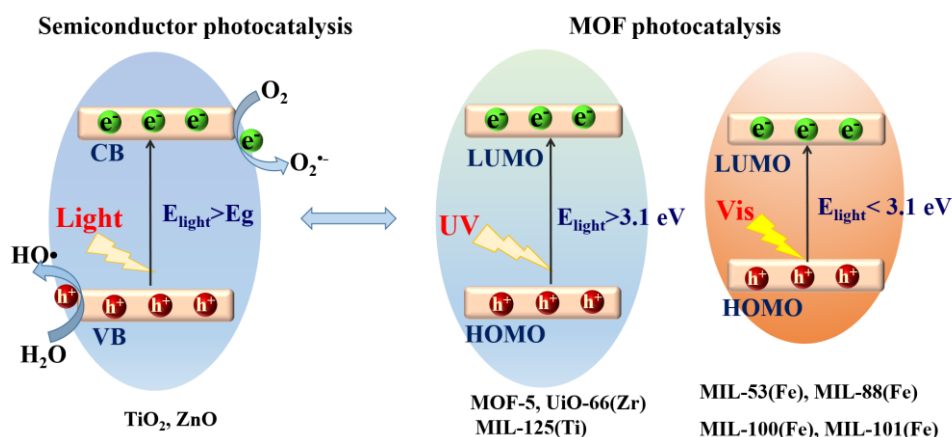


**Fig. 3.** Mechanism for semiconductor photocatalysis (left); Comparison of band gaps and light source (UV or visible light) between representative MOFs (right).

Based on the principle of traditional semiconductor photocatalysis, the photocatalyst can be directly excited by incident light with energy ( $E_{\text{light}}$ ) larger than the band gap ( $E_g$ ). In this way, electron–hole ( $e^-h^+$ ) pairs can be generated (Fig. 3). Similarly, electron transitions can also occur from the highest occupied molecular orbital (HOMO) to lowest unoccupied molecular orbital (LUMO) in MOFs, leaving holes ( $h^+$ ) in HOMO. Herein, the HOMO/LUMO play similar roles as CB/VB in semiconductors. Namely, the photogenerated electrons in LUMO can be transferred to O<sub>2</sub>, leading to the formation of superoxide radicals (O<sub>2</sub><sup>•-</sup>). Meanwhile, holes in HOMO can oxidize surface hydroxyl group/water, generating hydroxyl radicals (HO•). Due to the presence of reactive species (O<sub>2</sub><sup>•-</sup>, HO• and h<sup>+</sup>), organic pollutants can be degraded. However, the band gaps ( $E_{\text{HOMO-LUMO}}$ ) were reported to be ca. 3.4 eV, 3.9 eV and 3.6 eV for MOF-5, UiO-66(Zr) and MIL-125(Ti), respectively.<sup>37, 43-45</sup> For effective excitation of such MOFs, the incident light ( $E_{\text{light}} = 1240/\lambda > E_{\text{HOMO-LUMO}}$ ) was restricted to UV light with short wavelength ( $\lambda < 365 \text{ nm}$ ). Thus, for efficient utilization of solar energy, MOFs responsive to visible light ( $\lambda > 400 \text{ nm}$ , or  $E_{\text{light}} < 3.1 \text{ eV}$ ) are more desirable.

In contrast to MOFs with wide bandgap, Fe-MOFs are extremely appealing. The extensive Fe–O clusters can be directly excited by visible light, leading to more efficient utilization of solar energy. Besides, the application cost of Fe-MOFs will be much cheaper due to the earth-abundant nature of Fe element. As shown in Fig. 4A, using Fe(NO<sub>3</sub>)<sub>3</sub> or FeCl<sub>3</sub> as Fe<sup>3+</sup> precursor, terephthalic acid



(H<sub>2</sub>BDC), fumaric acid (H<sub>2</sub>FUM) or benzene-1,3,5-tricarboxylic acid (H<sub>3</sub>BTC) as ligand precursor, various kinds of Fe-MOFs (MIL-53, MIL-68, MIL-88A, MIL-88B, MIL-100 and MIL-101) can be obtained. As summarized in Table 1,<sup>39, 46</sup> the corresponding  $E_{\text{HOMO-LUMO}}$  values ranged from 1.88 eV to 2.88 eV, which can be directly excited by visible light. Various kinds of organic pollutants (RhB, MB, AO7, CA, CBZ and etc.) were reported to be degraded by Fe-MOFs under visible light. However, under most circumstances, H<sub>2</sub>O<sub>2</sub> was added as electron acceptor to accelerate the degradation process. Besides, photocatalytic reduction of Cr(VI) or U(VI) can also be achieved on MIL-53(Fe) using (NH<sub>4</sub>)<sub>2</sub>C<sub>2</sub>O<sub>4</sub> or HCOOH as h<sup>+</sup> scavenger.<sup>32, 47</sup>

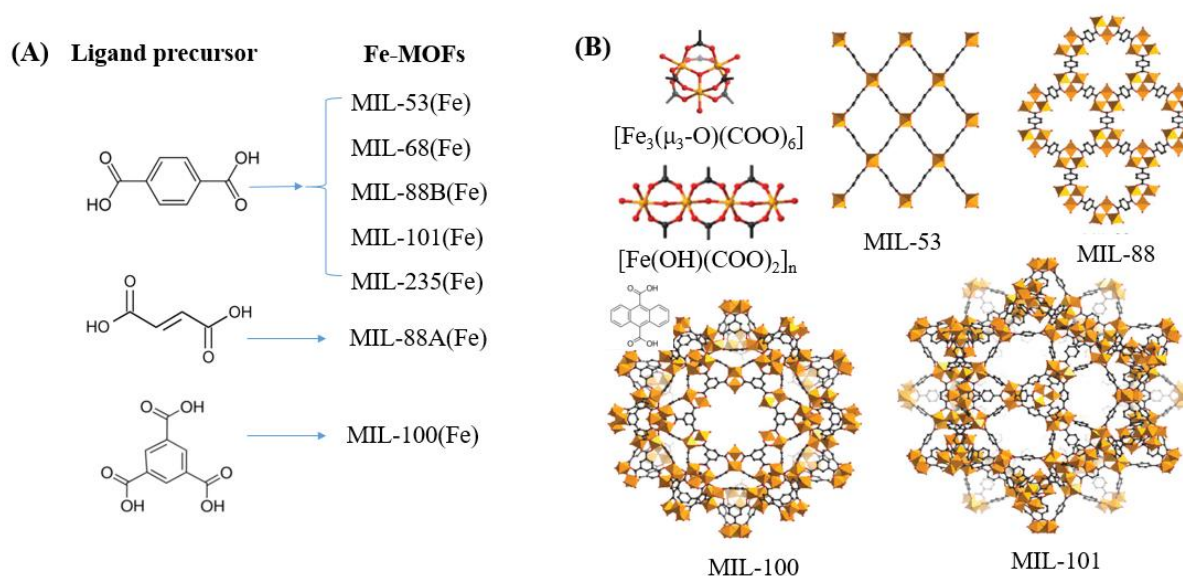


**Fig. 4.** (A) Fe-MOFs prepared with different ligand precursors; (B) Structures of metal clusters and representative MIL series of Fe-MOFs. Adapted with permission from ref. <sup>39</sup>, © 2018 WILEY-VCH.

Among the above various visible light-responsive Fe-MOFs, MIL-100(Fe) with tricarboxylate linker was theoretically more stable than Fe-MOFs (MIL-53, MIL-88 and MIL-101) with dicarboxylate linker.<sup>5</sup> As illustrated in Fig. 4B, both MIL-100(Fe) and MIL-101(Fe) display 3D structures. Among which, MIL-100(Fe) possess thermal and water stability.<sup>48</sup> Whereas, MIL-101(Fe) may be transformed into MIL-53 or MIL-88 in strong polar solvents.<sup>49, 50</sup> Furthermore, MIL-100 was reported to have higher water stability than UiO and ZIF.<sup>51-53</sup> The non-toxicity of MIL-100 was also verified by in-vivo toxicity assays. Thus, MIL-100(Fe) is expected to be a promising visible light-responsive photocatalyst for environmental remediation. Using antibiotic tetracycline (TC) as

target pollutant, the performance of MIL-53(Fe), MIL-100(Fe) and MIL-101(Fe) were compared by Wang et al.<sup>54</sup> However, it is MIL-101(Fe) rather than MIL-100(Fe) exhibited highest performance (Fig. 5A). TC can be removed *via* both adsorption and photocatalysis with a value of ca. 97% by MIL-101(Fe) after 180 min visible light irradiation. The rate constant ( $k$ ) was calculated to be  $1.6 \times 10^{-2} \text{ min}^{-1}$  (Fig. 5B), which was 7.1 and 1.8 times that on MIL-53(Fe) and MIL-100(Fe), respectively. However, the highest specific surface area ( $S_{\text{BET}}$ ) was observed on MIL-100(Fe) (1203  $\text{m}^2/\text{g}$ ), which was much larger than that of MIL-101(Fe) (253  $\text{m}^2/\text{g}$ ) and MIL-53(Fe) (21  $\text{m}^2/\text{g}$ ). Generally, the catalyst surface played important role in heterogeneous photocatalysis, and larger  $S_{\text{BET}}$  was usually beneficial for photocatalysis under other identical conditions. As for MIL-101(Fe), in addition to highest adsorption of TC, lowest band gap (1.88 eV) may also be beneficial for the greatest TC removal performance. Thus, the difference in photocatalytic performance of the tested Fe-MOFs may be influenced by both band gap and adsorption properties. At different conditions (temperature, solvent, and etc.), the different types of Fe-MOFs may have their own advantages and application fields. Further research work should be undertaken to enhance the photocatalytic performance as well as water/thermos-stability under harsh conditions.

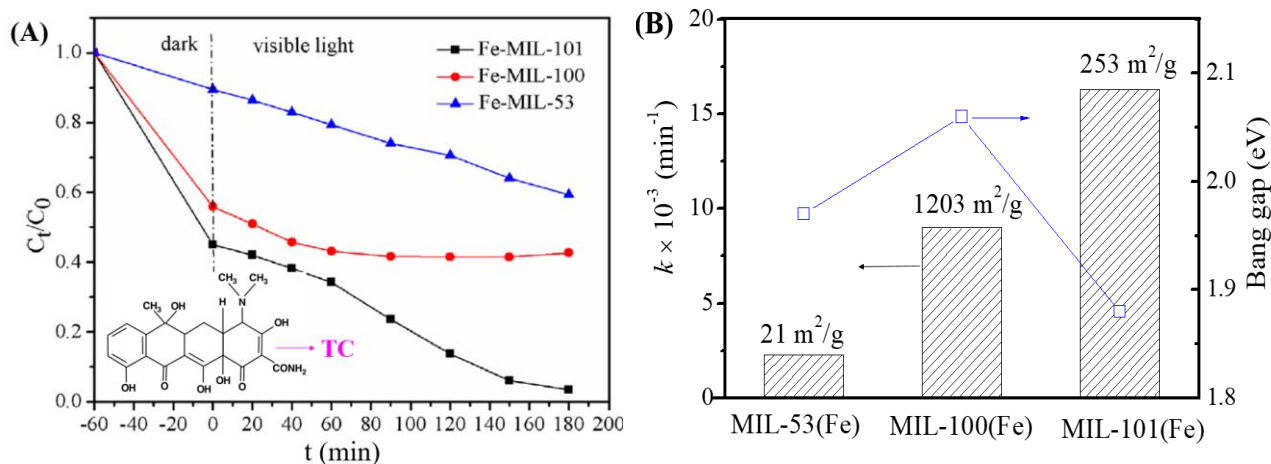


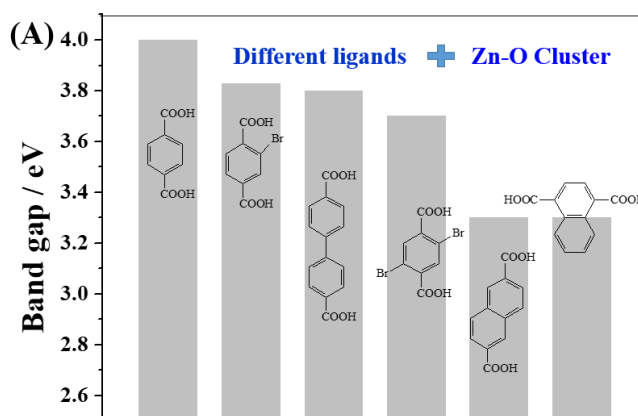
**Fig. 5.** (A) Photocatalytic degradation of TC by different type of Fe-MILs; (B) Rate constant for TC removal on different Fe-MILs in comparison with band gaps and specific surface areas. Adapted with permission from ref. <sup>54</sup>.

© 2018 Elsevier.

In addition to Fe-MOFs, the dicarboxylate and tricarboxylate linkers can interact with other metal ions (such as  $\text{Cu}^{2+}$ ,  $\text{Al}^{3+}$  or  $\text{Cr}^{3+}$ ), leading to the formation of visible light-active HKUST-1 (HKUST: Hong Kong University of Science and Technology), MIL-53(Al) or MIL-53(Cr), respectively. With

the development of MOF materials, the selection of ligands was extended from the original H<sub>2</sub>BDC/H<sub>3</sub>BTC to structures with higher  $\pi$ -conjugation. A large number of visible light-responsive MOFs were synthesized and applied for environmental remediation. For example, the band gap of MOF-5 (4.0 eV) can be reduced to 3.3 eV when using biphenyl or naphthalenedicarboxylic acids as ligand precursor (Fig. 6A). A novel Zn<sup>2+</sup>-centered MOF (UTSA-38) with narrow band gap (2.85 eV) was fabricated using 2,6-naphthalenedicarboxylic acid (H<sub>2</sub>NDC) as ligand precursor (Fig. 6B).<sup>55</sup> Photocatalytic degradation of methyl orange (MO, 20 mg/L) was achieved by UTSA-38, despite of low efficiency (< 30%) under visible light irradiation for 120 min.

Moreover, strategies were also developed to utilize the water-stable Ti- and Zr-centered MOFs. Motivated by the findings of MOF-5, the band gaps along with photocatalytic performance may be tuned by changing the organic linker.<sup>44</sup> As for Zr-MOFs, once the H<sub>2</sub>BDC was replaced by anthracene-9,10-dicarboxylic acid (H<sub>2</sub>ANDC) or 1,4-bis(2-[4-carboxyphenyl]ethynyl) benzene (H<sub>2</sub>CPEB), UiO-66(AN) or VUN-1 (VNU: Vietnam National University) with band gap of 2.47 eV and 2.88 eV were obtained (Fig. 6B), respectively.<sup>56, 57</sup> For the degradation of MO (20 mg/L), shorter time (90 min) and smaller catalyst dosage (0.1 g/L) led to 65% removal efficiency under visible light.<sup>56</sup> Methylene blue (MB) can be 100% removed by VUN-1 after 180 min UV-Vis irradiation.<sup>40</sup> As for Ti-MOFs, the same strategy still works well. The band gap can be engineered when Ti–O clusters was connected with different organic ligands (Fig. 6C).<sup>45</sup> The performance of different Ti-MOFs were investigated and compared via photocatalytic water splitting under UV-Vis light.



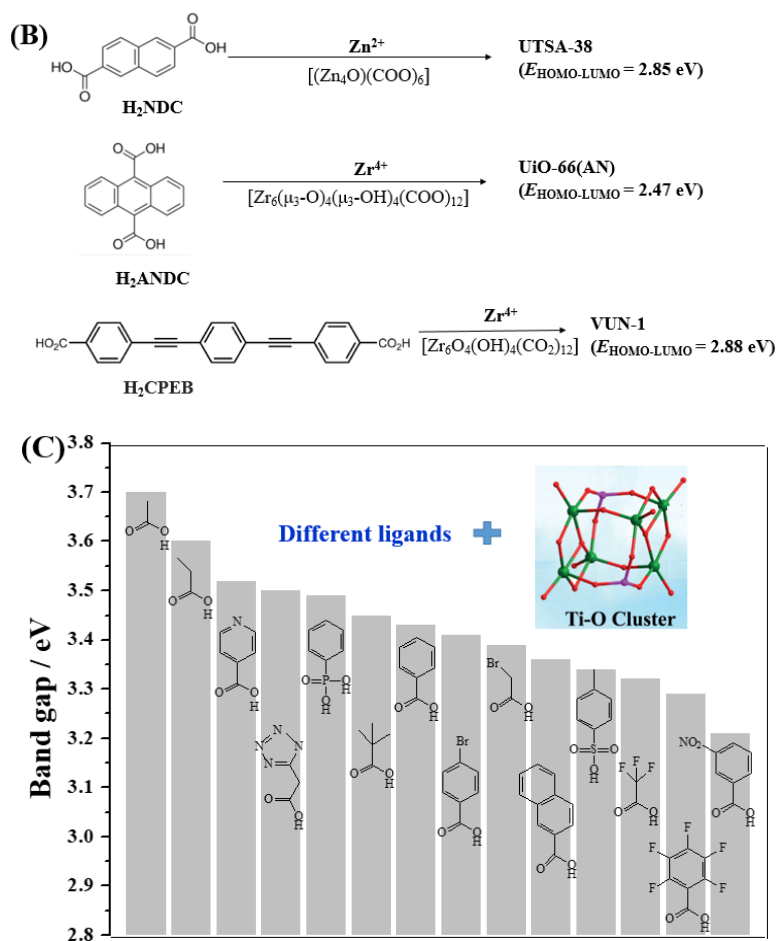


**Fig. 6.** (A) Bandgap engineering of Zn–O clusters with different organic ligands;<sup>44</sup> (B) Visible light-responsive Zn-MOFs and Zr-MOFs prepared with different ligand precursors; (C) Bandgap engineering of Ti–O clusters with different organic ligands.<sup>45</sup> Adapted with permission from ref.<sup>44, 45</sup>, © 2008 Wiley-VCH, © 2016 Wiley-VCH.

**Table 1.** Photocatalytic removal of pollutants by typical pristine MOFs under visible light.

MOF	Clusters	Ligands	$E_{\text{HOMO-LUMO}}$ (eV)	$^a S_{\text{BET}}$ ( $\text{m}^2/\text{g}$ )	Pollutant	$C_{\text{pollutant}}$ (mg/L)	$C_{\text{catalyst}}$ (g/L)	Time (min)	$^c \eta$ (%)	Ref.
MIL-53(Fe)	$[\text{Fe}(\text{OH})(\text{COO})_2]_n$	$\text{H}_2\text{BDC}$	2.62	NA	AO7 (with PS)	17.5	0.6	90	100	58
			2.88	19	RhB (with $\text{H}_2\text{O}_2$ )	10	0.4	50	98	59
			2.69	38	RhB (with $\text{H}_2\text{O}_2$ )	10	0.4	180	90	60
			2.55	16	RhB (with PMS)	40	1.0	20	95	61
			2.72	NA	MB	128	0.01	60	20 <sup>b</sup>	62
			NA	184	CA (with $\text{H}_2\text{O}_2$ )	40	0.1	280	98	63
					CBZ (with $\text{H}_2\text{O}_2$ )	40	0.1	280	90	
			2.72	NA	Cr(VI) (with $(\text{NH}_4)_2\text{C}_2\text{O}_4$ )	20	1.0	40	100	47
			2.72	NA	U(VI) (with HCOOH, $\text{N}_2$ )	50	0.4	120	80	32
			2.91	NA	SMT (with Fe(III), SPC)	5.6	0.2	60	91	64
MIL-68(Fe)	$[\text{Fe}(\text{OH})(\text{COO})_2]_n$	$\text{H}_2\text{BDC}$	2.80	NA	Cr(VI) (with $(\text{NH}_4)_2\text{C}_2\text{O}_4$ )	20	0.25	5	100	65
					Cr(VI) (with MG)	10	0.25	240	95	
					MG (with Cr(VI))	30	0.25	240	80	
MIL-88B(Fe)	$[\text{Fe}_3(\mu_3\text{-O})(\text{COO})_6]$	$\text{H}_2\text{BDC}$	NA	NA	MB	10	0.25	50	100	66
					RhB	10	0.25	60	94	
MIL-101(Fe)	$[\text{Fe}_3(\mu_3\text{-O})(\text{COO})_6]$	$\text{H}_2\text{BDC}$	1.88	252	TC	50	0.5	180	97	54
MOF-235(Fe)	$[\text{Fe}_3(\mu_3\text{-O})(\text{COO})_6]$	$\text{H}_2\text{BDC}$	1.94	148	RhB (with $\text{H}_2\text{O}_2$ )	19.2	0.2	20	100	67
MIL-88A(Fe)	$[\text{Fe}_3(\mu_3\text{-O})(\text{COO})_6]$	$\text{H}_2\text{FUM}$	2.05	NA	MB (with $\text{H}_2\text{O}_2$ )	32	0.4	20	100	68
MIL-100(Fe)	$[\text{Fe}_3(\mu_3\text{-O})(\text{COO})_6]$	$\text{H}_3\text{BTC}$	NA	1974	MO	5	0.33	420	40 <sup>b</sup>	69
HKUST-1	$[\text{Cu}_2(\text{CO}_2)_4]$	$\text{H}_3\text{BTC}$	2.63	197	MG	10	0.25	85	98	70
					SO	15	0.25	85	89	
MIL-53(Al)	$[\text{Al}(\text{OH})(\text{COO})_2]_n$	$\text{H}_2\text{BDC}$	3.87	NA	MB	128	0.1	60	30 <sup>b</sup>	62
MIL-53(Cr)	$[\text{Cr}(\text{OH})(\text{COO})_2]_n$	$\text{H}_2\text{BDC}$	3.20	NA	MB	128	0.01	60	32 <sup>b</sup>	62
UiO-66(AN)	$[\text{Zr}_6(\mu_3\text{-O})_4(\mu_3\text{-OH})_4(\text{COO})_{12}]$	$\text{H}_2\text{ANDC}$	2.47	627	MO	20	0.1	90	65	56
UTSA-38	$[(\text{Zn}_4\text{O})(\text{COO})_6]$	$\text{H}_2\text{NDC}$	2.85	1690	MO	20	0.4	120	64 <sup>b</sup>	71

VNU-1	$[\text{Zr}_6\text{O}_4(\text{OH})_4(\text{CO}_2)_{12}]$	$\text{H}_2\text{CPEB}$	2.88	2100	MB	100	0.67	180	$100^b$	<sup>57</sup>
					MO	100	0.67	180	$83^b$	
Bi-mna	NA	$\text{H}_2\text{mna}$	NA	35	RhB	20	1.0	120	96	<sup>72</sup>
					MB	20	1.0	120	95	
PCN-222	$[\text{Zr}_6(\mu_3\text{-O})_4(\mu_3\text{-OH})_4(\text{OH})_4(\text{H}_2\text{O})_4(\text{COO})_8]$	$\text{H}_2\text{TCPP}$	NA	1914	BPA	100	1.0	120	90	<sup>73</sup>

<sup>a</sup>  $S_{\text{BET}}$  surface area were presented in integer numbers; <sup>b</sup> UV-Vis light or sunlight; <sup>c</sup> Removal efficiencies ( $\eta$ ) for pollutants were received or estimated from the figures in reference and presented in integer numbers; <sup>d</sup> mM; NA: no experimental data available; PS: persulfate; PMS: peroxymonosulfate; SPC: percarbonate; SMT: Sulfamethazine;  $\text{H}_2\text{BDC}$ : terephthalic acid;  $\text{H}_2\text{FUM}$ : fumaric acid;  $\text{H}_3\text{BTC}$ : benzene-1,3,5-tricarboxylic acid;  $\text{H}_2\text{ANDC}$ : anthracene-9,10-dicarboxylic acid;  $\text{H}_2\text{NDC}$ : 2,6-naphthalenedicarboxylic acid;  $\text{H}_2\text{CPEB}$ : 1,4-bis(2-[4-carboxyphenyl]ethynyl) benzene;  $\text{H}_2\text{mna}$ : 2-mercaptonicotinic acid;  $\text{H}_2\text{TCPP}$ : Tetrakis (4-carboxyphenyl) porphyrin.

### 3. Strategies for engineering visible light-active MOFs

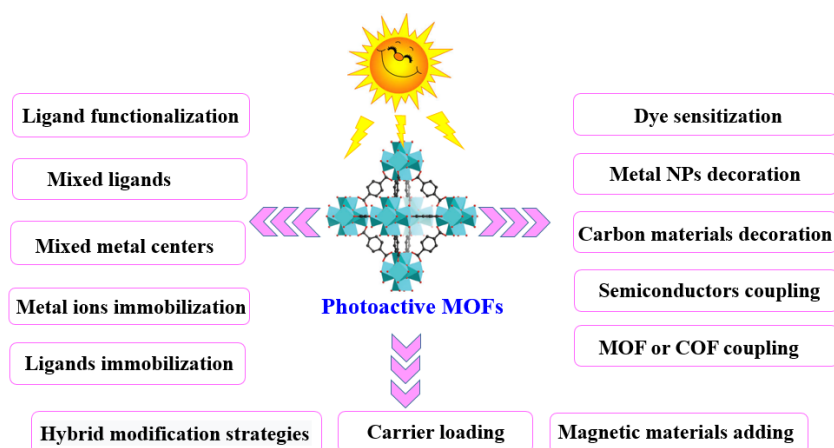


**Fig. 7.** Strategies to engineer MOFs as efficient photocatalysts for environmental applications.

In comparison with traditional metal oxide semiconductors, MOFs have many advantages in photocatalysis because of their inherent structural features (such as large surface area and porous structure) and tunable combination between metallic nodes and organic linkers. However, the photocatalytic efficiency still cannot meet the actual needs. Many attempts have been made to enhance the photocatalytic performance. As shown in Fig. 7, a series of strategies have been developed for extended visible light absorption, more efficient generation, separation and transfer of charge carriers, as well as good recyclability.

#### 3.1 Ligand functionalization

Considering the huge difference in available quantities of metal ions and organic linkers, modification of organic linkers rather than metallic nodes will be a powerful strategy to tune the optical properties of MOFs. Take the most frequently studied  $H_2BDC$  precursor as an example, MIL-125(Ti) synthesized with unmodified  $H_2BDC$  can only respond to UV light.<sup>42</sup> As shown in Fig. 8, after introducing  $-NH_2$  group into  $H_2BDC$ , isostructural  $NH_2$ -MIL-125(Ti) was synthesized in the same way, which displayed yellow color and extended visible light absorption.<sup>74</sup> The band gap dramatically decreased from 3.60 eV to 2.46 eV. Besides, due to enhanced  $CO_2$  adsorption by  $-NH_2$  group,  $NH_2$ -MIL-125(Ti) was reported for the first time as a targeted photocatalyst toward  $CO_2$  reduction under visible light. Furthermore, dye-like moieties with higher  $\pi$ -conjugated group was used as substituent to  $H_2BDC$ .<sup>75</sup> The resulting MR-MIL-125(Ti) displayed a clear red shift of optical absorption. The absorption edge reached almost 700 nm, indicating the band gap was ca. 1.93 eV.

Subsequently, a p-type Ti-containing MOF (NTU-9) was also developed, using two  $-OH$  groups substituted H<sub>2</sub>BDC (2,5-dihydroxyterephthalic acid) as organic linker.<sup>76</sup> The light absorption region can be extended up to 750 nm. The red NTU-9 sample can act as visible light-responsive photocatalyst for dye degradation with the assistance of H<sub>2</sub>O<sub>2</sub>. RhB (48 mg/L) and MB (32 mg/L) dyes can be completely degraded after 80 min and 20 min visible light irradiation, respectively. Moreover, high stability can also be observed after three cyclic runs.

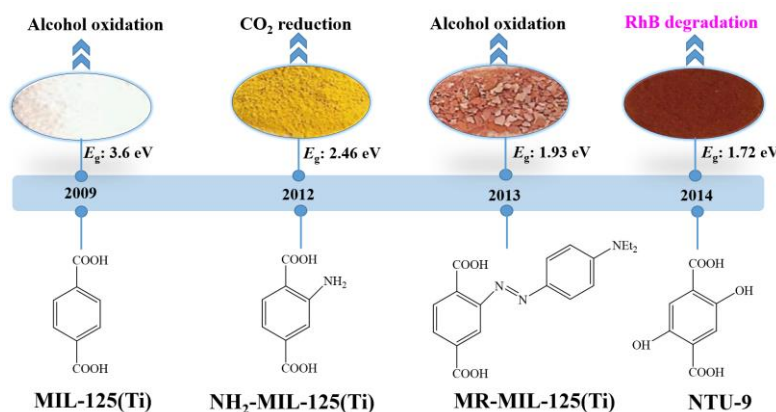


**Fig. 8.** The development history of Ti-MOFs via ligand functionalization and their first application in photocatalysis.

To elucidate the specific role of  $-NH_2$  substitution in engineering the optical response of MIL-125(Ti), Hendon et al. carried detailed research *via* both experimental and theoretical ways.<sup>77</sup> Results indicated that the enhanced optical properties were ascribed to regulation of HOMO. The introducing of single  $-NH_2$  group leads to 1.2 eV elevation of HOMO with no influence on LUMO. The effect of other functional groups ( $-OH$ ,  $-CH_3$ ,  $-Cl$ ) as well as diaminated linker BDC-(NH<sub>2</sub>)<sub>2</sub> were also studied. The band gaps decreased in the order of  $-CH_3/-Cl < -OH < -(NH_2)_2$  substitution. Herein,  $-(NH_2)_2$  substitution was considered as the most powerful way. Besides, the band gap of MIL-125(Ti) can be rational regulated by changing the ratio between  $-NH_2$  and  $-(NH_2)_2$ .<sup>77</sup> This strategy can be further extended to other aromatic linkers.



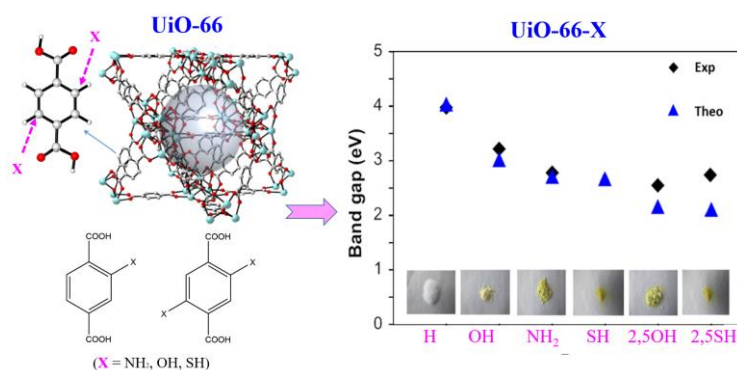


**Fig. 9.** The effect of functionalized BDC linkers on regulating the band gaps of UiO-66(Zr). Adapted with permission from ref. <sup>78</sup>, © 2015 American Chemical Society.

A similar band gap engineering by ligand functionalization was also reported for UiO-66(Zr) and UiO-66(Ce).<sup>78, 79</sup> For example, Hendrickx et al. conducted a combined theoretical and experimental study on the intrinsic optical properties of UiO-66(Zr).<sup>78</sup> As shown in Fig. 9, using mono or bifunctionalized BDC linkers, the band gap of UiO-66(Zr) can be engineered from 4.0 eV to 2.2 eV. The values obtained via HSE06 calculations agreed well with experimental results. As for the mechanism of band gap engineering, similar to NH<sub>2</sub>-MIL-125(Ti),<sup>77</sup> the decreased band gap was ascribed to elevation of HOMO after ligand functionalization.<sup>80</sup> Typically, according to the theory of conventional semiconductor photocatalysis, narrower band gap means more efficient response to visible light, which may have a positive effect on photocatalytic performance under visible light. Unexpectedly, some difference was reported for MOFs photocatalysis. For example, UiO-66-X (X = H, NH<sub>2</sub>, NO<sub>2</sub> or Br) were synthesized and compared for the oxidation of As(III) and reduction of Cr(VI) under visible light.<sup>43</sup> As listed in Table 2, the photocatalytic performance of the as-prepared UiO-66 MOFs was strongly affected by different functionalized linkers. Among the four tested sample, -NH<sub>2</sub> functionalization displayed highest photocatalytic activity for either As(III) oxidation or Cr(VI) reduction. For example, As(III) can be 100% removed by UiO-66-X (X = NH<sub>2</sub>), while the value was 60%, 18% or 50% for -H, -NO<sub>2</sub> or -Br functionalized UiO-66, respectively.<sup>43</sup> In comparison with unmodified UiO-66, the absorption edges were red-shifted to ca. 360, 400 and 450 nm for UiO-66-X (X = Br, NO<sub>2</sub> and NH<sub>2</sub>), respectively. Correspondingly, decreased band gaps were estimated from 3.88 to 2.76 eV.

**Table 2** Ligand functionalization of typical MOFs for photocatalytic removal of environmental pollutants under visible light.

MOFs	<sup>a</sup> <i>E</i> <sub>HOMO-LUMO</sub> (eV)	<sup>b</sup> <i>S</i> <sub>BET</sub> (m <sup>2</sup> /g)	Pollutant	<i>C</i> <sub>pollutant</sub> (mg/L)	<i>C</i> <sub>catalyst</sub> (g/L)	Time (min)	<sup>c</sup> <i>η</i> (%)	Ref.
<b><u>UiO-66(Zr)-X: X substituted H<sub>2</sub>BDC as ligand precursor</u></b>								
X = H	3.88	1141	As(III) <sup>d</sup>	2	1.0	60	64	43
X = NH <sub>2</sub>	2.76	733		2	1.0	60	100	
X = NO <sub>2</sub>	3.10	465		2	1.0	60	18	
X = Br	3.44	456		2	1.0	60	50	
X = H	3.88	1141	Cr(VI) <sup>d</sup>	10	0.5	100	20	43
X = NH <sub>2</sub>	2.76	733		10	0.5	100	100	
X = NO <sub>2</sub>	3.10	465		10	0.5	100	11	
X = Br	3.44	456		10	0.5	100	15	
<b><u>MIL-68(In)-X: X substituted -H<sub>2</sub>BDC as ligand precursor</u></b>								
X = H	3.94	611	Cr(VI) <sup>d,e</sup>	20	1.0	60	16	81
X = NH <sub>2</sub>	2.79	584		20	1.0	60	100	
X = NO <sub>2</sub>	3.02	582		20	1.0	60	<5	
X = Br	3.70	601		20	1.0	60	8	
<b><u>NH<sub>2</sub>-MOFs: NH<sub>2</sub> functionalization with different metal centers</u></b>								
MIL-125(Ti)	NA	NA	Cr(VI)	8	0.5	45	60	82
MIL-53(Fe)	NA	NA		8	0.5	45	17	
MIL-88B(Fe)	NA	NA		8	0.5	45	100	
UiO-66(Zr)	NA	NA		8	0.5	45	46	
<b><u>Development of NH<sub>2</sub> functionalization</u></b>								
NH <sub>2</sub> -MIL-101(Fe)	1.32	NA	Toluene	27.6	0.16	360	79	33
NH <sub>2</sub> -UiO-66(Zr) film	2.90	NA	Cr(VI)	5	0.5	120	98	83
NH <sub>2</sub> -UiO-66(Hf) film	2.88	NA	Cr(VI)	5	0.9	120	99	83
Hierarchical NH <sub>2</sub> -MIL-125(Ti)	2.53	1133	RhB	100	0.4	120	84	84
NH <sub>2</sub> -MIL-125(Ti)	2.64	1129	NO	NA	0.4	5	31	85
NH <sub>2</sub> -MIL-125(Ti)	2.75	1344	Cr(VI) <sup>f</sup>	48	0.4	60	91	86
MIL-68(In)-NH <sub>2</sub>	2.82	674	Cr(VI) <sup>g</sup>	20	1.0	180	97	87
<b><u>Other groups functionalization</u></b>								
NTU-9 <sup>i</sup>	1.72	NA	RhB <sup>h</sup> MB <sup>h</sup>	48 32	0.5 0.5	80 20	100 100	76

NA: no experimental data available; <sup>a</sup> *E*<sub>HOMO-LUMO</sub> was used received or estimated from the adsorption edges of MOFs; <sup>b</sup> *S*<sub>BET</sub> surface area were presented in integer numbers; <sup>c</sup> Removal efficiencies (*η*) for pollutants were used received or estimated from the figures in reference and presented in integer numbers; <sup>d</sup> UV-Vis light or sunlight; <sup>e</sup> Addition of ammonium oxalate under N<sub>2</sub> atmosphere; <sup>f</sup> Addition of ethanol; <sup>g</sup> Addition of ethanol under N<sub>2</sub> atmosphere; <sup>h</sup> Addition of H<sub>2</sub>O<sub>2</sub>; <sup>i</sup> (OH)<sub>2</sub>-H<sub>2</sub>BDC as organic ligand.

However, the photocatalytic performance for both As(III) oxidation and Cr(VI) reduction were not correlate with band gaps. Only  $-\text{NH}_2$  functionalization enhanced the photocatalytic performance, while  $-\text{NO}_2$  and  $-\text{Br}$  had an inhibitory effect. Based on further exclusion of the influence of specific surface area, the above phenomena can be explained by electronic effects of ligands. As shown in Fig. 10, the  $\log(K_X/K_H)$  correlated well with the Hammett's  $\sigma_m$  values of different X ligands. Herein,  $K_X$  and  $K_H$  represented rate constant for As(III) oxidation by UiO-66-X and UiO-66 respectively. The electron-donating group ( $-\text{NH}_2$ ) with negative  $\sigma_m$  can enhance the electron density around Zr-O cluster, leading to promoted separation and transfer of photogenerated charge carriers. Whereas, the electron-withdrawing groups ( $-\text{NO}_2$  and  $-\text{Br}$ ) had an opposite effect. Thus, rather than surface area or band gap, electronic effect was considered to play dominating rule in affecting the photocatalytic performance of UiO-66-X. Subsequently, the electronic effects of ligand substitution were also demonstrated by functionalized MIL-68(In) for the photocatalytic treatment of Cr(VI)-containing wastewater.<sup>81</sup>

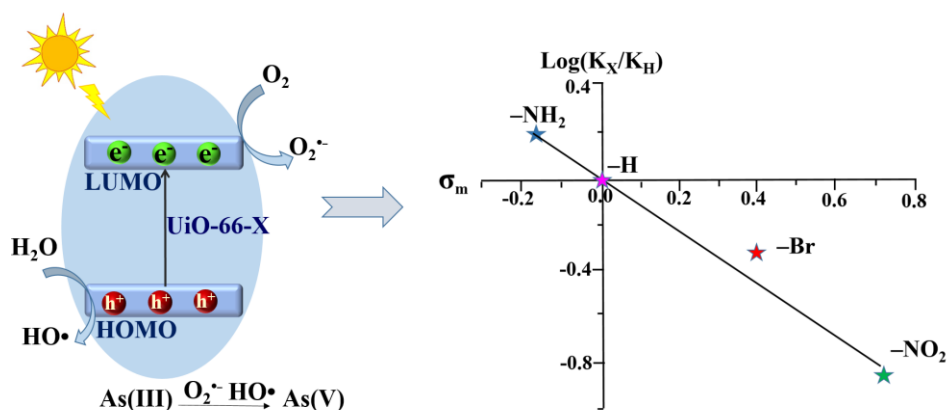
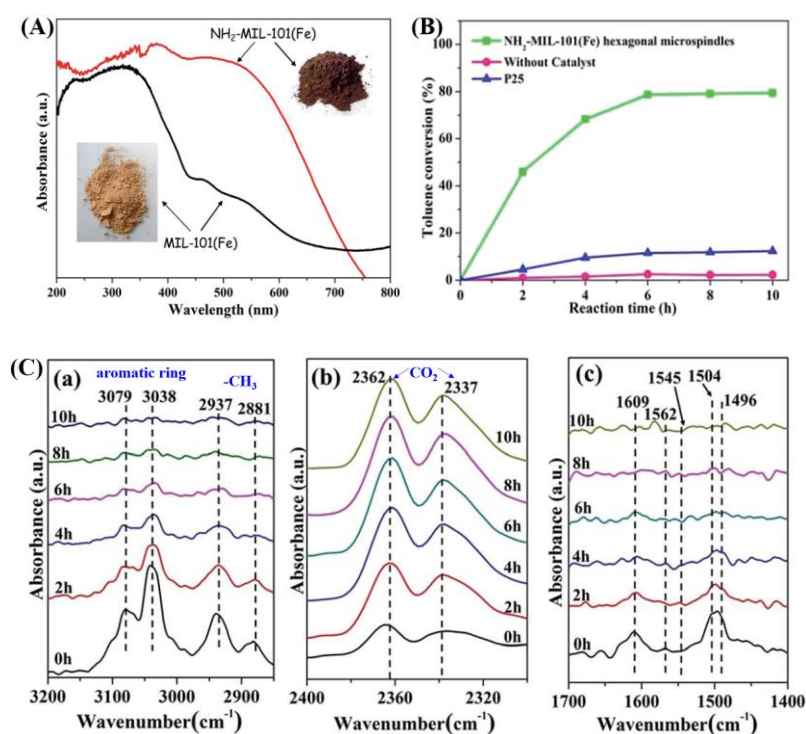


**Fig. 10.** Proposed mechanism (left) and Hammett plot (right) for photocatalytic oxidation of As(III) by UiO-66-X (X = H,  $\text{NH}_2$ ,  $\text{NO}_2$  or Br). Reproduced from Ref. <sup>43</sup> with permission from the PCCP Owner Societies.

In addition to UV-active MIL-125(Ti) and UiO-66(Zr),  $-\text{NH}_2$  functionalization was also applied to Fe-containing MOFs. Similarly, enhanced visible light absorption and photocatalytic performance can be observed. Moreover, the effect of  $-\text{NH}_2$  functionalization on different MOFs were further investigated.<sup>82</sup> For example, the performance of  $\text{NH}_2$ -MIL-88B(Fe),  $\text{NH}_2$ -MIL-125(Ti) and  $\text{NH}_2$ -UiO-66(Zr) were compared for the reduction of aqueous Cr(VI). Among which,  $\text{NH}_2$ -MIL-88B(Fe) displayed highest activity. Cr(VI) can be totally reduced by  $\text{NH}_2$ -MIL-88B(Fe) within 45 min visible light irradiation (Table 2). Whereas, the values were 60% and 46% by

$\text{NH}_2\text{-MIL-125(Ti)}$  and  $\text{NH}_2\text{-UiO-66(Zr)}$ , respectively. The superior performance of  $\text{NH}_2\text{-MIL-88B(Fe)}$  can be explained by dual excitation pathways. Namely, both  $\text{Fe-O}$  clusters and  $-\text{NH}_2$  group can be excited. The electron transfer from the excited  $-\text{NH}_2$  to  $\text{Fe-O}$  center led to promoted separation of photogenerated charge carriers, as well as enhanced  $\text{Cr(VI)}$  reduction.

Moreover,  $-\text{NH}_2$  functionalized  $\text{Fe-MOFs}$  also displayed potential application in air purification. For example, Zhang et al. demonstrated that hexagonal  $\text{NH}_2\text{-MIL-101(Fe)}$  spindles can be applied for the visible light-induced degradation of gaseous toluene.<sup>33</sup> As shown in Fig. 11A,  $\text{NH}_2$ -functionalization dramatically enhanced the visible light absorption of  $\text{MIL-101(Fe)}$ , corresponding to decreased band gap (1.32 eV). After 6 h visible light irradiation, ca. 79% toluene can be degraded by  $\text{NH}_2\text{-MIL-101(Fe)}$ . Whereas, the value was ca. 11% by  $\text{TiO}_2$  (Fig. 11B). The mechanism for toluene degradation was revealed using *in situ* FTIR technique (Fig. 11C). Characteristic peaks corresponding to aromatic ring ( $3079$  and  $3038\text{ cm}^{-1}$ ) and methyl groups ( $2937$  and  $2881\text{ cm}^{-1}$ ) in toluene gradually decreased with prolonged irradiation time. Meanwhile, peaks of  $\text{CO}_2$  ( $2362$  and  $2337\text{ cm}^{-1}$ ) gradually increased. The formation of degradation intermediate (benzoic acid) was also deduced *via* the signals of carboxylate group ( $1504$ ,  $1545$  and  $1562\text{ cm}^{-1}$ ). Thus, the oxidative degradation of toluene to  $\text{CO}_2$  can be confirmed (Fig. 11D).



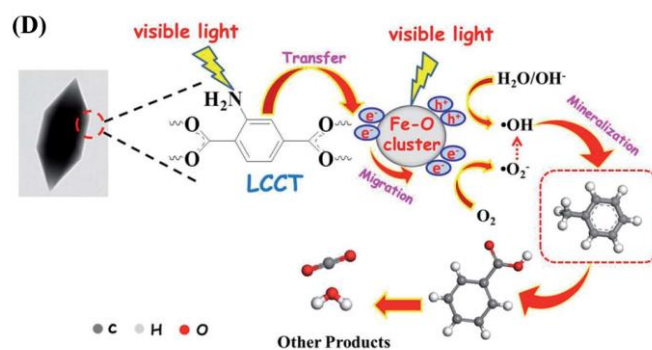


**Fig. 11.** (A) UV-Vis DRS of MIL-101(Fe) and NH<sub>2</sub>-MIL-101(Fe); (B) Photocatalytic degradation dynamics of toluene; (C) *In situ* FTIR spectra of toluene at different irradiation time by NH<sub>2</sub>-MIL-101(Fe); (D) Proposed mechanism for toluene degradation by NH<sub>2</sub>-MIL-101(Fe) under visible light. Adapted from Ref. <sup>33</sup> with permission from The Royal Society of Chemistry.

### 3.2 Mixed-metal/linker strategy

Due to the versatility and flexibility of MOFs, mixed-metal/linker strategy have been developed for preparing more efficient MOFs with desirable properties using more than one metal (mixed-metal) center or/and more than one organic linker (mixed-linker), respectively.<sup>88-92</sup> Typically, additional metal ions or linkers can be introduced into a MOF structure through solvothermal or post-synthetic modification approach.<sup>92</sup> The as-prepared MOFs with mixed components exhibited unique and superior catalytic activity relative to pristine MOFs with single component. Due to more types of active sites, enhanced photocatalytic performance may be anticipated.<sup>93</sup>

As for MOFs with mixed metals,<sup>90</sup> partial substitution of metal centers could regulate the efficiency for charge separation as well as photocatalytic performance.<sup>92, 94-106</sup> Oxo-bridged heterometallic assemblies with more flexibility and tenability can be formed within the same MOFs.<sup>92, 99</sup> For example, Ni-doped ZIF-8 were fabricated *via* a one-pot mechanochemical method.<sup>100</sup> The active Ni(II) centers in the backbones of ZIF-8 can regulate the light absorption region from UV to visible light. Under visible light irradiation, Ni-doped ZIF-8 with purple color can be excited, leading to efficient degradation of MB dye within 25 min, whereas, pristine ZIF-8 with white color displayed negligible activity. Besides, Cu<sup>2+</sup> was successfully doped into the structure of ZIF-67 *via* initially mixing Cu(COO)<sub>2</sub>, Co(COO)<sub>2</sub> and 2-methylimidazole with organic solvent followed by solvothermal procedure at 140 °C for 7 days.<sup>98</sup> The as-prepared Cu-doped ZIF-67 (Cu/ZIF-67) displayed significantly enhanced performance for methyl orange (MO) degradation under visible

light. Recently, Cu doped NH<sub>2</sub>-MIL-125(Ti) was also developed for enhanced photocatalytic degradation of MO and phenol.<sup>101</sup> At optimal Cu doping amount (1.5 wt%), the estimated rate constants for MO and phenol were 10.4 and 3.4 times relative to that on pristine NH<sub>2</sub>-MIL-125(Ti), respectively. As shown in Fig. 12, the doping of Cu<sup>2+</sup> will introduce a shallow state below the position of LUMO, which may trap electrons from LUMO and transfer it to other electron acceptors via Cu<sup>2+</sup>/Cu<sup>+</sup> redox cycle. In this way, the recombination of charge carriers can be greatly inhibited.

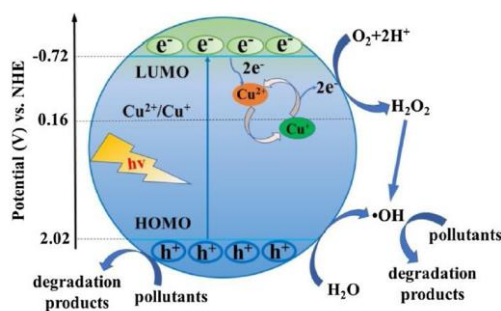


**Fig. 12.** Proposed mechanism for electron transfer pathways during the degradation of pollutants by Cu doped NH<sub>2</sub>-MIL-125(Ti) under visible light. Adapted with permission from ref. <sup>101</sup>, © 2018 Elsevier B. V.

Besides, Ti substituted UiO-66-NH<sub>2</sub>(Zr) was achieved by post-synthetic exchange method.<sup>94, 95</sup> The as-prepared UiO-66-NH<sub>2</sub>(Zr/Ti) exhibited enhanced photocatalytic performance for CO<sub>2</sub> reduction and H<sub>2</sub> production, which was ascribed to the presence of Ti<sup>4+</sup> as an electron mediator. Furthermore, Yasin and co-workers carried out theoretical DFT calculations of band gaps for UiO-66-X (X: H, NO<sub>2</sub> or NH<sub>2</sub>) with different ratio of mixed metallic centers (Zr, Ti or Hf).<sup>107</sup> Results indicated that the band gap decreased gradually with increasing percentage of Ti<sup>4+</sup> substitution. The lowest band gap (1.61 eV) was calculated on fully substituted Ti-BDC-NH<sub>2</sub>. Despite of these, either the conventional solvothermal method or the post-synthetic exchange approach took too long time (up to days or even weeks)<sup>108</sup>. To overcome this barrier, microwave-assisted method was recently developed due to much shorter reaction time and lower energy consumption.<sup>109, 110</sup> For example, Ti substituted UiO-66-NH<sub>2</sub> could be fabricated within a few hours with well-maintained crystallinity and enhanced photocatalytic activity.

Similar to MOFs with mixed metals, MOFs with mixed linkers were also developed as unique photocatalysts. Using NH<sub>2</sub>-BDC and X-BDC (X: H, F, Cl, Br) as primary and secondary linker, respectively, a series of Zr-based MOFs were synthesized in one-pot reactions.<sup>111</sup> The introducing of X-BDC with electron-withdrawing halogen group can lead to enhanced photocatalytic performance

for alcohol oxidation, among which, Zr-MOF with NH<sub>2</sub>-BDC and F-BDC mixed linkers behaved highest performance.

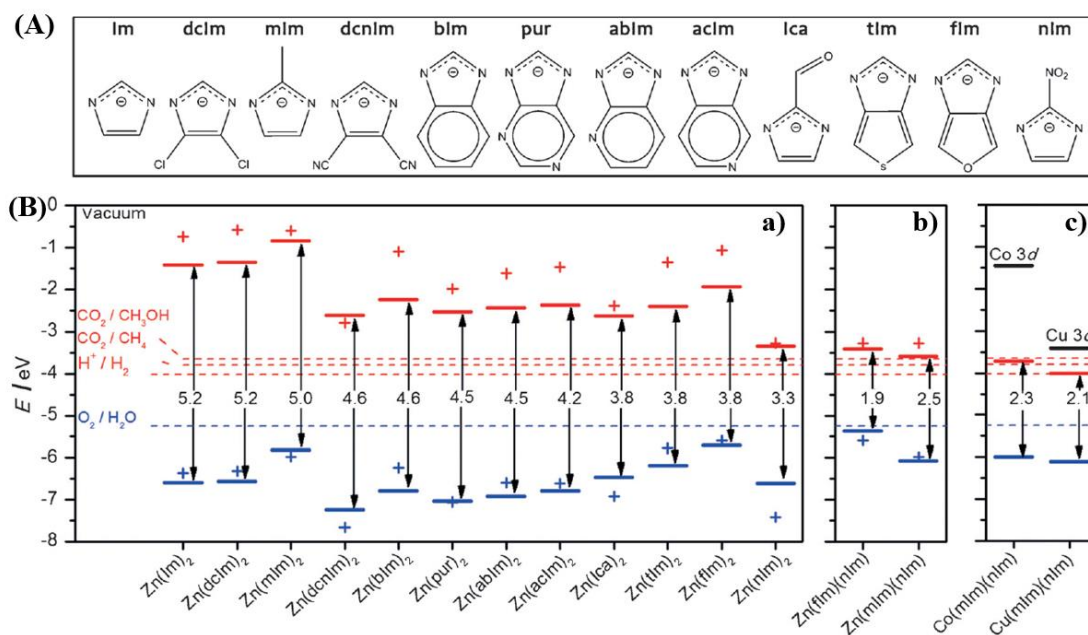


**Fig. 13.** (A) The chemical structures of different organic linkers (X) for constructing ZnX<sub>2</sub> MOF; (B) Calculated HOMO (blue) and LUMO (red) positions of ZnX<sub>2</sub> crystal structures (lines) and isolated HX molecules (crosses): a) ZnX<sub>2</sub> with different combination of organic ligands; b) Equivalent plot for ZnX<sub>2</sub> created by combining of flm or mIm with nIm linkers; c) Equivalent plot for Co(mIm)(nIm) and Cu(mIm)(nIm). Adapted with permission from ref. <sup>112</sup>, © 2016 Wiley-VCH.

By computational predication, Grau-Crespo et al. reported a conceptually simple route to engineer the band edge positions of ZIFs using mixed organic linkers.<sup>112</sup> As illustrated in Fig. 13A, a series of organic linkers were calculated. Relatively wide band gaps (> 3.3 eV) can be observed using single type of organic linker (Fig. 13B), indicating unachievable excitation by visible light. Whereas, the band gap dramatically decreased to 1.9 eV and 2.5 eV for ZnX<sub>2</sub> by combining of flm or mIm with nIm linkers. The predicated band positions were theoretically ideal for visible light-induced CO<sub>2</sub> reduction and water splitting. Moreover, they also calculated the influence of metal ion doping. Cu<sup>2+</sup> doping would led to narrower band gap with increased photo-absorption and e<sup>-</sup>-h<sup>+</sup> recombination times, which was consistent with the experimental results in mixed-metal strategy.

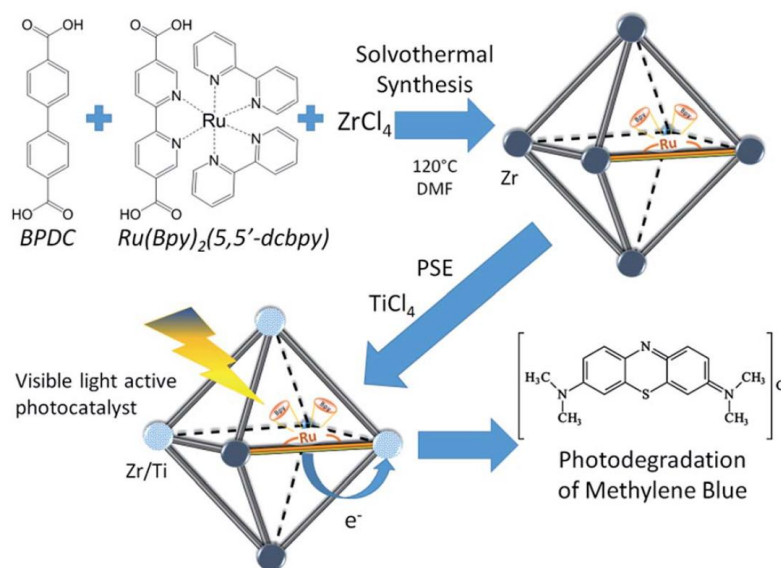


**Fig. 14.** Schematic processes for preparing UiO-67–Ru–Ti MOF and its application.<sup>113</sup> Adapted with permission from ref. <sup>113</sup>, © 2017 Elsevier B.V.

The combinations of mixed-metal and mixed-ligand strategies were also developed. For example, Amador et al. reported the synthesis of UiO-67–Ru–Ti MOF through the combination of two pathways (Fig. 14).<sup>113</sup> Firstly, 4,4'-biphenyldicarboxylic acid (BPDC) and Ru(Bpy)<sub>2</sub>(5,5'-dcbpy) were applied in the solvothermal process, which acted for the structure and light-absorbing antenna, respectively. Subsequently, Zr<sup>4+</sup> was partially substituted by Ti<sup>4+</sup> *via* post-synthetic exchange. The as-prepared UiO-67–Ru–Ti MOF was evaluated by the degradation MB dye. Dramatically enhanced performance can be observed under visible light relative to UiO-67–Ru or UiO-67–Ti with single modification strategy.

### 3.3 Metal ions/ligands immobilization

In addition to functional group modification, implantation of transition metal ions to complex with ligand was reported to be a feasible way for enhanced photocatalytic performance.<sup>114, 115</sup> For example, the implantation of Fe<sup>3+</sup> in porphyrinic MOFs (PCN-224) were achieved *via* post synthetic reaction between pristine MOFs and FeCl<sub>3</sub> in DMF solution.<sup>114</sup> As illustrated in Fig. 15A, the unsaturated Fe<sup>3+</sup> was implanted into porphyrin unit, leading to the formation of Fe@PCN-224. The uniform distribution of Fe in FCN-224 can be further confirmed by HAADF-STEM (high-angle annular dark-field scanning TEM) and corresponding elemental mapping images (Fig. 15B). After Fe<sup>3+</sup> implantation, the optical response was extended to longer wavelength, and the recombination of



$e^-h^+$  pairs was inhibited, which were revealed by UV-Vis Diffuse Reflectance Spectroscopy (UV-Vis-DRS), photoluminescence (PL) and fluorescence lifetime measurements. Besides, the introduction of additional  $Fe^{3+}$  can also promote the activation of in-situ generated  $H_2O_2$ , leading to more active  $O_2^{\cdot-}$  and  $HO\cdot$  species. Thus, the photooxidation of gaseous isopropanol (IPA) was significantly boosted on Fe@PCN-224. The generation rate for degradation intermediate (acetone) and product ( $CO_2$ ) exhibited an 8.9 and 9.3 times enhancement relative to pristine PCN-224, respectively (Fig. 15C-D). Good stability for Fe@PCN-224 can be deduced from cyclic experiments (Fig. 15E). Besides, this strategy was also applicable for the modification of another porphyrinic MOF (PCN-222), which exhibited similar behaviors. Different from Fe(III) complex in porphyrin unit, the immobilization of Bi(III) in MIL-101(Cr) via two-step hydrolysis route led to the formation of small Bi-oxoclusters inside the mesocages of MIL-101.<sup>115</sup> The complete photodegradation of methyl red (MR) can be easily achieved by the as-prepared Bi(III)@MIL-101(Cr) composite.

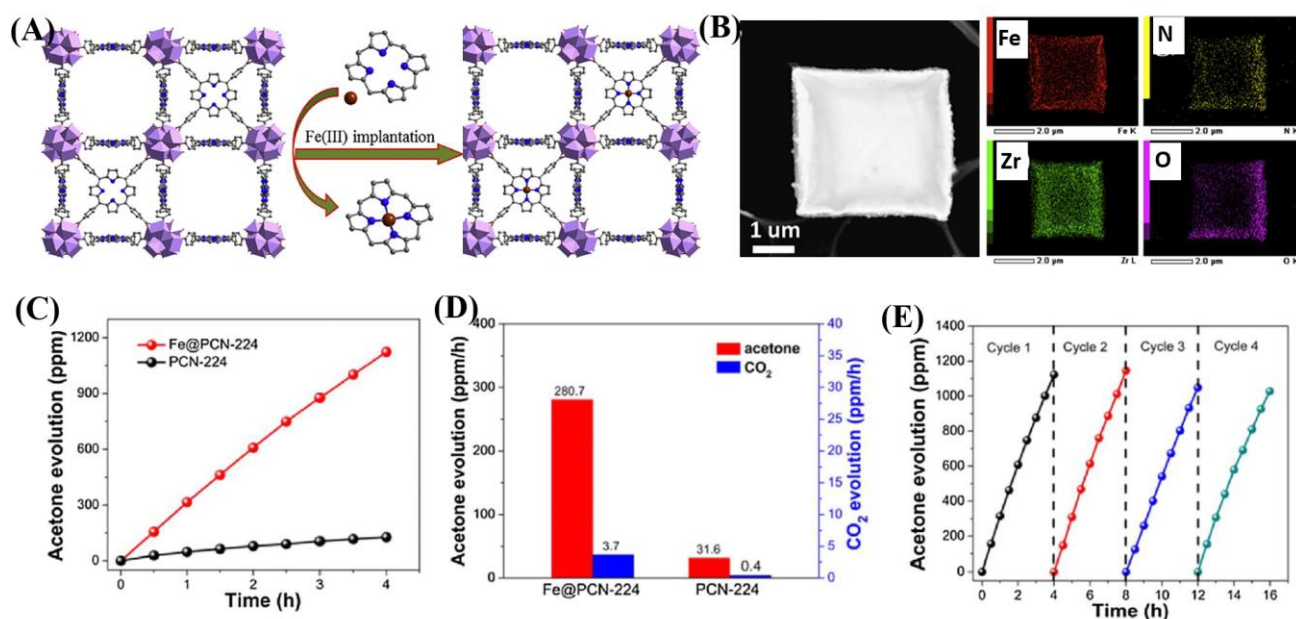


**Fig. 15.** (A) Schematic illustration for implanting  $Fe^{3+}$  into porphyrin unit of PCN-224; (B) HAADF-STEM image of Fe@PCN-224 and its corresponding elemental mapping images; (C) Time-dependent acetone evolution and (D) Evolution rate of acetone and  $CO_2$  during photocatalytic oxidation of IPA by PCN-224 and Fe@PCN-224; (E) Cyclic photocatalytic evolution of acetone by Fe@PCN-224. Adapted with permission from ref.<sup>114</sup>, © 2017 Elsevier B.V.

Starting from the characteristics of pollutants, the implantation of appropriate substance that can accumulate pollutant on the surface or in the tunnel of MOFs have also been verified as an efficient

way. For example, due to selective binding with radiative U(VI), phosphonate was previously verified as efficient ligand for functional materials in adsorptive remediation of uranyl. Recently, Wang's group reported the post-synthetic modification of Zr-clusters in PCN-222 with aminomethylphosphonic acid (PN-PCN-222) and ethanephosphonic acid (P-PCN-222).<sup>116</sup> It can be deduced from Fig. 16A that the morphology of PCN-222 was well maintained after ligand incorporation. Besides, phosphonic acids are chemically grafted onto the Zr clusters. Due to simultaneous selective complexation and photocatalytic reduction, U(VI) can be completely removed with extremely wide concentration range (from 1 to 400 ppm). As shown in Fig. 16B, PN-PCN-222 (0.5 g/L) behaved highest performance for U(VI) removal (756.1 mg/g). At lower catalyst dosage (0.25 g/L), the uptake amounts for U(VI) were 184.2 and 1289.3 mg/g under dark and visible light, respectively. Moreover, the PN-PCN-222 exhibited stable photocatalytic performance and recyclability for U(VI) removal (Fig. 16C).

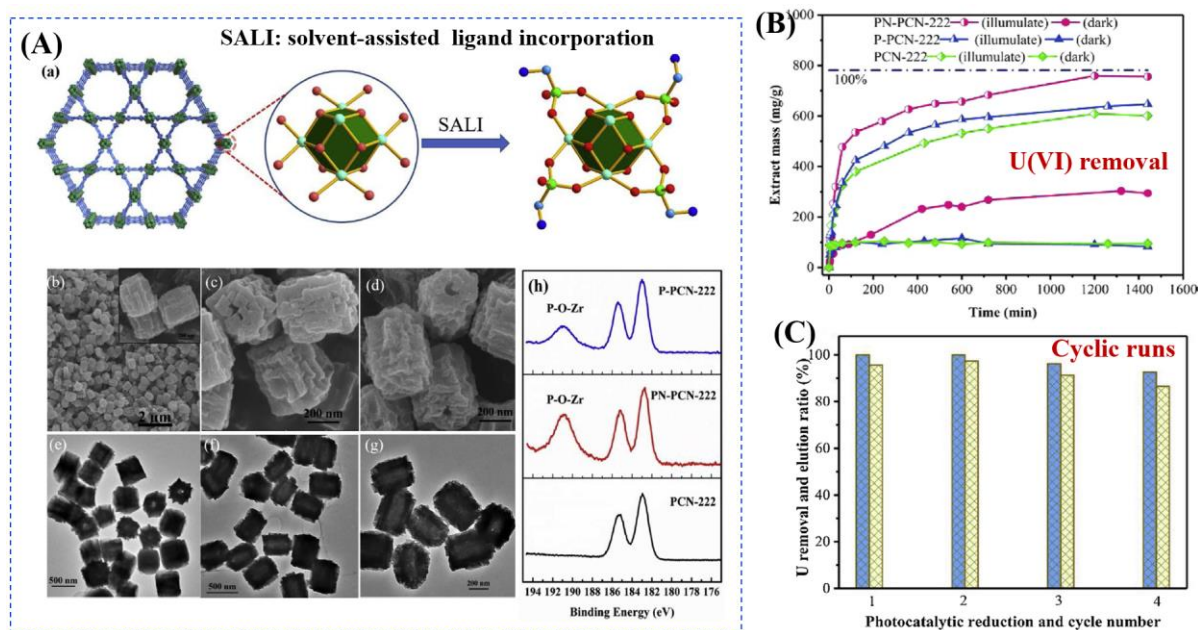


**Fig. 16.** (A) Schematic representation for modification of PCN-222 (Zr: green; P: bottle green; C: Cambridge blue; O: red; N: blue; H atoms are omitted) (a); SEM and corresponding TEM images of PCN-222 (b, c), PN-PCN-222 (c, f), and P-PCN-222 (d, g); XPS spectra of Zr(IV) in different samples (h); (B) Uranium extraction (400 ppm) by different samples; (C) Cyclic extraction efficiency of U (10 ppm) via photoreduction method (left axis) and elution 0.1M HCl (right axis). Adapted with permission from ref. <sup>116</sup>, © 2019 Elsevier B.V.

### 3.4 Dye sensitization

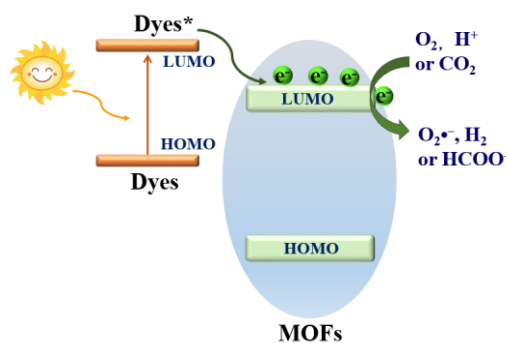


**Fig. 17.** Electron transfer pathway in dye sensitized MOFs (wide band gap) system.

Dye sensitization was a mature way for harvesting more incident solar light, which is well known in dye-sensitized solar cells (DSSC). Different from the traditional semiconductor-based system, a strong  $\pi$ - $\pi$  stacking as well as Van Der Waals interaction may be expected in dye-sensitized MOFs due to extensive presence of benzene ring in both the organic linker of MOFs and dyes. Inspired by this, dye-sensitized photocatalysis was further developed using MOFs as substrate. Specific dyes can be selected to form a complex with MOFs. As shown in Fig. 17, dye molecules in the ground state can absorb incident light and be transformed into excited state (dye<sup>\*</sup>). As long as the potential of dye<sup>\*</sup> is more negative than the LUMO position of MOFs, electron injection from dye<sup>\*</sup> to the LUMO of MOFs will be feasible. Finally, the electrons can be transferred to different acceptors ( $O_2$ ,  $H^+$  or  $CO_2$ ) leading to the formation of active  $O_2^{\bullet-}$ ,  $H_2$  or  $HCOO^-$ , respectively. In this way, the excitation wavelength can be extended to visible light. At the beginning, many researches were focused on  $H_2$  production and  $CO_2$  reduction.<sup>75, 117-122</sup> Recently, dye-sensitized MOFs were gradually applied in the field of environmental remediation.<sup>123-126</sup>

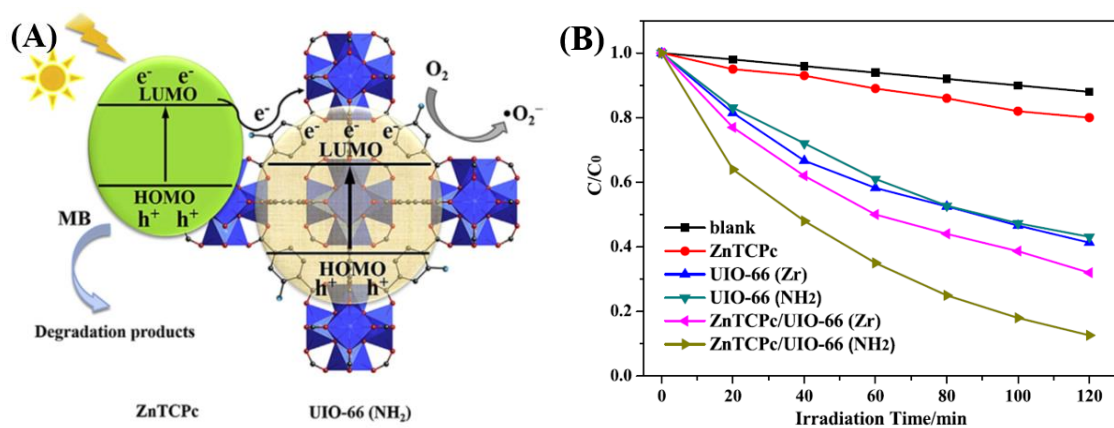


**Fig. 18.** (A) Proposed mechanism for the degradation of MB by ZnTCpC/UIO-66(NH<sub>2</sub>) under visible light; (B)

Degradation dynamics of MB by different samples. Adapted with permission from ref. <sup>124</sup>, © 2016 Elsevier B.V.

For example, Zinc phthalocyanine (ZnTCPc) was applied to form complex with UiO-66 and UiO-66(NH<sub>2</sub>) *via* impregnation method.<sup>124</sup> As shown in Fig. 18, in comparison with pristine MOFs, the ZnTCPc modified samples both displayed enhanced visible light activity for MB degradation. Besides, due to the synergistic effect of visible light-responsive UiO-66(NH<sub>2</sub>), the degradation efficiency increased from 68% by ZnTCPc/UiO-66(Zr) to 89% by ZnTCPc/UiO-66(NH<sub>2</sub>) after 120 min visible light irradiation. In addition to metal-organic ZnTCPc dye, Thakare and Ramteke reported the post-modification of MOF-5 using 8-hydroxyquinoline (HOQ) dye for the degradation of colorless phenol.<sup>123</sup> After 80 min visible light irradiation, phenol (1mg/L) can be completely degraded using HOQ/MOF (4 g/L) as photocatalyst. Whereas, less than 5% phenol was degraded using unmodified MOF-5, indicating the vital role of HOQ dye. Moreover, the photocatalytic performance remained well up to 5 cyclic runs. No difference was observed both in XRD and UV-Vis-DRS analysis, indicating the stability of HOQ/MOF-5 composite. Besides, Rhodamine B (RhB) dye, which was frequently reported as target dye pollutant, was also applied to sensitize MIL-125(Ti) *via* post-impregnation method.<sup>127</sup> For the degradation of MO dye, boosted performance was observed from inactive MIL-125(Ti) to more than 90% on RhB/TiO<sub>2</sub> after 60 min visible light irradiation. Trichromatic dyes, such as Basic Yellow 24 (BY24), Basic Red 14 (BR14) or Methylene Blue (MB) were also encapsulated in Cu-MOFs. The as-prepared dyes@Cu-MOFs all exhibited enhanced performance for the degradation of large sized Reactive Blue 13 (RB13). Among which, MB@Cu-MOFs displayed highest activity. The reason was ascribed to the difference in visible light-absorption region. For example, MB covers 450–750 nm, which is broader than that of BR14 (380–580 nm) and BY24 (325–480 nm).

### 3.5 Metal nanoparticles loading

Due to the porous characteristics, photoactive guest species can be incorporated into the pore spaces or partially stabilized on the surface of MOFs. Metal nanoparticles (MNPs), especially small noble MNPs with structural diversity and tailor ability, are promising guest species. As a typical design, the encapsulation of MNPs into the cavity of MOFs can regulate the size and enhance the stability of MNPs. Up to now, the MNPs/MOFs composites have displayed great potential in

photocatalysis.<sup>29, 128-131</sup> Herein, due to low Fermi energy levels, the MNPs co-catalyst were reported to serve as electron acceptor and mediator. Sometimes, they can also enhance the visible and/or NIR light absorption. For example, due to the localized surface plasmon resonance (LSPR) effect, the loading of noble MNPs led to enhanced visible light absorption and excitation.<sup>132-134</sup>

For photocatalytic elimination of environmental pollutants, Pd nanoparticles (3 to 6 nm in diameter) were immobilized and highly dispersed in NH<sub>2</sub>-UiO-66(Zr) via one-pot hydrothermal method. The as-prepared Pd@NH<sub>2</sub>-UiO-66(Zr) composite displayed reusable and highly enhanced photocatalytic activity for Cr(VI) reduction.<sup>135</sup> As listed in Table 3, at catalyst dosage of 0.5 g/L and after 90 min visible light irradiation, the removal efficiency for Cr(VI) increased from 33% to 99% after Pd loading. Besides, the BET surface area slightly increased from 756 to 837 m<sup>2</sup>/g, indicating more surface active sites. Moreover, the addition of organic dye (MB or MO) can further promote the reduction of Cr(VI). In this way, dye oxidation and Cr(VI) reduction can be simultaneously achieved by photogenerated electrons (e<sup>-</sup>) and holes (h<sup>+</sup>), respectively.

**Table 3** Photocatalytic removal of environmental pollutants by MNPs/MOFs composites under visible light.

MNPs/MOF	<sup>a</sup> S <sub>BET</sub> Variation (m <sup>2</sup> /g)	Pollutant	C <sub>pollutant</sub> (mg/L)	C <sub>catalyst</sub> (g/L)	Time (min)	<sup>b</sup> η Variation (%)	Ref.
Pd@NH <sub>2</sub> -UiO-66(Zr)	756→837	Cr(VI)	10	0.5	90	36→99	135
Pd@MIL-100(Fe)	2006→2102	Theophylline <sup>c</sup>	20	0.125	150	82→100	136
		Ibuprofen <sup>c</sup>	20	0.125	150	67→100	
		Bisphenol A <sup>c</sup>	20	0.125	240	35→66	
Pd@MIL-100(Fe)	2007→1898	MO <sup>c</sup>	20	0.125	40	41→84	137
		Cr(VI) <sup>d</sup>	20	1.0	8	69→100	
Pt@MIL-100(Fe)	2007→1724	MO <sup>c</sup>	20	0.125	40	41→100	137
		Cr(VI) <sup>d</sup>	20	1.0	8	69→86	
Pt/NH <sub>2</sub> -MIL-125(Ti)	1052→896	Cr(VI)	15	1.0	120	41→77 <sup>e</sup>	138
Pt/NH <sub>2</sub> -MIL-125(Ti)	1101→910	Nitrobenzene <sup>f</sup>	3075	6.25	1200	NA→98	139
Au@MIL-100(Fe)	2007→1822	MO <sup>c</sup>	20	0.125	40	41→65	137
		Cr(VI) <sup>d</sup>	20	1.0	8	69→82	
Ag@MOF-5	NA	E. coli	NA	NA	70	28→91	34
Ag@MIL-125(Ti)	NA	RhB	NA	1.0	40	8→93	140
Ag/MIL-125(Ti)-AC	1245→977	MB	20	0.06	30	55→100 <sup>g</sup>	141

Ag/Uio-66-NH <sub>2</sub>	NA	Cr(VI)	10	1.0	105	40→90	142
PtPd@ZIF-8	1024→713	C <sub>2</sub> H <sub>4</sub>	100	NA	120	<5→93 <sup>e</sup>	143
CuPd@ZIF-8	1531→1259	Cr(VI)	20	0.2	60	22→89 <sup>e</sup>	144

NA: no experimental data available; <sup>a</sup>  $S_{\text{BET}}$  variation indicates the surface area of MOFs before and after loading MNPs; <sup>b</sup> Removal efficiencies ( $\eta$ ) for pollutants were used received or estimated from the figures in reference and presented in integer numbers,  $\eta$  variation indicated the performance of MOFs before and after loading MNPs; <sup>c</sup> Addition of H<sub>2</sub>O<sub>2</sub>; <sup>d</sup> Addition of ammonium oxalate; <sup>e</sup> UV-Vis light or solar light; <sup>f</sup> in acetonitrile with the addition of TEOA; <sup>g</sup> 100W daylight lamp.

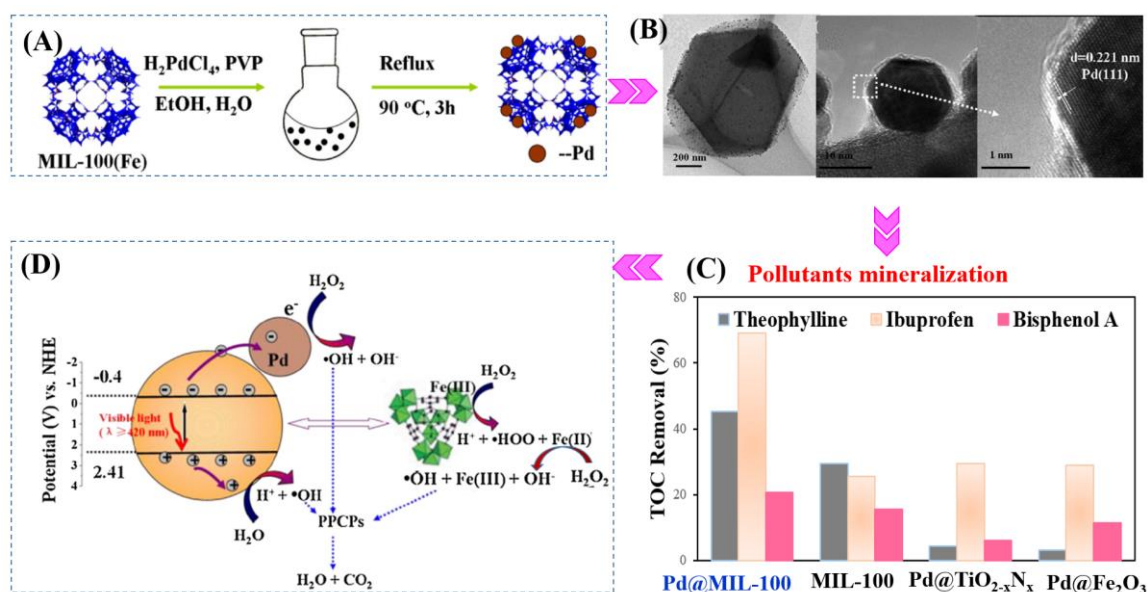


**Fig. 19.** (A) Schematic processes for preparing Pd@MIL-100(Fe) via a facile alcohol reduction method; (B) TEM and HRTEM images of Pd@MIL-100(Fe); (C) TOC Removal efficiency of Theophylline, Ibuprofen and Bisphenol A by different photocatalysts. Reaction conditions: 5 mg photocatalyst, 40 mL PPCPs (20 mg/L), 40  $\mu$ L H<sub>2</sub>O<sub>2</sub>, pH 4; (D) Proposed mechanism for visible-light-induced PPCPs degradation by Pd@MIL-100(Fe). Adapted with permission from ref. <sup>145</sup>, © 2015 Elsevier B.V.

Furthermore, Pd@MIL-100(Fe) with higher surface area were also fabricated (2102 m<sup>2</sup>/g).<sup>145</sup> As shown in Fig. 19A-B, using H<sub>2</sub>PdCl<sub>4</sub> as precursor, 1 wt% Pd nanoparticles (6 to 10 nm in diameter) with high dispersion were anchored on MIL-100(Fe) *via* a facile alcohol reduction method. The as-prepared brown Pd@MIL-100(Fe) powder displayed slightly enhanced absorption in visible light region relative to unmodified one. For the photocatalytic degradation of pharmaceuticals and personal care products (PPCPs), such as theophylline, ibuprofen and bisphenol A, Pd@MIL-100(Fe) displayed superior photocatalytic activity (Fig. 19C). The enhanced photocatalytic performance was

ascribed to more efficient separation of photogenerated  $e^-h^+$  pairs and easier transfer of interfacial charges induced by Pd loading. To gain more insight into the reaction, trapping experiments using different radical scavengers were further carried out, and the results indicated that  $HO\cdot$  played major role for PPCPs degradation. Thus, a proposed mechanism was displayed in Fig. 19D.

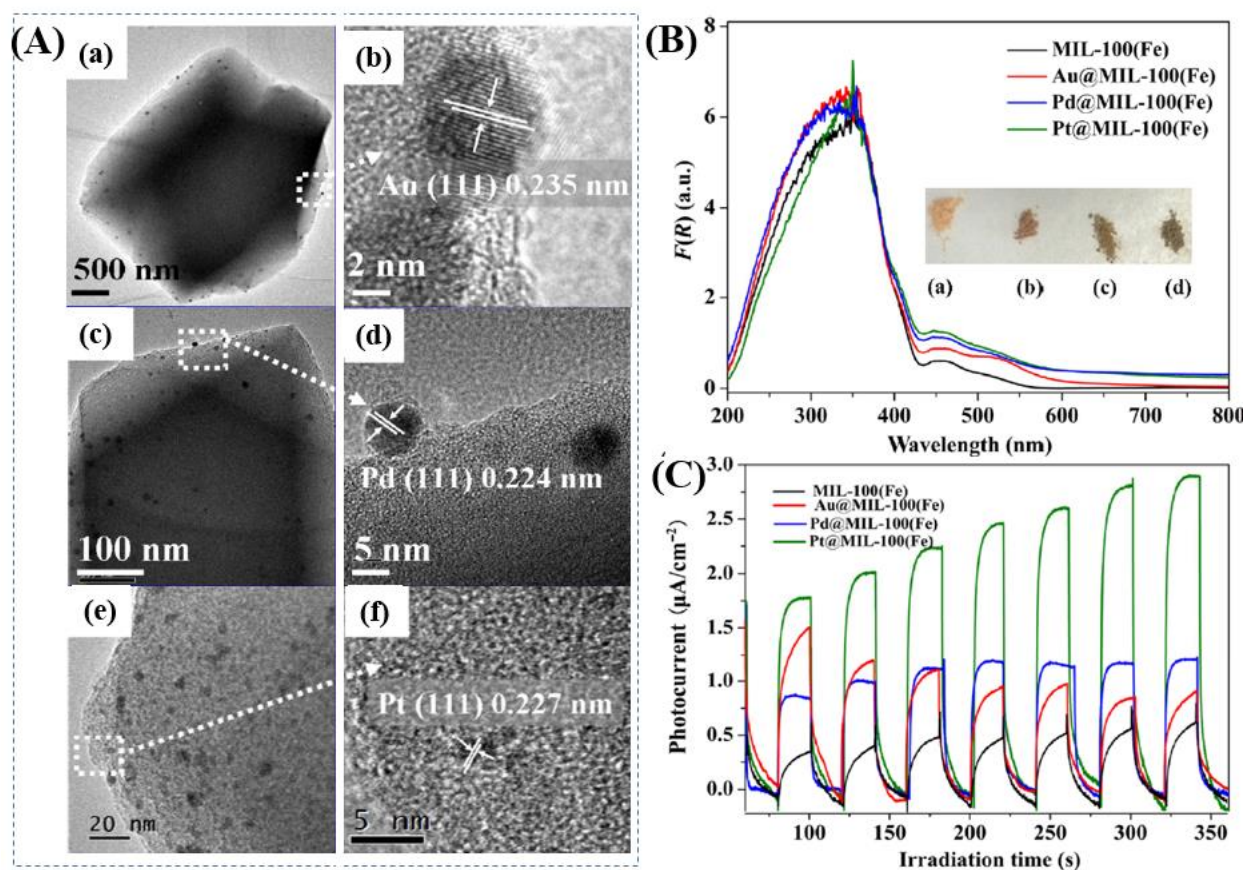


**Fig. 20.** (A) TEM and corresponding HRTEM images of (a, b) Au@MIL-100(Fe); (c, d) Pd@MIL-100(Fe); (e, f) Pt@MIL-100(Fe); (B) UV-vis DRS spectra and (D) Photocurrent response of MIL-100(Fe) and M@MIL-100(Fe). Adapted with permission from ref. <sup>137</sup>, © 2015 Springer.

Furthermore, Wu's group prepared a series of M@MIL-100(Fe) (M: Au, Pd or Pt) *via* a photochemical route and compared their photocatalytic performance under visible light.<sup>137</sup> Metal ion precursors can capture the photogenerated electrons in the LUMO of MIL-100(Fe), leading to reduction and deposition of corresponding MNPs on MIL-100(Fe) substrate. The average diameters were estimated to be 15, 12 and 2 nm for Au, Pd and Pt nanoparticles, respectively (Fig. 20A). The as-prepared M@MIL-100(Fe) were compared for photocatalytic removal of MO and Cr(VI) under visible light. Enhanced photocatalytic activity can be observed after loading different kinds of MNPs, among which Pt loading exhibited highest performance. The order of Pt@MIL-100(Fe) >

$\text{Pd@MIL-100(Fe)} > \text{Au@MIL-100(Fe)} > \text{MIL-100(Fe)}$  was consistent with the results in visible light absorption and photocurrent response (Fig. 20B-C), but in reverse order of surface area. Therefore, the presence of noble MNPs play crucial role in enhancing visible light absorption and prolonging lifetime of photogenerated charges, which together lead to boosted photocatalytic performance for removal of environmental pollutants.

Ag nanoparticles are also excellent electron sinks due to the formation of Ag-MOFs Schottky junction at interface. Thus, the  $e^-h^+$  recombination in MOFs can be greatly inhibited, leading to enhanced photocatalytic activity after loading Ag nanoparticles. For example,  $\text{Ag@MIL-125(Ti)}$  was fabricated through a facile photo-reduction method. The  $\text{AgNO}_3$  precursor can be photo-reduced to uniform Ag nanoparticles ( $\sim 40$  nm) and loaded onto the surface MIL-125(Ti). After 40 min of visible-light irradiation, about 8% RhB was degraded by pure MIL-125(Ti), whereas, the value was boosted to 93% by  $\text{Ag@MIL-125(Ti)}$ .<sup>140</sup> Simultaneously, the post-synthetic modification of  $\text{NH}_2\text{-MIL-125(Ti)}$  with acetylacetone (AC), led to the formation of MIL-125-AC, which were subsequently treated with  $\text{CH}_3\text{COOAg}$ .<sup>141</sup> In this way, smaller Ag nanoparticles, mostly 5–10 nm in size, were spread on the external surface and embedded within  $\text{NH}_2\text{-MIL-125(Ti)}$ . The as-prepared  $\text{Ag/MIL-125(Ti)-AC}$  displayed enhanced activity for photocatalytic degradation of MB dye.

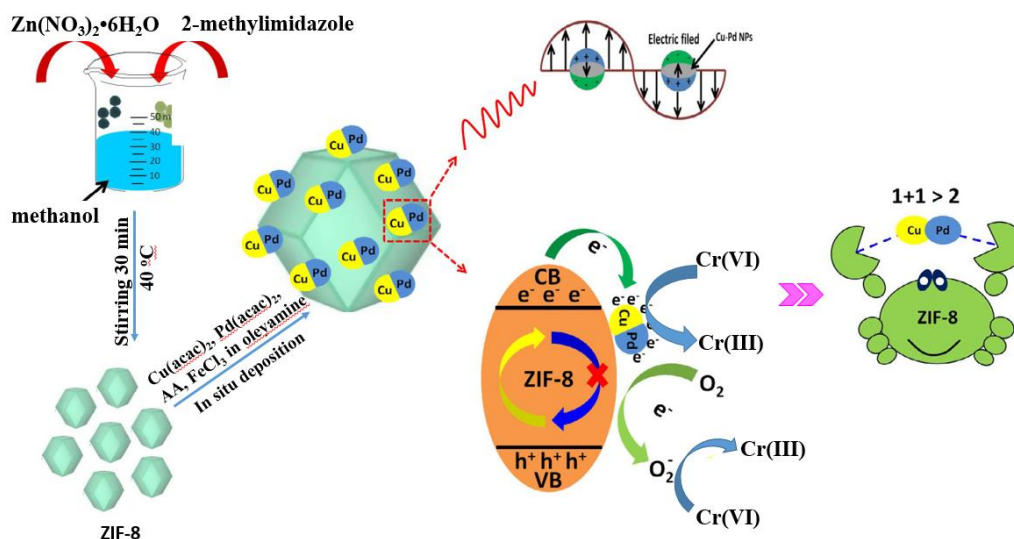


**Fig. 21.** Schematic processes for preparing  $\text{CuPd@ZIF-8}$  and proposed mechanism for photocatalytic reduction of  $\text{Cr(VI)}$ . Adapted by permission of ref. <sup>143</sup>, © 2014 The Royal Society of Chemistry.

In addition to single MNPs, bimetallic alloy nanocrystals were also encapsulated in MOFs for



photocatalytic applications. For example, PtPd alloy nanocrystals were encapsulated in microporous ZIF-8 with high dispersion (Table 3). Superior activity for the degradation of ethylene to CO<sub>2</sub> can be achieved.<sup>143</sup> Recently, CuPd alloy nanoparticles was dispersed on ZIF-8 with good stability for Cr(VI) reduction.<sup>144</sup> As shown in Fig. 21, CuPd@ZIF-8 was fabricated *via* a sol-gel method. Comparing with pristine ZIF-8, the loading of CuPd alloy led to enhanced adsorption capacity for O<sub>2</sub> and more photogenerate e<sup>-</sup>-h<sup>+</sup> pairs due to LSPR effect. Upon light irradiation, the photogenerated e<sup>-</sup> can be directly transferred to Cr(VI) or O<sub>2</sub>. Despite of the competition of O<sub>2</sub> in capturing e<sup>-</sup>, the reduction product of O<sub>2</sub> (O<sub>2</sub><sup>·-</sup>) will also contribute to Cr(VI) reduction, which finally led to boosted photocatalytic activity. After 60 min visible light irradiation, the efficiency for Cr(VI) reduction increased from 22% on pristine ZIF-8 to 89% on optimized CuPd@ZIF-8 with 5 wt% CuPd. Moreover, other control samples were also tested, which were in the order of CuPd@ZIF-8 > Cu@ZIF-8 > Pd@ZIF-8 > ZIF-8 > CuPd > Pd > Cu. Obviously, the CuPd alloy displayed synergistic effect comparing to single MNPs. Besides, the stability of the optimized CuPd@ZIF-8 maintained well (> 90%) after four successive cyclic runs.

### 3.6 Carbon material decoration

In traditional semiconductor photocatalytic systems, carbon materials with superior electrical conductivity were widely applied to form hybrid photocatalysts. The recombination of photogenerated charges can be suppressed after the loading of carbon materials.<sup>146-148</sup> For example, graphene oxide (GO), reduced graphene oxide (rGO), carbon quantum dots (CQDs), and etc. were typical carbon materials, which could accelerate the transfer of photogenerated charges. Similarly, coupling carbon materials with MOFs will also solve the disadvantageous of fast charge recombination in pristine MOFs, and lead to enhanced photocatalytic performance. As listed in Table 4, some typical carbon-MOFs composites were fabricated. No matter whether the specific surface area ( $S_{\text{BET}}$ ) is increased or decreased, carbon coupling all led to boosted photocatalytic performance for the elimination of environmental pollutants.

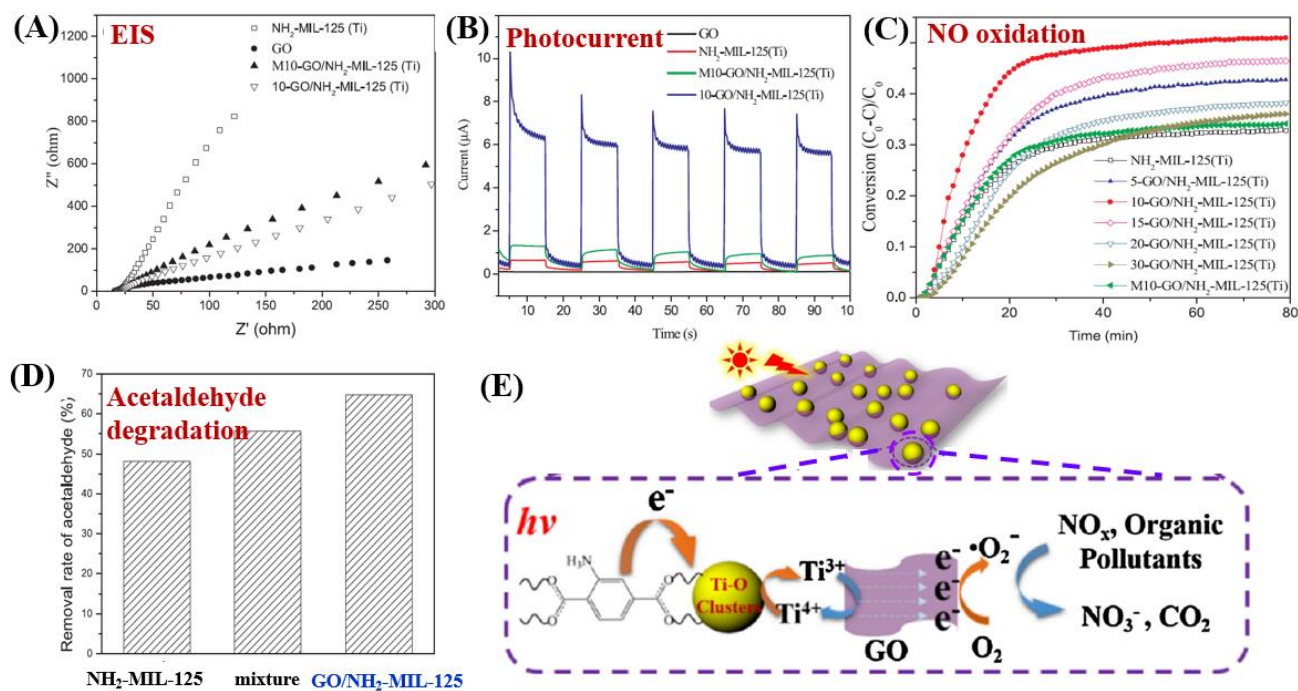
**Table 4** MOF–carbon composites for photocatalytic removal of environmental pollutants under visible light.

MOFs-based composite	Carbon Materials (wt%)	<sup>a</sup> S <sub>BET</sub> Variation (m <sup>2</sup> /g)	Pollutant	C <sub>pollutant</sub> (mg/L)	C <sub>catalyst</sub> (g/L)	Time (min)	<sup>b</sup> η Variation (%)	Ref.
MIL-53(Fe)	2.5% rGO	NA	MB	20	0.5	80	82→95	149
MIL-53(Fe)	0.5% rGO	NA	Cr(VI) <sup>c</sup>	20	1.0	80	79→100	150
NH <sub>2</sub> -MIL-68(In)	GO	530→681	AMX	20	0.6	10	60→93	151
MIL-88B(Fe)	10% GO <sup>c</sup>	NA→99	RR195 <sup>d</sup>	100	0.3	20	50→95 <sup>e</sup>	152
MIL-88(Fe)	3% GO <sup>c</sup>	NA	MB	100	0.5	10	48→95 <sup>e</sup>	153
			RhB				49→94 <sup>e</sup>	
NH <sub>2</sub> -MIL-125(Ti)	10% GO	871→501	NO	0.5	5	30	30→50	154
			CH <sub>3</sub> CHO	1.95	50	80	48→65	
NH <sub>2</sub> -MIL-125(Ti)	1% CQDs	487→198	RhB	10	0.5	240	67→100	155
NH <sub>2</sub> -UiO-66(Zr)	2% rGO	732→767	Cr(VI)	10	0.5	100	35→100	156
ZIF-8	2.5% CQDs <sup>f</sup>	1356→1479	NO	0.42	10	30	0→43	157
[Cu <sub>2</sub> Br(ptz)] <sub>n</sub>	20% FCF	NA	RhB	4.8	0.25	180	3→88	158

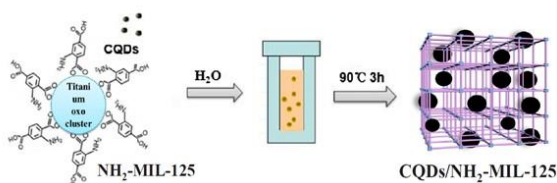
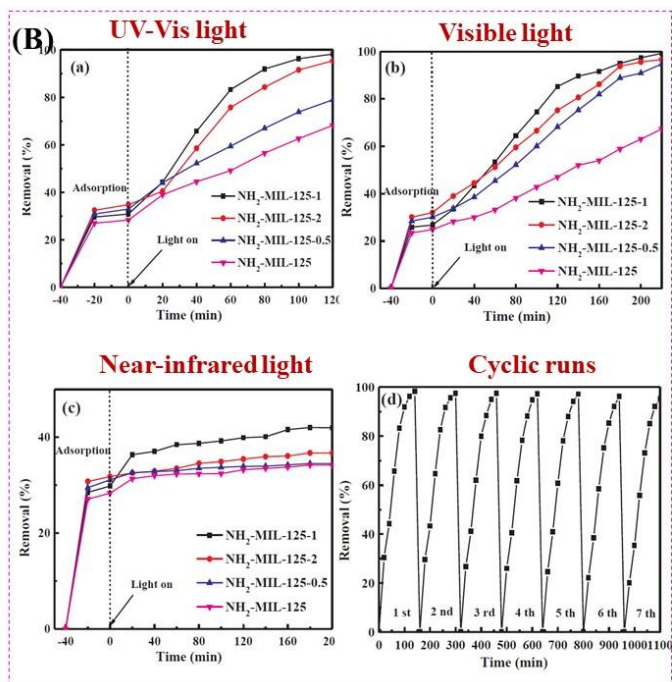
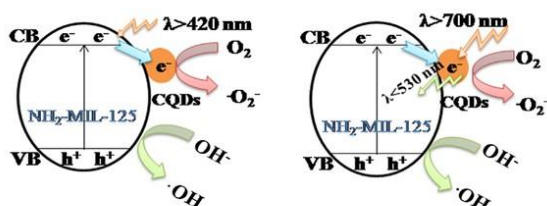
NA: no experimental data available; rGO: reduced graphene oxide; GO: graphene oxide; CQDs: carbon nanodots; FCF: functional carbon fiber; ptz: 5-(4-pyridyl)-1H-tetrazole; <sup>a</sup> S<sub>BET</sub> variation indicates the surface area of MOFs before and after loading carbon materials; <sup>b</sup> Removal efficiencies (η) for pollutants were used received or estimated from the figures in reference and presented in integer numbers, η variation indicated the performance of MOFs before and after loading carbon materials; <sup>c</sup> Addition of ammonium oxalate; <sup>d</sup> Addition of H<sub>2</sub>O<sub>2</sub>; <sup>e</sup> UV-Vis light or sunlight; <sup>f</sup> vol%.

For example, MIL-53(Fe)/rGO hybrid materials were prepared via simple one-step solvothermal method. With optimal loading amount of rGO (2.5 wt%), the degradation of MB dye can be promoted.<sup>149</sup> Besides, Li et al. reported the fabrication of GO modified NH<sub>2</sub>-MIL-125(Ti) with enhanced performance for photocatalytic degradation of gaseous pollutants. The light absorption, charge generating and transfer properties in NH<sub>2</sub>-MIL-125(Ti) can be greatly altered after GO coupling. For example, the light absorption was greatly enhanced in the region of 200-500 nm, and the absorption edge was also shifted from 445 to 455 nm due to strong interaction between GO and NH<sub>2</sub>-MIL-125(Ti). Moreover, the charge transfer resistance was also decreased (Fig. 22A), and the photocurrent response under visible light was dramatically promoted (Fig. 22B). Due to the above combined effects, photocatalytic oxidation of NO and degradation of acetaldehyde were both greatly accelerated on optimized GO/NH<sub>2</sub>-MIL-125(Ti) relative to pristine NH<sub>2</sub>-MIL-125(Ti) (Fig. 22C-D).

For better understanding, the proposed mechanism was depicted in Fig. 22E. Namely, upon visible light irradiation, the organic linker (2-aminoterephthalic acid) can be excited and generate electrons which will be transferred to the center of Ti-O cluster. In this way, the photoexcited electrons will be trapped on metallic Ti by reducing  $\text{Ti}^{4+}$  to  $\text{Ti}^{3+}$ . The presence of GO can rapidly accumulate the trapped electrons and accelerate their transfer to  $\text{O}_2$ . Thus, more reactive  $\text{O}_2^{\cdot-}$  radicals can be generated, which will be beneficial for the degradation of gaseous pollutants.



**Fig. 22.** Comparison of  $\text{NH}_2\text{-MIL-125(Ti)}$  and  $\text{GO/NH}_2\text{-MIL-125(Ti)}$ : (A) EIS Nyquist plots and (B) Photo-current responses; (C) Photocatalytic oxidation of NO; (D) Photocatalytic degradation of acetaldehyde; (E) Proposed mechanism for pollutants degradation by  $\text{GO/NH}_2\text{-MIL-125(Ti)}$  under visible light irradiation. Adapted with permission from ref. <sup>154</sup>, © 2018 Elsevier B.V.

**(A) Preparing process****(C) Proposed mechanism**

**Fig. 23.** (A) Schematic processes for preparing CQDs/NH<sub>2</sub>-MIL-125(Ti); (B) Photocatalytic degradation of RhB by NH<sub>2</sub>-MIL-125 and CQDs/NH<sub>2</sub>-MIL-125 composites under the irradiation of (a) full spectrum; (b) visible light and (c) near-infrared light; (d) cyclic runs for RhB degradation by optimized CQDs/NH<sub>2</sub>-MIL-125 under full spectrum light; (C) Proposed mechanism for charge transfer in CQDs/NH<sub>2</sub>-MIL-125(Ti) under visible light ( $\lambda > 420$  nm) and near-infrared light ( $\lambda > 700$  nm) irradiation; Adapted with permission from ref. <sup>155</sup>, © 2018 Elsevier B.V.

As novel carbon nanomaterial, CQDs were also applied to couple with MOFs. In addition to the beneficial properties of good electron conductivity, easy functionalization, low cost and low toxicity, CQDs has special optical property in upconversion luminescence.<sup>159-161</sup> The incident near infrared light can be absorbed by CQDs and then converted to visible light which will enhance the utilization of solar energy<sup>162</sup> As shown in Fig. 23A, CQDs with size of 2 nm were successfully distributed on NH<sub>2</sub>-MIL-125(Ti) via simple solvent-deposition method.<sup>163</sup> The large surface area of NH<sub>2</sub>-MIL-125(Ti) (487 m<sup>2</sup>/g) was beneficial for CQDs loading. For the photocatalytic degradation of RhB dye (Fig. 23B), the as-prepared CQDs/NH<sub>2</sub>-MIL-125 composite always exhibited enhanced performance, no matter the incident light is full spectrum, visible light or near-infrared light. Highest activity was observed at a loading amount of 1 wt% CQDs. Meanwhile, good stability of the optimized CQDs/NH<sub>2</sub>-MIL-125 can be maintained after 7 successive cyclic runs. For better understanding of the photocatalytic mechanism, photoluminescence (PL) spectra and Electrochemical impedance spectroscopy (EIS) Nyquist plots were measured to investigate the

separation efficiency and transfer resistance of photogenerated charge carriers, respectively. Moreover, the upconversion PL spectra were also carried out to detect the unique PL upconversion performance of CQDs. Based on the above results, the mechanism for charge generation, separation and transfer on CQDs/NH<sub>2</sub>-MIL-125(Ti) were proposed (Fig. 23C). Under visible light ( $\lambda > 420$  nm) irradiation, the good electron conductivity of CQDs can facilitate efficient separation of photogenerated  $e^-h^+$  pairs in NH<sub>2</sub>-MIL-125(Ti). Under near-infrared light ( $\lambda > 700$  nm) irradiation, in addition to electron conductivity, the special upconversion luminescence property of CQDs can convert near infrared light into visible light, leading to more efficient utilization of solar energy.

As another attractive option, functional carbon fiber (FCF) has several merits, such as high conductivity, large surface area and excellent absorption capability. Especially, FCF can act as a photosensitizer to extend the photoresponse. For example, a new coordination polymer [Cu<sub>2</sub>Br(ptz)]<sub>n</sub> (CP) (ptz=5-(4-pyridyl)-1H-tetrazole) nanobelts (CPNB) were loaded on the surface of FCF via a simple colloidal blending process.<sup>158</sup> The resulting CPNB/FCF composite exhibited significantly enhanced activity for photocatalytic degradation of RhB. At catalyst dosage of 0.25 g/L and after 180 min visible light irradiation, the removal efficiency for RhB dramatically increased from 3% by pristine CPNB to 88% by CPNB/FCF composite. As shown in Fig. 24A, the band gap ( $E_g$ ) of pristine CPNB was 3.17 eV, and it decreased to 2.02-2.69 eV after loading FCF with different pretreatment time. Moreover, results from photocurrent response and EIS Nyquist plots both indicated the merits of loading FCF (Fig. 24B-C). Considering the flat band potential in Mott-Schottky plot (Fig. 24C) and the  $E_g$  (3.17 eV), the CB and VB position of CPNB were estimated to be -0.31 V and +2.86 V (vs SCE), respectively. Under visible light irradiation, only FCF can be excited (Fig. 24D). The photogenerated electrons will transfer from the CB of FCF to CPNB, leading to effective separation of  $e^-h^+$  pairs.

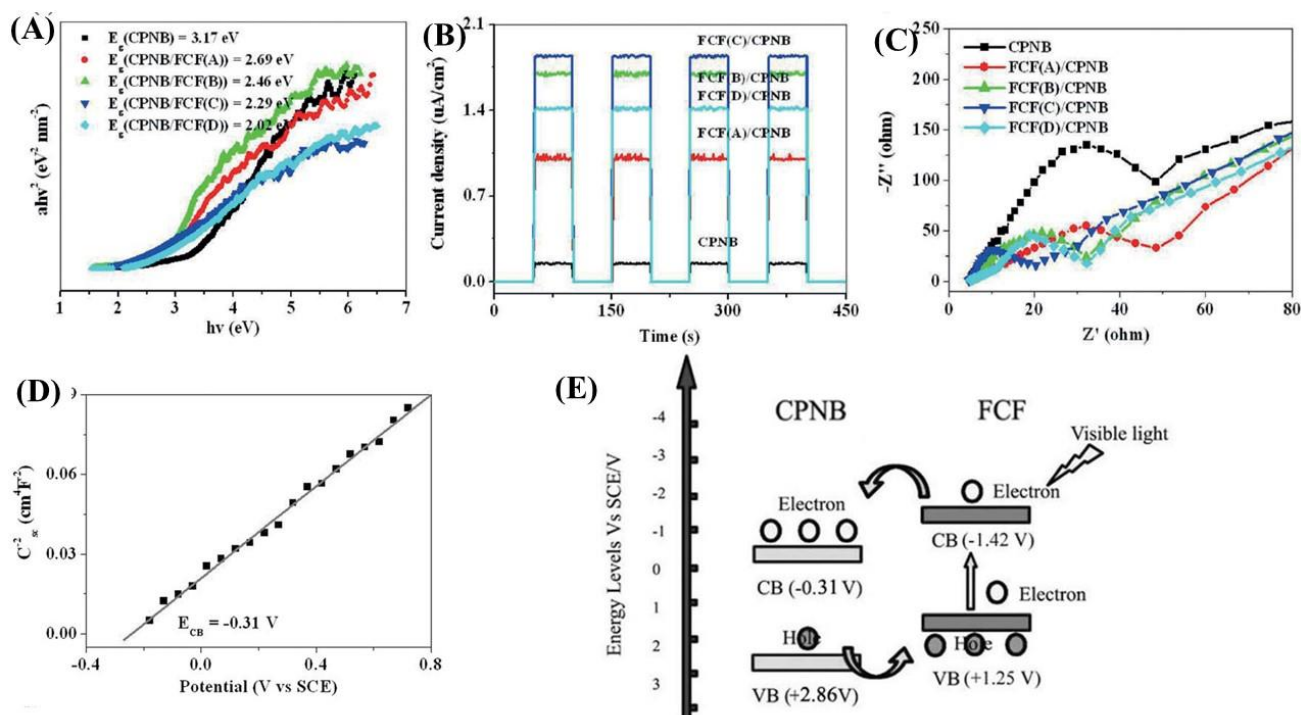


**Fig. 24.** Comparison between CPNB and CPNB/FCF: (A) Tauc plots; (B) Photocurrent response and (C) EIS Nyquist plots; (D) Mott–Schottky plot of CPNB; (E) Proposed photocatalytic mechanism for CPNB/FCF. Adapted with permission from ref. <sup>158</sup>, © 2015Wiley-VCH.

### 3.7 MOFs-semiconductor heterojunctions

Coupling MOFs with other photoactive semiconductors was another alternative way to enhance photocatalytic activity. In this approach, the porous network of MOFs can facilitate the dispersion of semiconductors, generating more active sites. Moreover, due to the formation of heterojunctions,<sup>164</sup> more efficient separation of photo-excited charges can be achieved. Typically, there are three types of heterojunctions for semiconductors, depending on the CB/VB position as well as n/p type nature of independent components (Fig. 25). Till now, many semiconductors have been reported to form composites with MOFs. For example, metal-containing semiconductors (such as ZnO, TiO<sub>2</sub>, BiVO<sub>4</sub>, AgI, α-Fe<sub>2</sub>O<sub>3</sub>, CdS, and etc.) and nonmetal graphitic carbon nitride (g-C<sub>3</sub>N<sub>4</sub>), have been coupled with photoactive MOFs and exhibited superior performance in field of photocatalysis.

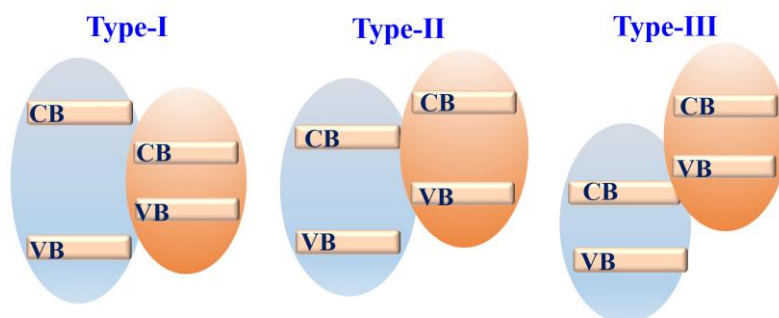


**Fig. 25.** Three types of semiconductor heterojunctions. Type-I: straddling gap; Type-II: staggered gap; Type-III: broken gap.

### 3.7.1 Coupling with metal-containing semiconductors

Since the first report of  $\text{TiO}_2$  photocatalysis in 1972, more and more semiconductor photocatalysts were synthesized and reported. Some semiconductors can be directly excited by visible light, such as  $\text{BiOBr}$ ,  $\text{BiOI}$ ,  $\text{MoO}_3$ ,  $\text{WO}_3$ ,  $\text{Bi}_2\text{MoO}_6$ ,  $\text{BiVO}_4$ ,  $\text{AgI}$ ,  $\text{Ag}_3\text{PO}_4$ , and etc. As for the construction of MOFs-based heterojunctions, such metal-containing semiconductors were gradually tested. The as-prepared MOFs-based binary composites for photocatalytic removal of environmental pollutants were summarized in Table 5. Except for MIL-53(Fe) with 1D lozenge-shaped channels and ultra-small surface area ( $< 100 \text{ m}^2/\text{g}$ ),<sup>165-167</sup> the coupling of other MOFs with a photoactive semiconductor led to decreased surface area relative to pristine MOFs. Due to comprehensive effects of various factors, including light absorption, charge generation, separation and transfer properties, the photocatalytic performance for environmental remediation can be promoted.

**Table 5** MOFs-based binary composites for photocatalytic removal of environmental pollutants.

Composites	<sup>a</sup> $S_{\text{BET}}$ Variation ( $\text{m}^2/\text{g}$ )	Pollutant	$C_{\text{pollutant}}$ ( $\text{mg}/\text{L}$ )	$C_{\text{catalyst}}$ ( $\text{g}/\text{L}$ )	Time (min)	<sup>b</sup> $\eta$ Variation (%)	Ref.
<b><u>Coupled with Zn-MOFs</u></b>							
$\text{BiOBr}/\text{MOF-5(IL)}$	915 $\rightarrow$ NA	MO	10	0.4	150	$<2\rightarrow 88$	168
$\text{TiO}_2@\text{ZIF-8}$	NA	MB	1.6	NA	120	54 $\rightarrow 88^d$	169
		RhB	2.4	NA	120	50 $\rightarrow 65^d$	
$\text{Bi}_2\text{MoO}_6/\text{ZIF-8}$	NA	MB	20	0.25	100	34 $\rightarrow 67$	170
3D $\text{MoO}_3@\text{ZIF-8}$	1531 $\rightarrow$ 213	Cr(VI)	15	0.5	40	13 $\rightarrow 96$	171
$\text{MoO}_3\text{-NPs}/\text{ZIF-8}$	1710 $\rightarrow$ 1529	MB	10	0.25	180	59 $\rightarrow 82^d$	172
$\text{BiFeO}_3/\text{ZIF-8}$	NA	MB	20	0.375	100	50 $\rightarrow 93$	173

ZIF-8@BiVO <sub>4</sub>	1180→249	MB	20	0.25	130	NA→81 <sup>d</sup>	174
Bi <sub>2</sub> S <sub>3</sub> @ZIF-8	1297→821	RhB	10	0.4	90	NA→97	175
Cd <sub>0.5</sub> Zn <sub>0.5</sub> S@ZIF-8	1190→174	Cr(VI)	20	1	10	5→100	176
<b><u>Coupled with Fe-MOFs</u></b>							
Fe <sub>2</sub> O <sub>3</sub> /MIL-53(Fe)	48→47	MB	10	0.2	120	31→48	177
WO <sub>3</sub> /MIL-53(Fe)	57→97	Cr(VI)	30	1.5	240	70→94 <sup>d</sup>	167
		2,4-D	30	1.5	240	58→100 <sup>d</sup>	
Ag <sub>3</sub> PO <sub>4</sub> /MIL-53(Fe)	9→16	TC	20	0.5	60	26→94	165
AgI/MIL-53(Fe)	NA	RhB	4.8	0.3	45	86→99	166
CdS/MIL-53(Fe)	NA	RhB	10	1.0	120	5→86	178
1T-MoS <sub>2</sub> /MIL-53(Fe)	21→337	IBP <sup>c</sup>	10	0.4	120	50→100	179
MIL-53(Fe)/SnS	56→34	Cr(VI)	20	1.0	60	16→71	180
TiO <sub>2</sub> @NH <sub>2</sub> -MIL-88B(Fe)	34→19	Cr(VI) <sup>e</sup>	10.4	0.5	35	85→99 <sup>d</sup>	181
TiO <sub>2</sub> NS@MIL-100(Fe)	1670→474	MB <sup>c</sup>	50	0.2	60	NA→96	182
MIL-100(Fe)/TiO <sub>2</sub>	1189→307	TC <sup>c</sup>	100	0.05	60	NA→86 <sup>d</sup>	183
		Cr(VI)	10	0.05	60	NA→50 <sup>d</sup>	
N-TiO <sub>2</sub> QDs/MIL-100(Fe)	1556→1413	MB	16	0.1	140	90→99	184
		RhB	24	0.1	140	83→94	
M.MIL-100(Fe)@ZnO	766→654	Phenol	5	0.2	120	43→85	185
		BPA	5	0.2	120	35→89	
		Atrazine	5	0.2	120	30→70	
Bi <sub>2</sub> WO <sub>6</sub> /MIL-100(Fe)	1370→140	SA <sup>c</sup>	10	1.0	50	35→95	186
Bi <sub>2</sub> MoO <sub>6</sub> /MIL-100(Fe)	NA→110	RhB	10	1.0	120	51→88	187
MIL-100(Fe)@Bi <sub>2</sub> S <sub>3</sub>	1394→404	RhB	10	0.5	60	70→94	188
M-MIL-101(Fe)/TiO <sub>2</sub>	394→159	TC	20	1.0	80	74→92	189
<b><u>Coupled with Cr-MOFs</u></b>							
N-K <sub>2</sub> Ti <sub>4</sub> O <sub>9</sub> /MIL-101(Cr)	2321→135	RhB	5	0.2	180	43→54 <sup>d</sup>	190
WO <sub>3</sub> @MIL-101(Cr)@WO <sub>3</sub>	2480→1360	MB	30	NA	80	NA→100	191
<b><u>Coupled with Zr-MOFs</u></b>							
Ag <sub>2</sub> CO <sub>3</sub> /UiO-66(Zr)	808→522	RhB	14.4	0.5	120	NA→94	192
AgI/UiO-66(Zr)	808→289	RhB	14.4	0.5	60	NA→100	193
N-K <sub>2</sub> Ti <sub>4</sub> O <sub>9</sub> /NH <sub>2</sub> -UiO-66(Zr)	NA	RhB	5	0.2	180	53→90 <sup>d</sup>	194
		MB	5	0.2	180	NA→94 <sup>d</sup>	
		NR	5	0.2	180	NA→91 <sup>d</sup>	
BiOBr/UiO-66(Zr)	869→204	RhB	14.4	0.5	15	<5→98	195
BiOBr/NH <sub>2</sub> -UiO-66(Zr)	NA	Noroxin	0.3	0.3	180	34→94 <sup>d</sup>	196



$\alpha$ -Fe <sub>2</sub> O <sub>3</sub> @UiO-66(Zr)	1296→1204	MB	12.8	1.0	50	70→100	197
WO <sub>2.72</sub> /UiO-66(Zr)	1099→187	MO	20	0.3	60	48→100	198
BiVO <sub>4</sub> /UiO-66(Zr)	646→387	RhB	10	1.0	150	<10→100	199
Bi <sub>2</sub> WO <sub>6</sub> /UiO-66(Zr)	808→275	RhB	14.4	0.5	180	NA→100	200
Bi <sub>2</sub> MoO <sub>6</sub> /UiO-66(Zr)	621→209	RhB	10	0.5	120	30→92	201
ZnIn <sub>2</sub> S <sub>4</sub> /UiO-66(Zr)	911→242	Cr(VI)	80	0.5	60	<5→99	202
		MO	20	0.17	180	49→98	
CdS@NH <sub>2</sub> -UiO-66(Zr)	840→114	MG	20	0.2	30	16→100	203
<b><u>Coupled with Ti-MOFs</u></b>							
In <sub>2</sub> S <sub>3</sub> @MIL-125(Ti)	1548→304	TC	46	0.3	60	42→63	204
BiOBr/NH <sub>2</sub> -MIL-125(Ti)	1012→8	RhB	20	0.2	100	41→98	205
		Phenol	20	0.2	150	NA→24	
BiOI/NH <sub>2</sub> -MIL-125(Ti)	NA	MO	20	1.0	120	22→93	206
NH <sub>2</sub> -MIL-125(Ti)/BiOCl	770→46	TC	20	0.5	120	5→78	207
		BPA	10	0.5	240	NA→65	
Ag <sub>3</sub> PO <sub>4</sub> /NH <sub>2</sub> -MIL-125(Ti)	NA	MB	10	0.5	50	55→100	208
		RhB	10	0.5	180	50→94	
PHIK/NH <sub>2</sub> -MIL-125(Ti)	1160→185	RhB	100	1.0	120	66→97 <sup>h</sup>	209
CdTe QDs/NTU-9	1205→880	Rh6G	1.0	0.05	30	55→96 <sup>f</sup>	210
<b><u>Coupled with Cu-MOFs</u></b>							
HKUST-1/BiVO <sub>4</sub>	855→585	DB17	30	0.2	20	NA→100 <sup>g</sup>	211
		RB	30	0.2	20	NA→99 <sup>g</sup>	
Cu <sub>2</sub> (OH)PO <sub>4</sub> -HKUST-1	NA	Abamectin	30	0.4	20	NA→100 <sup>g</sup>	212
<b><u>Coupled with other MOFs</u></b>							
Co <sub>2</sub> Ni-MOF/BiFeO <sub>3</sub>	1058→895	MO	50	0.2	90	34→94	213
		4-NP	50	0.2	90	24→75	
Co <sub>2</sub> Ni-MOF/CuWO <sub>4</sub>	1054→801	MB	10	0.2	135	32→98	214
		4-NP	10	0.2	105	24→81	
Ag <sub>3</sub> PO <sub>4</sub> @Co <sub>2</sub> Ni-MOF	NA	Phenol	40	1.0	16	<5→100	215
		BPA	40	1.0	20	<5→99	
BiOBr/CAU-17	NA	RhB	20	0.2	40	22→99	216

NA: no experimental data available; <sup>a</sup> S<sub>BET</sub> variation indicates the surface area of MOFs before and after forming composite; <sup>b</sup> Removal efficiencies ( $\eta$ ) for pollutants were used received or estimated from the figures in reference and presented in integer numbers,  $\eta$  variation indicated the performance of MOFs before and after forming composite; <sup>c</sup> Addition of H<sub>2</sub>O<sub>2</sub>; <sup>d</sup> UV-Vis light or simulated sunlight; <sup>e</sup> addition of ammonium oxalate; <sup>f</sup> 500 nm monochromatic light; <sup>g</sup> under the assistance of sonication; <sup>h</sup> 465 nm LED light.

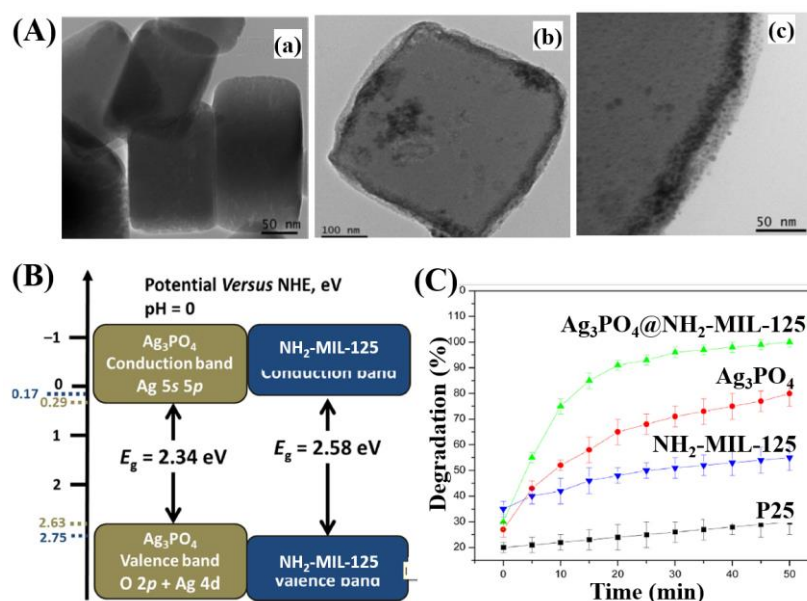


**Fig. 26.** (A) TEM images of NH<sub>2</sub>-MIL-125(Ti) (a), Ag<sub>3</sub>PO<sub>4</sub>@NH<sub>2</sub>-MIL-125(Ti) (b), and high magnification of Ag<sub>3</sub>PO<sub>4</sub>@NH<sub>2</sub>-MIL-125(Ti) (c); (B) CB and VB positions of Ag<sub>3</sub>PO<sub>4</sub> and NH<sub>2</sub>-MIL-125 (Ti); (C) Photocatalytic degradation of MB by different samples under visible light irradiation. Adapted with permission from ref. <sup>208</sup>, © 2017 Elsevier B.V.

For example, Ag<sub>3</sub>PO<sub>4</sub>@NH<sub>2</sub>-MIL-125(Ti) were fabricated *via* a simple dry-process.<sup>208</sup> As shown in Fig. 26A, Ag<sub>3</sub>PO<sub>4</sub> nanoparticles (10 to 20 nm) were well-dispersed onto the surface of NH<sub>2</sub>-MIL-125(Ti). The band structure of Ag<sub>3</sub>PO<sub>4</sub> and NH<sub>2</sub>-MIL-125(Ti) were illustrated in Fig. 26B, which indicated Type I heterojunction. The as-prepared binary composite exhibited significantly enhanced performance (Fig. 26C) as well as good stability for MB degradation under visible light irradiation. Similarly, WO<sub>2.72</sub>/UiO-66(Zr)<sup>198</sup> and Co,Ni-MOF/BiFeO<sub>3</sub><sup>213</sup> composites were also prepared and displayed characteristic properties of Type I heterojunctions.

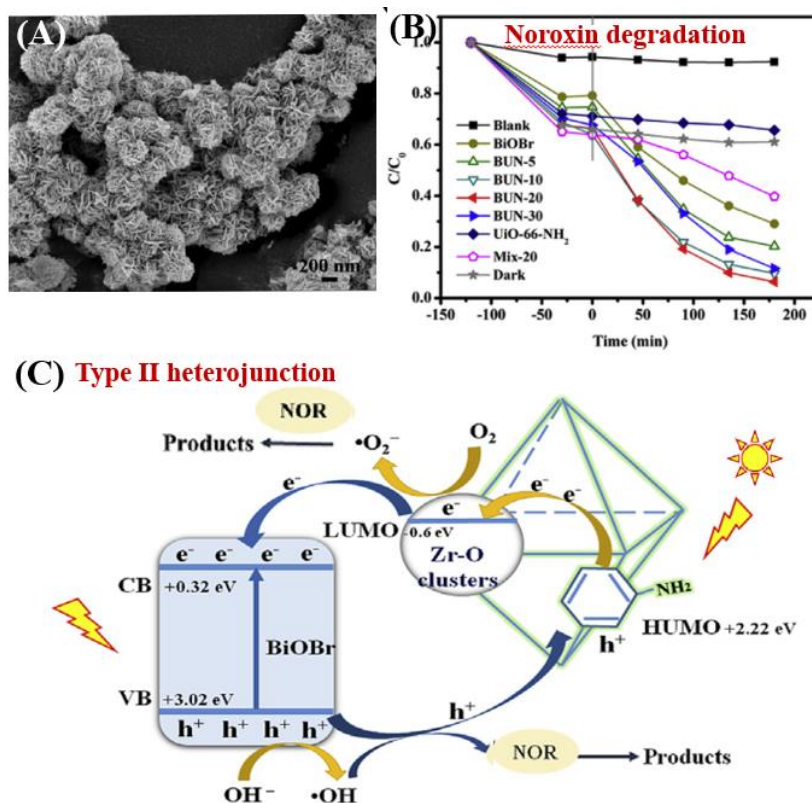


**Fig. 27.** (A) SEM image of BiOBr/NH<sub>2</sub>-UiO-66(Zr); (B) Photocatalytic degradation of Noroxin by different samples under simulated sunlight irradiation; (C) Proposed mechanism for photocatalytic degradation of Noroxin by BiOBr/NH<sub>2</sub>-UiO-66(Zr). Adapted with permission from ref. <sup>196</sup>, © 2018 Elsevier Ltd.

Due to water-stability of UiO-66(Zr), the development of UiO-66(Zr)-based composites were competitive candidates for wastewater treatment. For example, BiOBr/UiO-66(Zr) was prepared by incorporating UV-active UiO-66 ( $E_g = 4.0$  eV) with visible light-active BiOBr ( $E_g = 2.8$  eV) through a convenient solution method.<sup>195</sup> The as-prepared BiOBr/UiO-66 composite displayed enhanced photocatalytic activity for RhB degradation, as well as good stability in cyclic runs. After 15 min visible light irradiation, the removal efficiency of RhB was in the order of BiOBr/UiO-66 (100%) > BiOBr (84%) > UiO-66(Zr) (<5%). Furthermore, amine-functionalized UiO-66 was also applied to couple with BiOBr.<sup>196</sup> As shown in Fig. 27A, flower-like BiOBr/NH<sub>2</sub>-UiO-66(Zr) composite with three-dimensional structure were fabricated. Intensive characterizations, such as SEM, XRD and XPS, have been carried out to investigate the structure properties. Results indicated that BiOBr nanoplates successfully grew on the surface of NH<sub>2</sub>-UiO-66(Zr) with an intimate interaction. The recombination of charge carriers can be inhibited, which was evidenced by PL spectra. For the photocatalytic degradation of a typical fluoroquinolones antibiotics (Norfloxacin), the as-prepared

BiOBr/NH<sub>2</sub>-UiO-66(Zr) composites with different loading amounts all displayed enhanced performance (Fig. 27B). Highest activity was achieved by BUN-20 with 20 wt% NH<sub>2</sub>-UiO-66. Furthermore, trapping experiments were also performed to reveal the active species for Norfloxacin degradation. The addition of electron scavenger (HCOOH) and emptying oxygen (N<sub>2</sub> purging) both significantly inhibited the degradation dynamics. Thus, the dominant role of O<sub>2</sub><sup>•-</sup> can be speculated since O<sub>2</sub><sup>•-</sup> was originated from the electron transfer to O<sub>2</sub>. Besides, the secondary role of HO<sup>•</sup> and h<sup>+</sup> can also be confirmed via addition of corresponding IPA and NaCl scavengers. Considering the band positions of independent BiOBr and NH<sub>2</sub>-UiO-66(Zr), a Type II heterojunction<sup>167, 196, 207</sup> can be applied to explain the charge transfer processes (Fig. 27C). It is thermodynamically feasible that the photogenerated electrons in the LUMO of NH<sub>2</sub>-UiO-66(Zr) (-0.6 eV) can be transferred to the CB of BiOBr (+0.32 eV). Meanwhile, holes (h<sup>+</sup>) in the VB of BiOBr (+3.02 eV) can be transferred to the HUMO of NH<sub>2</sub>-UiO-66(Zr) (+2.22 eV). Moreover, the LUMO of NH<sub>2</sub>-UiO-66(Zr) and VB of BiOBr are energetic enough for reducing O<sub>2</sub> to O<sub>2</sub><sup>•-</sup> and oxidizing HO<sup>-</sup> to HO<sup>•</sup>, respectively. The synergistic effect between BiOBr and NH<sub>2</sub>-UiO-66(Zr) led to highly enhanced performance for Norfloxacin degradation.

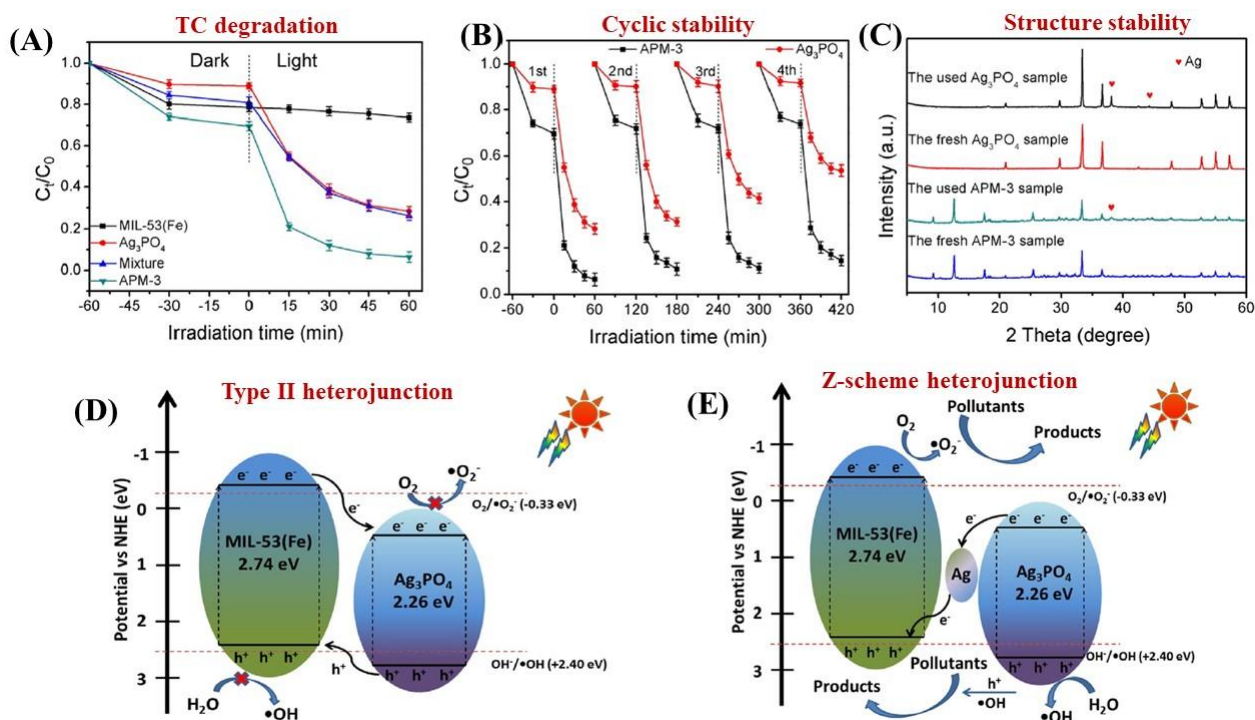


**Fig. 28.** (A) Photocatalytic degradation of TC by different samples under visible light irradiation; (B) Cyclic stability of Ag<sub>3</sub>PO<sub>4</sub> and Ag<sub>3</sub>PO<sub>4</sub>/MIL-53(Fe) composite for photocatalytic degradation of TC; (C) XRD patterns of

$\text{Ag}_3\text{PO}_4$  and  $\text{Ag}_3\text{PO}_4/\text{MIL-53(Fe)}$  in different conditions; Proposed mechanism for charge separation over  $\text{Ag}_3\text{PO}_4/\text{MIL-53(Fe)}$ : (D) Traditional Type II heterojunction and (E) Z-scheme heterojunction. Adapted with permission from ref. <sup>165</sup>, © 2018 Elsevier B.V.

In addition to traditional Type II heterojunction, novel MOF-based Z-scheme heterojunction were recently reported.<sup>165, 167</sup> For example,  $\text{Ag}_3\text{PO}_4/\text{MIL-53(Fe)}$  composite was prepared through a simple in situ precipitation strategy. The as-prepared binary composite displayed enhanced photocatalytic performance for the degradation of multiple antibiotics such as tetracycline (TC), oxytetracycline (OTC), chlortetracycline (CTC) and deoxytetracycline (DCL). As shown in Fig. 28A, the optimized  $\text{Ag}_3\text{PO}_4/\text{MIL-53(Fe)}$  composite (APM-3) with 1:3 mass ratio exhibited highest activity for TC degradation. More importantly, the binary composite also displayed higher photostability and recyclability than pristine  $\text{Ag}_3\text{PO}_4$  (Fig. 28B). After four cyclic runs for TC degradation, the loss of degradation efficiency using APM-3 was ca. 8%. Whereas, the value was ca. 25% using  $\text{Ag}_3\text{PO}_4$ . The instability of  $\text{Ag}_3\text{PO}_4$  during the photocatalytic process was evidenced by the formation of metallic Ag. More obvious XRD signals of Ag (JCPDS card no. 65-2871) were observed in pristine  $\text{Ag}_3\text{PO}_4$  relative to APM-3 (Fig. 28C). Interestingly, the formation of tiny metallic Ag may lead to a Z-scheme structure for charge transfer in  $\text{Ag}_3\text{PO}_4/\text{MIL-53(Fe)}$  composite. As shown in Fig. 28D, the CB/LUMO positions of  $\text{Ag}_3\text{PO}_4$  and MIL-53(Fe) matched well with typical Type II heterojunctions. In this mechanism, the electrons in the LUMO of MIL-53(Fe) (-0.41 eV) will flow into the CB of  $\text{Ag}_3\text{PO}_4$  (+0.42 eV). Since the CB edge of  $\text{Ag}_3\text{PO}_4$  is more positive than the redox potential of  $\text{O}_2/\text{O}_2^{\bullet-}$  (-0.33 eV vs NHE), the formation of  $\text{O}_2^{\bullet-}$  was not feasible. Similarly, the HOMO position of MIL-53(Fe) (+2.33 eV) was not energetic enough to oxidize surface  $\text{HO}^-$  into  $\text{HO}^{\bullet}$  ( $E_{\text{HO}^-/\text{HO}^{\bullet}} = +2.40$  eV vs NHE). However, both strong signals of  $\text{HO}^{\bullet}$  and  $\text{O}_2^{\bullet-}$  were detected by electron spin resonance (ESR) spectroscopy. Thus, Type II heterojunction mechanism was not suitable for  $\text{Ag}_3\text{PO}_4/\text{MIL-53(Fe)}$ . Since metallic Ag was detected during the photocatalytic process, a Z-scheme mechanism can well explain the above phenomena. As depicted in Fig. 28E, metallic Ag nanoparticles with proper Fermi level can act as bridge for electron transfer from the CB of  $\text{Ag}_3\text{PO}_4$  to the HOMO of MIL-53(Fe). In this way, both the high reductive ability of MIL-53(Fe) and oxidative ability of  $\text{Ag}_3\text{PO}_4$  can be well maintained, leading to generation of sufficient active species ( $\text{HO}^{\bullet}$  and  $\text{O}_2^{\bullet-}$ ).

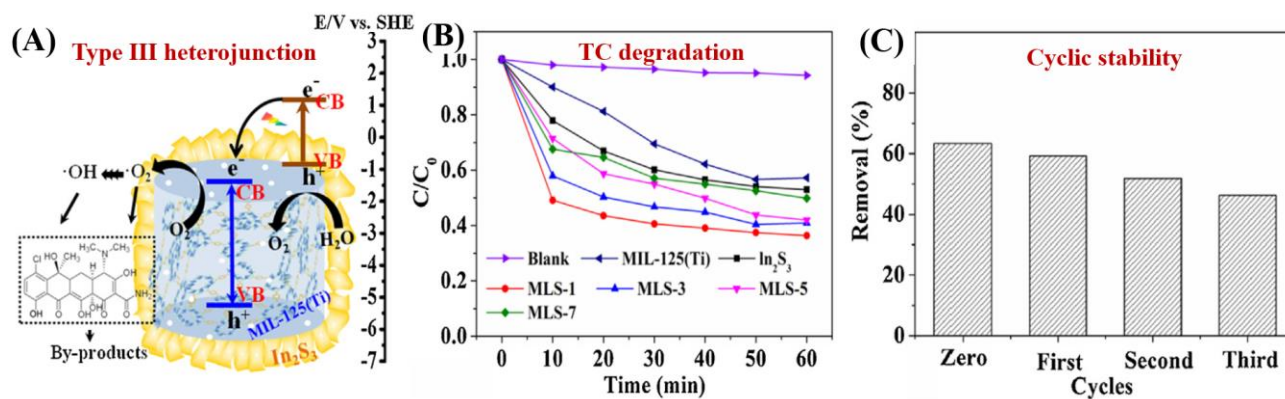


**Fig. 29.** (A) Proposed mechanism for the charge transfer processes in In<sub>2</sub>S<sub>3</sub>@MIL-125(Ti); (B) Photocatalytic degradation of TC by different samples; (C) Cyclic stability of optimized In<sub>2</sub>S<sub>3</sub>@MIL-125(Ti) for TC degradation under visible light. Adapted with permission from ref. <sup>204</sup>, © 2016 Elsevier.

Comparing with Type I and Type II heterojunctions, there were very few reports of Type III heterojunctions for environmental photocatalysis. In 2016, Wang et al. reported the fabrication of core-shell In<sub>2</sub>S<sub>3</sub>@MIL-125(Ti) *via* solvothermal method.<sup>204</sup> As shown in Fig. 29A, the band positions of In<sub>2</sub>S<sub>3</sub> and MIL-125(Ti) matched well with Type III heterojunction. Upon visible light irradiation, the photogenerated electrons in the CB of In<sub>2</sub>S<sub>3</sub> will be transferred to the LUMO of MIL-125(Ti), which finally led to reduction of adsorbed O<sub>2</sub>. Meanwhile, the corresponding h<sup>+</sup> left in the VB of In<sub>2</sub>S<sub>3</sub> will oxidize water into O<sub>2</sub>. Thus, promoted separation of photogenerated charges can be achieved, which finally led to enhanced degradation of TC (Fig. 29B). However, probably due to low oxidizing ability of h<sup>+</sup> in In<sub>2</sub>S<sub>3</sub>, the degradation of TC on optimized In<sub>2</sub>S<sub>3</sub>@MIL-125(Ti) slow down with prolonged irradiation time. Besides, the cyclic stability for TC degradation exhibited moderate loss (Fig. 29C).

### 3.7.2 Coupling with metal free g-C<sub>3</sub>N<sub>4</sub> semiconductor

Nonmetal g-C<sub>3</sub>N<sub>4</sub> was a star photocatalyst due to its appealing electronic structure, low cost and high stability. The band gap of g-C<sub>3</sub>N<sub>4</sub> was ca. 2.7 eV, indicating the light absorption edge into visible region (up to 450 nm). Thus, coupling g-C<sub>3</sub>N<sub>4</sub> with MOFs may lead to enhanced visible light response. As summarized in Table 6, many kinds of MOFs-C<sub>3</sub>N<sub>4</sub> binary composites have been fabricated and displayed superior photocatalytic activity. After coupling with g-C<sub>3</sub>N<sub>4</sub>, the BET specific surface area was decreased to different extends in most cases, indicating less surface active sites. Despite of this, the negative effects by decreased surface area can be offset by enhanced visible

light absorption, promoted conductivity, more efficient charge separation and lower charge transfer resistance induced by g-C<sub>3</sub>N<sub>4</sub>.

**Table 6** MOFs-C<sub>3</sub>N<sub>4</sub> binary composites for photocatalytic removal of environmental pollutants.

MOFs	C <sub>3</sub> N <sub>4</sub> (wt%)	<sup>a</sup> S <sub>BET</sub> Variation (m <sup>2</sup> /g)	Pollutant	C <sub>pollutant</sub> (mg/L)	C <sub>catalyst</sub> (g/L)	Time (min)	<sup>b</sup> η Variation (%)	Ref.
<b><u>Coupled with Zn-MOFs</u></b>								
ZIF-8(Zn)	60%	1318→555	TC	89	0.1	60	45→91 <sup>c</sup>	217
ZIF-8(Zn)	97%	NA	TC	20	0.5	30	NA→74	218
			RhB	10	0.5	75	NA→99	
			MO	50	0.5	180	NA→86	
BUC-21(Zn)	50%	1→12	Cr(VI)	10	0.25	120	13→100	219
<b><u>Coupled with Al-MOFs</u></b>								
MIL-53(Al)	20%	NA→44	RhB	10	0.5	75	NA→100 <sup>c</sup>	220
<b><u>Coupled with Fe-MOFs</u></b>								
MIL-53(Fe)	3%	21→19	Cr(VI)	10	0.4	180	52→100	221
NH <sub>2</sub> -MIL-53(Fe)	50% <sup>e</sup>	NA	TC <sup>d</sup>	50	0.4	30	82→90	222
			CBZ <sup>d</sup>	50	0.4	150	52→78	
			BPA <sup>d</sup>	50	0.4	10	NA→100	
			PNP <sup>d</sup>	50	0.4	30	NA→100	
MIL-88A(Fe)	90%	22→38	RhB	10	1.0	30	<5→100	223
			Phenol	10	1.0	120	<5→26	
			TC	10	1.0	120	<5→46	
MIL-88A(Fe)	NA	24→16	MB	NA	1.0	120	25→75	224
NH <sub>2</sub> -MIL-88B(Fe)	10%	NA	MB <sup>d</sup>	30	1.0	120	57→100	225
MIL-100(Fe)	1% <sup>f</sup>	1225→1096	RhB <sup>d</sup>	50	0.2	240	68→100	226
MIL-100(Fe)	80%	NA	Cr(VI)	10	0.5	80	76→98 <sup>c</sup>	227
			DS <sup>d</sup>	32	0.5	30	NA→100 <sup>c</sup>	
MIL-100(Fe)	9% <sup>g</sup>	1556→1252	RhB	10	1	200	36→87	228
			MB	10	1	200	27→82	
			pyridine	560 <sup>h</sup>	5	360	53→76	
MIL-101(Fe)	2%	NA	BPA <sup>i</sup>	10	0.5	60	51→100	229
NH <sub>2</sub> -MIL-101(Fe)	NA	NA	Cr(VI)	10	0.5	60	56→100	230
<b><u>Coupled with Zr-MOFs</u></b>								
UiO-66(Zr)	50%	1335→1133	RhB	10	0.4	180	19→93	231

UiO-66(Zr)	50%	972→384	MB	10	0.25	240	48→100	232
PCN-222(Zr)	99%	NA→36	RhB	20	0.1	120	78→98	233
			Ofloxacin	20	0.1	200	72→96	
<b>Coupled with Ti-MOFs</b>								
MIL-125(Ti)	7%	1548→328	RhB	50	0.4	60	15→95	234
NH <sub>2</sub> -MIL-125(Ti)	30%	1535→830	4-NP	NA	NA	240	55→75	235
<b>Coupled with Cu-MOFs</b>								
HKUST-1	25% <sup>j</sup>	1084→392	DMCP	NA	NA	1440	NA	236
HKUST-1/fiber	25%	1084→392	DMCP	NA	NA	1440	NA	237

NA: no experimental data available; <sup>a</sup>  $S_{\text{BET}}$  variation indicates the surface area of MOFs before and after forming composite; <sup>b</sup> Removal efficiencies ( $\eta$ ) for pollutants were used received or estimated from the figures in reference and presented in integer numbers,  $\eta$  variation indicated the performance of MOFs before and after forming composite; <sup>c</sup> UV-Vis light or sunlight; <sup>d</sup> Addition of H<sub>2</sub>O<sub>2</sub>; <sup>e</sup> g-C<sub>3</sub>N<sub>4</sub> doped with pyromellitic diimide (PDI); <sup>f</sup> g-C<sub>3</sub>N<sub>4</sub> nanosheet; <sup>g</sup> Protonated g-C<sub>3</sub>N<sub>4</sub>; <sup>h</sup>  $\mu\text{g/g}$ ; <sup>i</sup> Addition of PS; <sup>j</sup> oxidized g-C<sub>3</sub>N<sub>4</sub>.

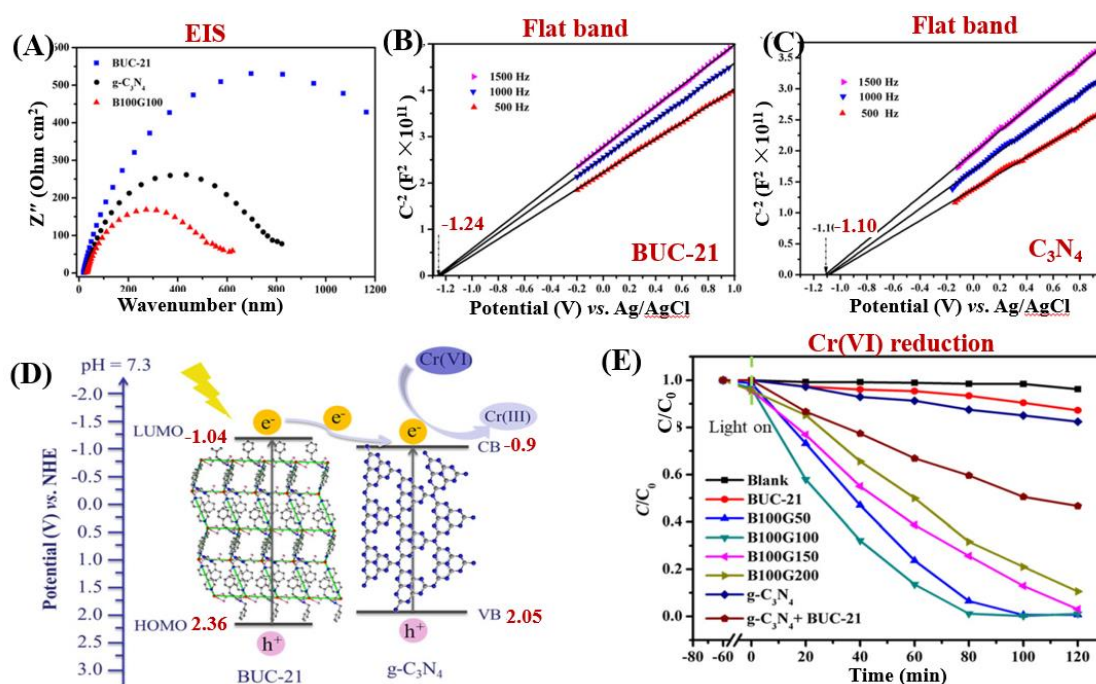


**Fig. 30.** (A) EIS Nyquist plots of different samples; (B) Mott–Schottky plots of BUC-21; (C) Mott–Schottky plots of g-C<sub>3</sub>N<sub>4</sub>; (D) Proposed mechanism for photogenerated electron transfer by BUC-21/g-C<sub>3</sub>N<sub>4</sub> heterojunction; (E) Photocatalytic reduction of Cr(VI) by different samples. Adapted with permission from ref. <sup>219</sup>, © 2018 John Wiley & Sons, Ltd.



For example, Wang's group reported the facile fabrication of Type-I heterojunction between a novel Zn-MOFs (BUC-21) and g-C<sub>3</sub>N<sub>4</sub> through ball-milling. The as-prepared BUC-21/g-C<sub>3</sub>N<sub>4</sub> composite displayed enhanced photocatalytic performance for Cr(VI) reduction. The radius of EIS Nyquist plot for BUC-21/g-C<sub>3</sub>N<sub>4</sub> composite was smaller than either BUC-21 or g-C<sub>3</sub>N<sub>4</sub> (Fig. 30A), indicating lowest electron transfer impedance. Thus, for the reduction of Cr(VI) under simulated sunlight, BUC-21/g-C<sub>3</sub>N<sub>4</sub> composites with different loading percentage of g-C<sub>3</sub>N<sub>4</sub> displayed significantly enhanced performance (Fig. 30E). After 120 min light irradiation, only 13% and 18% Cr(VI) can be reduced by single BUC-21 and g-C<sub>3</sub>N<sub>4</sub>, respectively. Whereas, 100% reduction efficiency can be achieved by BUC-21/g-C<sub>3</sub>N<sub>4</sub> (B100G100) composite with 50 wt% g-C<sub>3</sub>N<sub>4</sub>. In order to further confirm the formation of heterojunction, a mixture of BUC-21 and g-C<sub>3</sub>N<sub>4</sub> with the same content as optimized BUC-21/g-C<sub>3</sub>N<sub>4</sub> were also tested for Cr(VI) reduction. The value was ca. 52%, which was far less than the composite. For better understanding the interfacial charge transfer mechanism, the band positions of pristine BUC-21 and g-C<sub>3</sub>N<sub>4</sub> were estimated from typical Mott-Schottky measurements. As illustrated in Fig. 30B-C, the flat band potentials were ca -1.24 V and -1.10 V (*vs* Ag/AgCl) for BUC-21 and g-C<sub>3</sub>N<sub>4</sub>, corresponding to -1.04 V and -0.90 V (*vs* NHE), respectively. Besides, the positive slope of Mott-Schottky plot indicated n-type semiconductor. Therefore, the VB position can be calculated from the equation:  $E_g = E_{VB} - E_{CB}$ . As shown in Fig. 30D, a Type-I heterojunction can be deduced from BUC-21/g-C<sub>3</sub>N<sub>4</sub> composite. In addition to UV active BUC-21, Type-I heterojunctions can also be achieved when visible light-active Fe-MOFs were coupled with g-C<sub>3</sub>N<sub>4</sub>.<sup>224-226, 228</sup> For example, MIL-100(Fe) with tricarboxylate linker was reported to be very stable with relatively high BET surface area (> 1000 m<sup>2</sup>/g).<sup>5</sup> The LUMO and HOMO positions of MIL-100(Fe) were estimated to be -0.24 V and 1.73 V (*vs* Ag/AgCl) at pH 7, respectively.<sup>226</sup> The corresponding CB and VB values were -0.92 V and 1.96 V (*vs* Ag/AgCl) for g-C<sub>3</sub>N<sub>4</sub> nanosheets. The MIL-100(Fe)/g-C<sub>3</sub>N<sub>4</sub> composite with Type I heterojunction exhibited enhanced activity for RhB degradation. After 240 min visible light irradiation, the degradation efficiency increased from 68% on pristine MIL-100(Fe) to 100% on MIL-100(Fe)/g-C<sub>3</sub>N<sub>4</sub>.

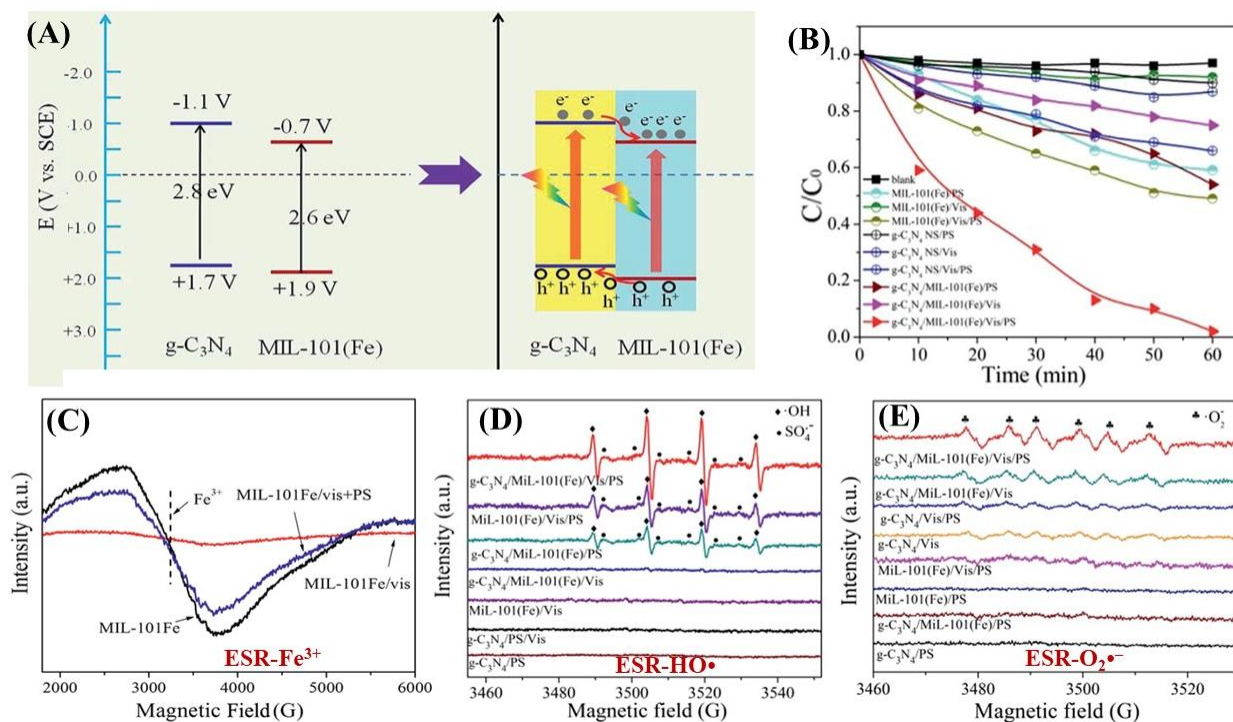


**Fig. 31.** (A) Schematic diagram of the band structure and charge transfer between MIL-101(Fe) and g-C<sub>3</sub>N<sub>4</sub>; (B) Visible light-induced photocatalytic degradation of BPA under different conditions; (C) ESR spectra of Fe<sup>3+</sup> in MIL-101(Fe) under different conditions; ESR signals of (D) DMPO-HO• and (E) DMPO-O<sub>2</sub><sup>•-</sup> in different photocatalytic systems. (D) Reuse stability of g-C<sub>3</sub>N<sub>4</sub>/MIL-101(Fe) for BPA degradation; (E) Proposed photocatalytic mechanism of g-C<sub>3</sub>N<sub>4</sub>/MIL-101(Fe) heterojunction. Adapted with permission from Ref. <sup>229</sup>, © 2018 The Royal Society of Chemistry.

In addition to Type-I heterojunction, UV-active UiO-66(Zr)<sup>231, 232</sup>, MIL-125(Ti)<sup>234, 235</sup> and visible light-active Fe-MOFs<sup>221, 224, 227, 229</sup> were also reported to form Type II heterojunctions with g-C<sub>3</sub>N<sub>4</sub>. For example, g-C<sub>3</sub>N<sub>4</sub>/MIL-101(Fe) composite were fabricated for degradation of bisphenol A (BPA) with persulfate (PS) under visible light. Combined with the results in Mott-Schottky plots (measuring flat band potential) and UV-Vis DRS spectra (measuring band gap  $E_g$ ), the CB and VB positions of g-C<sub>3</sub>N<sub>4</sub> were estimated to be -1.1 V and 1.7 V (vs SCE), respectively. The corresponding LUMO and HOMO values were -0.7 V and 1.9 V (vs SCE) for MIL-101(Fe), respectively. As shown in Fig. 31A, under visible light irradiation, the photogenerated electrons (e<sup>-</sup>) will transfer from the CB of g-C<sub>3</sub>N<sub>4</sub> to the LUMO of MIL-101(Fe). Meanwhile, holes (h<sup>+</sup>) will transfer from the HOMO of MIL-101(Fe) to VB of g-C<sub>3</sub>N<sub>4</sub>. In this way, efficient separation of photogenerated charges can be achieved. Thus, for the visible light-induced degradation of BPA, the g-C<sub>3</sub>N<sub>4</sub>/MIL-101(Fe)

composite displayed dramatically enhanced performance relative to single MIL-101(Fe) and g-C<sub>3</sub>N<sub>4</sub> (Fig. 31B). The electron transfer process as well as reactive centers were further investigated by ESR analysis. As shown in Fig. 31C, obvious ESR signal can be observed under dark condition in MIL-101(Fe), which was ascribed to Fe<sup>3+</sup> in FeO<sub>6</sub>. Subsequently, this signal can be totally quenched under visible light irradiation, indicating the disappearance of Fe<sup>3+</sup>. Due to the presence of extensive Fe–O clusters, which can be directly excited by visible light, the charge transfer from O<sup>2-</sup> to Fe<sup>3+</sup> will lead to reduction of Fe<sup>3+</sup> to Fe<sup>2+</sup>. Interestingly, after the addition of PS, the ESR signal of Fe<sup>3+</sup> can be regenerated, which may be originated from the oxidation of Fe<sup>2+</sup> to Fe<sup>3+</sup> by PS. Thus, it can be deduced that the active sites for PS activation were metal centers (Fe) in the network of MIL-101(Fe). Besides, stronger signals of DMPO–HO• and DMPO–O<sub>2</sub>•<sup>-</sup> were also observed in g-C<sub>3</sub>N<sub>4</sub>/MIL-101(Fe) composite relative to single ones. The oxidation of H<sub>2</sub>O/HO<sup>-</sup> by SO<sub>4</sub>•<sup>-</sup> led to the production of HO•. Thus, all the active species together boosted the degradation of BPA.

Direct Z-scheme heterojunction was also reported in the fabrication of MIL-88A(Fe)/g-C<sub>3</sub>N<sub>4</sub> composite.<sup>223</sup> The introducing of MIL-88A(Fe) can significantly promoted the separation of photogenerated charges. For example, lower PL intensity, higher photocurrent response and lower charge transfer resistance were observed on MIL-88A(Fe)/g-C<sub>3</sub>N<sub>4</sub> relative to single components. Therefore, for the photocatalytic degradation of colorful RhB dye and colorless organic pollutants (phenol and tetracycline), the binary composite exhibited excellent performance. Under visible light irradiation, the estimated rate constant for RhB was ca. 0.16 min<sup>-1</sup>, which was ca. 253 and 5 times that on MIL-88A and g-C<sub>3</sub>N<sub>4</sub>, respectively.

### 3.8 MOFs/COFs coupling

During the past decades, great progress has been achieved in the modification of MOFs. Among the various modification strategies, coupling MOFs with another MOFs may possess the merits of individual MOFs and bring in new properties. For example, MOFs–MOFs hybrid materials with core–shell,<sup>238–240</sup> Janus<sup>241, 242</sup> and hierarchical structures<sup>243, 244</sup> have been fabricated and applied in many fields, such as catalysis,<sup>245</sup> gas detection<sup>246</sup> and chemical/biological sensing.<sup>247</sup> Since photoactive MOFs possess semiconductor-like behavior, the coupling of different MOFs with matched HOMO-LUMO positions may also lead to formation of heterojunctions, which

subsequently promoted the separation of photogenerated charges as well as photocatalytic performance.<sup>248-252</sup> For example, hierarchical MIL-101(Cr)@NH<sub>2</sub>-MIL-125(Ti) hybrid were developed via internal extended growth method, which displayed enhanced performance for Cr(VI) reduction under visible light.<sup>248</sup> PCN-222/MOF-545 with porphyrin functionality, high porosity and exceptional stability were prepared and applied for the selective degradation of mustard-gas simulant (2-chloroethyl ethyl sulfide) to nontoxic 2-chloroethyl ethyl sulfoxide.<sup>251</sup> As for Fe-MOFs with strong visible light absorption, MIL-100(Fe)/MIL-53(Fe) composite with Type II heterojunction were fabricated *via* electrostatic interaction with each other. For the photocatalytic degradation of Microcystin-LR (MC-LR), the hybrid material displayed enhanced activity than single MIL-53(Fe) and MIL-100(Fe) (Fig. 32A).<sup>253</sup> More importantly, the leaching of Fe<sup>3+</sup> was significantly suppressed in hybrid MOFs (Fig. 32B). The reason may be ascribed to electrostatic attracting effect between the two kinds of Fe-MOFs, since the surface of MIL-101 and MIL-53 was negatively and positively charged (at pH 6), respectively. Considering the matched LUMO and HOMO positions, more efficient charge separation can be anticipated (Fig. 32C). Thus, the complete degradation of MC-LR (4.5 mg/L) can be achieved at very low dosage (0.02 g/L) of MIL-100/MIL-53 (Fe).

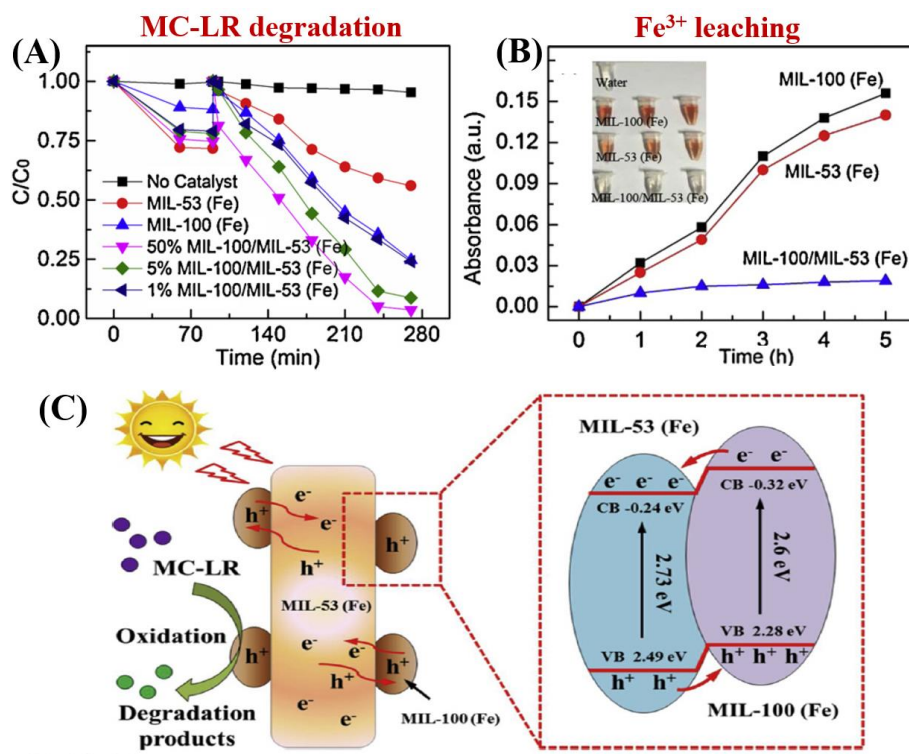


**Fig. 32.** (A) Photocatalytic degradation of MC-LR by different samples under visible light; (B) Comparison of Fe(III) ion leaching from MIL-53 (Fe), MIL-100(Fe) and MIL-100(Fe)/MIL-53(Fe), Inset: the photo of the aqueous

solution during the photocatalytic process; (B) Proposed mechanism for charge separation and MC-LR degradation by optimized MIL-100(Fe)/MIL-53(Fe) under visible light. Adapted with permission from ref. <sup>253</sup>, © 2019 Elsevier.

Similar to MOFs, metal-free covalent organic frameworks (COFs) are another kind of porous crystalline materials, which have recently attracted increasing attention in photocatalysis.<sup>254-256</sup> Moreover, the MOF-COF hybrid photocatalysts have also been developed.<sup>257, 258</sup> For example, core-shell NH<sub>2</sub>-MIL-68(In)@TPA-COF with high crystallinity and hierarchical porosity was fabricated according to the procedure depicted in Fig. 33A.<sup>257</sup> The growth of sheet-like TPA-COF on the surface of rod-like NH<sub>2</sub>-MIL-68(In) can be obviously observed (Fig. 33B). Besides, the incorporation of TPA-COF were further verified by XRD (Fig. 33C) and FT-IR analysis. Since TPA-COF (2.32 eV) has narrower band gap than NH<sub>2</sub>-MIL-68(In) (2.82 eV), the MOFs-COF hybridization led to even smaller band gap (Fig. 33D), corresponding to more efficient utilization of visible light. Besides, due to the introduction of TPA-COF (1136 m<sup>2</sup>/g), the BET surface area increased from 451 m<sup>2</sup>/g for NH<sub>2</sub>-MIL-68(In) to 539 m<sup>2</sup>/g for the hybrid material. Thus, for the photocatalytic degradation of RhB, the NH<sub>2</sub>-MIL-68(In)@TPA-COF hybrid displayed enhanced activity.

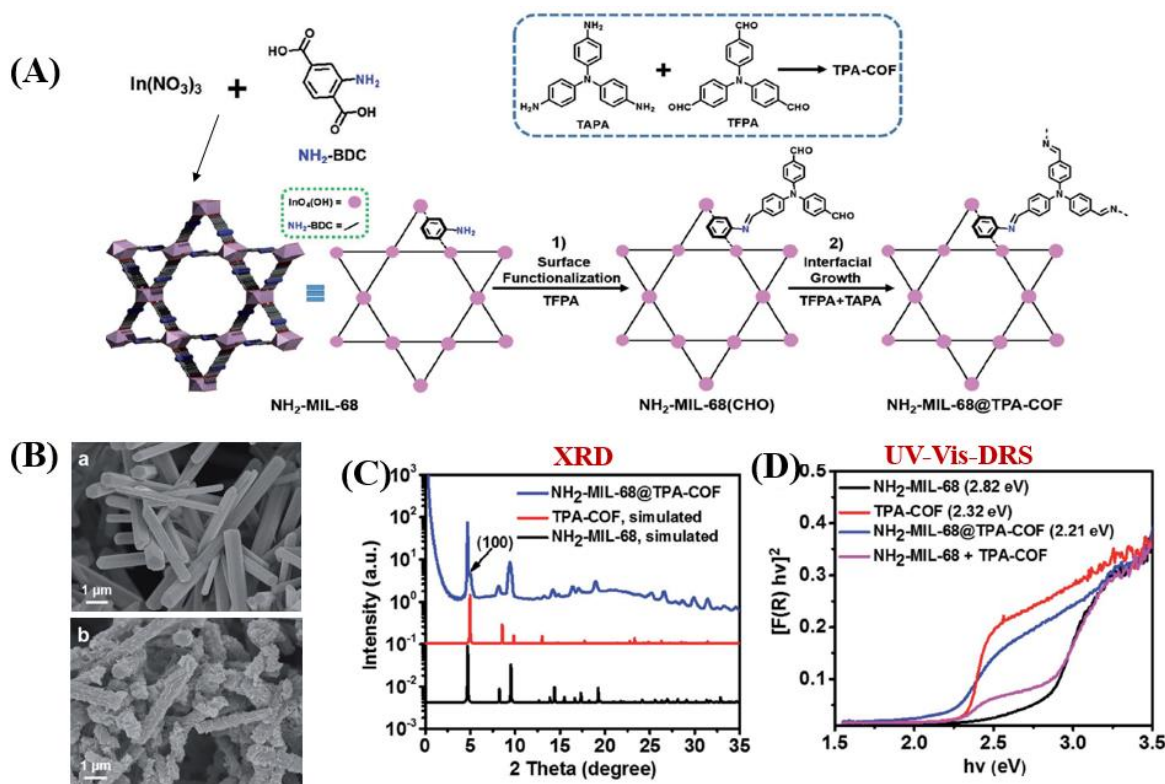


**Fig. 33.** (A) Schematic illustrations for the fabrication of  $\text{NH}_2\text{-MIL-68(In)}@\text{TPA-COF}$ ; (B) SEM images of (a)  $\text{NH}_2\text{-MIL-68(In)}$  and (b)  $\text{NH}_2\text{-MIL-68(In)}@\text{TPA-COF}$ ; (C) XRD patterns and (D) UV-Vis-DRS of different samples. Adapted with permission from ref. <sup>257</sup>, © 2017 WILEY-VCH.

Recently, a series of covalently integrated MOF/COF composites with direct Z-scheme heterojunctions were also synthesized *via* facial one-pot procedure, such as  $\text{NH}_2\text{-MIL-125(Ti)/TTB-TTA}$ ,  $\text{NH}_2\text{-MIL-53(Al)/TTB-TTA}$  and  $\text{NH}_2\text{-UiO-66(Zr)/TTB-TTA}$ .<sup>258</sup> Due to well-matched HOMO-LUMO positions and promoted separation of charge carriers across heterojunction interface, significantly enhanced performance can be observed for the photocatalytic degradation of phenol and MO. Besides, the  $\text{NH}_2\text{-MIL-125(Ti)/TTB-TTA}$  composite with highest activity became extremely stable after the incorporation of TTB-TTA COF. Thus, the hybridation of MOFs with metal free COFs will be very attractive due to the formation of heterojunction, retention of high surface area and structural stability.

### 3.9 Hybrid modification strategies

As described above, many single strategies have been reported to modify MOFs for enhanced photocatalytic performance. Each strategy has its own merits and limitations. For better utilization of the merits, proper combination of different strategies may lead to synergistic effect.

As listed in Table 7, many hybrid modification strategies were established and displayed further enhanced photocatalytic performance relative to single strategy. For example, MOFs can be co-modified using MNPs and photoactive semiconductors, MNPs and conducting carbon materials, conducting carbon materials and photoactive semiconductors, and etc. Besides, different photoactive semiconductors were also coupled with MOFs constructing multi-heterojunctions for more efficient charge separation.

**Table 7** Hybrid modification strategies for photocatalytic removal of environmental pollutants under visible light.

Composites	<sup>a</sup> S <sub>BET</sub> (m <sup>2</sup> /g)	Pollutant	C <sub>pollutant</sub> (mg/L)	C <sub>catalyst</sub> (g/L)	Time (min)	<sup>b</sup> η <sub>composite</sub> (%)	Ref.
<b>Co-modification of MOFs using MNPs and photoactive semiconductors</b>							
Ag/AgCl@ZIF-8	367	ACT	1.0	0.5	90	99	259
Ag/AgCl/ZIF-8	576	RhB	10	1.0	60	98	260
Ag@AgCl/Ag nanofilm/ZIF-8	23	MB	10	1.0	12	96	261
Pt/ZIF-8/TiO <sub>2</sub> -NTs	1100	phenol	52	NA	120	19	262
Ag/AgCl@MIL-53(Fe)	NA	RhB	10	0.4	45	100	263
		Cr(VI)	10	0.4	240	100	
MIL-53(Fe)/Ag/g-C <sub>3</sub> N <sub>4</sub> ;	NA	CLQ	10	0.2	100	95	264
Ag/AgCl@MIL-88A(Fe)	173	IBP	10	0.4	210	100	265
Ag/AgCl@MIL-101(Cr)	2016	RhB	20	1.0	18	96	266
MIL-125(Ti)/Ag/g-C <sub>3</sub> N <sub>4</sub>	101	NB	2050	0.83	240	43 <sup>e</sup>	267
UiO-66(Zr)/g-C <sub>3</sub> N <sub>4</sub> /Ag	705	RhB	20	0.4	180	93	268
		2,4-D	20	0.4	180	84	
Ag <sub>2</sub> CrO <sub>4</sub> /Ag/AgCl-HKUST-1 <sup>g</sup>	NA	AB	3	0.1	155	98	269
		OG	3	0.1	155	90	
Ag/Ag <sub>3</sub> PO <sub>4</sub> /HKUST-1	602	PBS	55.6	1.0	80	89	270
Ag <sub>3</sub> PO <sub>4</sub> /AgBr/Ag-HKUST-1 <sup>g</sup>	NA	MB	15	0.4	75	92	271
		ER	15	0.4	75	90	
		A-O	15	0.4	75	90	
<b>Co-modification of MOFs using MNPs and conducting carbon materials</b>							
Ag/GO/MIL-125(Ti)	730	RhB	50	0.4	50	95	272
Pd/GO/MIL-101(Cr)	NA	BC	25	0.25	15	100	273
		AF	25	0.25	15	100	
<b>Co-modification of MOFs using conducting carbon materials and photoactive semiconductors</b>							
BiOBr/GO/MOF-5	185	RhB	NA	NA	120	92	274
SnO <sub>2</sub> @UiO-66(Zr)/rGO	437	RhB	50	0.5	150	96	275
<b>Co-modification of MOFs using two different strategies</b>							
MIL-100(Fe)@Fe <sub>3</sub> O <sub>4</sub> /CA	390	TC	10	0.2	180	85	276
Fe-C oxides/MIL-101(Cr)	1116	X-3B <sup>c</sup>	100	0.1	120	100 <sup>d</sup>	277
TiO <sub>2</sub> @Salicylaldehyde-NH <sub>2</sub> -MIL-101(Cr)	853	MB <sup>c</sup>	30	0.125	60	86	278
H <sub>2</sub> TCPPc(I <sup>-</sup> )Meim-UiO-66	502	Cr(VI)	100	0.25	30	100	279
4-PySH@TiO <sub>2</sub> /PCN-222(Zn)	1401	RhB <sup>c</sup>	50	0.048	270	98	280
		2,4-DNP <sup>c</sup>	20	0.048	270	68	

**Co-modification of MOFs using different photoactive semiconductors**

BiOI@MIL-88A(Fe)@g-C <sub>3</sub> N <sub>4</sub>	70	AB92	10	0.1	180	88	281
		RhB	10	0.1	180	75	
		Phenol	10	0.1	180	70	
Ag <sub>3</sub> PO <sub>4</sub> /BiPO <sub>4</sub> @MIL-88B(Fe)@g-C <sub>3</sub> N <sub>4</sub>	NA	AB92	10	0.1	60	85	282
Ag <sub>3</sub> PO <sub>4</sub> /MIL-101(Cr)/NiFe <sub>2</sub> O <sub>4</sub>	313	RhB	10	0.2	30	95	283
CdS/g-C <sub>3</sub> N <sub>4</sub> /MIL-125(Ti)	238	RhB	NA	NA	60	94	284
CdS/NH <sub>2</sub> -MIL-125@TiO <sub>2</sub>	968	NO	NA	4.0	5	49	85
N-K <sub>2</sub> Ti <sub>4</sub> O <sub>9</sub> /g-C <sub>3</sub> N <sub>4</sub> /UiO-66(Zr)	288	RhB	10	0.2	180	68 <sup>d</sup>	285
Cd <sub>0.5</sub> Zn <sub>0.5</sub> S@UiO-66(Zr)@g-C <sub>3</sub> N <sub>4</sub>	147	MO	20	0.2	120	82	286
BiOI@NH <sub>2</sub> -UiO-66(Zr)@g-C <sub>3</sub> N <sub>4</sub>	123	RhB	20	0.2	80	95	287
		TC	20	0.2	180	79	
BiPO <sub>4</sub> /Bi <sub>2</sub> S <sub>3</sub> -HKUST-1	670	TB	25	0.25	65	99	288
		AO	25	0.25	65	98	
Ag <sub>3</sub> PO <sub>4</sub> /Bi <sub>2</sub> S <sub>3</sub> -HKUST-1 <sup>f</sup>	NA	TB	25	0.25	25	98	289
		VS	25	0.25	25	99	

NA: no experimental data available; rGO: reduced graphene oxide; GO: graphene oxide; CA: carbon aerogel; <sup>a</sup> S<sub>BET</sub> surface area were presented in integer numbers; <sup>b</sup> Removal efficiencies ( $\eta$ ) for pollutants were received or estimated from the figures in reference and presented in integer numbers; <sup>c</sup> Addition of H<sub>2</sub>O<sub>2</sub>; <sup>d</sup> UV-Vis light or sunlight; <sup>e</sup> under N<sub>2</sub> atmosphere with methanol as h<sup>+</sup> scavenger; <sup>f</sup> under the assistance of sonication; <sup>g</sup> measured in continuous flow photocatalytic rotating packed bed for the degradation of dye mixtures.



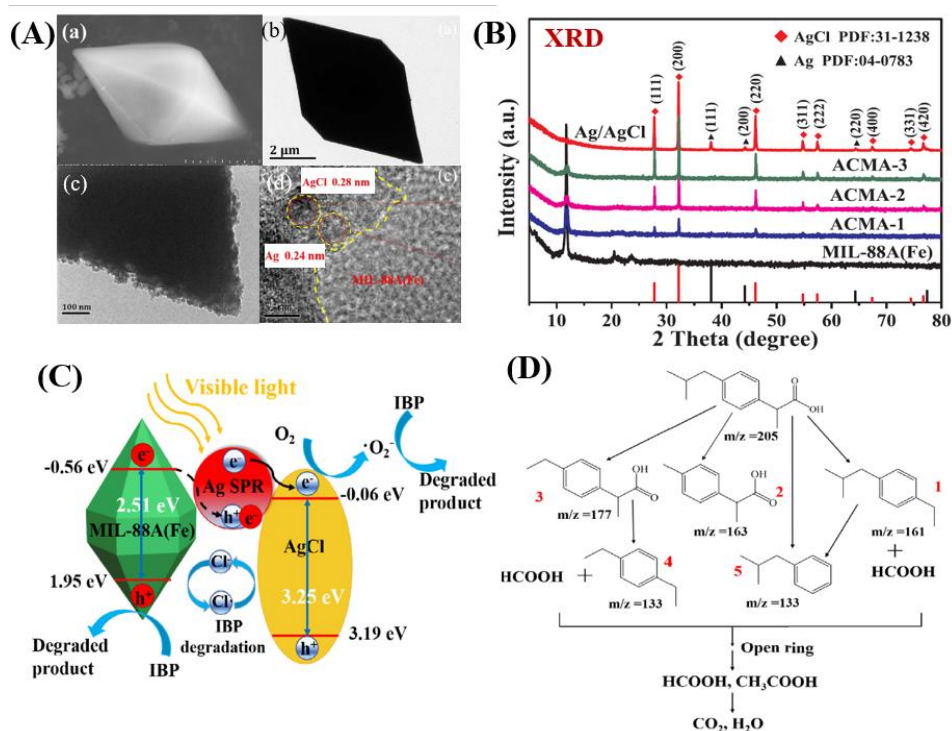


**Fig. 34.** (A) (a) SEM; (b) TEM; (c) and (d) HRTEM images of Ag/AgCl@MIL-88A(Fe); (B) XRD patterns of different samples; (C) Proposed mechanism for photocatalytic degradation of IBP by Ag/AgCl@MIL-88A(Fe) under visible light irradiation; (D) Proposed degradation pathway of IBP. Adapted with permission from ref. <sup>265</sup>, © 2018 Elsevier B.V.

Among the reported hybrid modification strategies, co-modification of MOFs using MNPs and photoactive semiconductors were frequently reported. Especially, plasmonic Ag nanoparticles were competitive in comparison with other noble metals (such as Au, Pt and Pd) due to lower price. Till now, various kinds of MOFs (such as ZIF-8, MIL-Fe, MIL-Ti and HKUST) have been co-modified using Ag nanoparticles and semiconductors for environmental photocatalysis. For example, plasmonic Ag/AgCl and spindle-shaped MIL-88A(Fe) were integrated forming Ag/AgCl@MIL-88A(Fe) (denoted as ACMA) ternary composite via one-pot solvothermal method.<sup>265</sup> As shown in Fig. 34A, Ag/AgCl nanoparticles were uniformed anchored on the surface of spindle-shaped MIL-88A(Fe) micro rods. The presence of metallic Ag were further verified by XRD analysis (Fig. 34B) and XPS investigation. The flat-band potential of ACMA was estimated to be  $-0.75$  V *via* Mott-Schottky plot measurement.<sup>290</sup> Thus, the electron transfer from the CB of ACMA to  $O_2$  forming reactive  $O_2^{\cdot-}$  (0.13 eV) was thermodynamically feasible. For the photocatalytic degradation of ibuprofen (IBP), Ag/AgCl@MIL-88A(Fe) composite exhibited significantly enhanced

performance relative to Ag/AgCl and MIL-88A(Fe). The ternary composite was optimized with Fe:Ag molar ratio of 2:1 in the initial preparing procedure. Furthermore, trapping experiments were carried out to investigate possible active species involved in the degradation of IBP by optimal ACMA-2. The addition of  $O_2^{\bullet-}$  (benzoquinone),  $h^+$  (EDTA-2Na) and  $e^-$  ( $AgNO_3$ ) scavengers all inhibited the degradation dynamics, while  $HO^{\bullet}$  scavenger (IPA) had negligible influence. Thus, it can be deduced that  $O_2^{\bullet-}$ ,  $h^+$  and  $e^-$  play dominant roles for IPA degradation.<sup>291</sup> The production of  $HO^{\bullet}$  ( $E_{HO^{\bullet}/HO^{\bullet}} = 2.38$  V vs NHE)<sup>59, 290</sup> was thermodynamically infeasible due to weak oxidative ability (Fig. 34C). The degradation products were further detected. As depicted in Fig. 34D, due to the combined effect of  $O_2^{\bullet-}$ ,  $h^+$  and  $e^-$ , the degradation of IBP started from decarboxylation (by-product 1 and 4) and direct loss of functional groups (by-product 2, 3 and 5). The subsequent ring opening process led to the formation of  $HCOOH$  and  $CH_3COOH$ , which finally were mineralized into  $CO_2$  and  $H_2O$ .

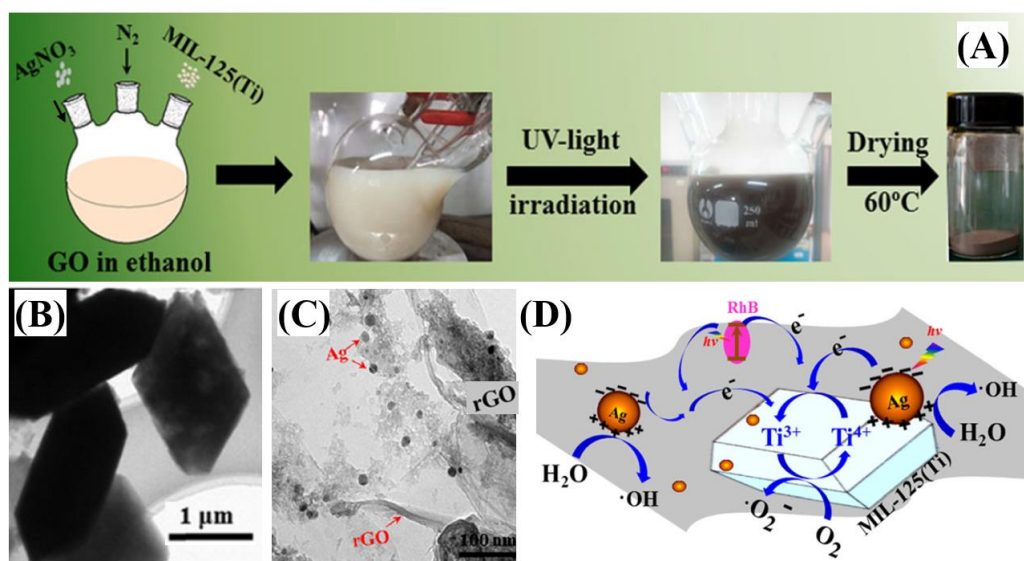


**Fig. 35.** (A) Schematic processes for the preparing of Ag/rGO/MIL-125(Ti); (B) TEM image of MIL-125(Ti); (C) HRTEM image (insert: TEM image) of Ag/rGO/MIL-125(Ti); (D) Proposed mechanism for photocatalytic degradation of RhB by Ag/rGO/MIL-125(Ti) ternary composite. Adapted with permission from ref. <sup>272</sup>, © 2016 John Wiley.

The merits of MNPs and conducting carbon materials can also be combined *via* co-modification. For example, MIL-125(Ti) was modified with both Ag nanoparticles and rGO. As shown in Fig. 35A-C, bipyramid-like MIL-125(Ti) was wrapped with rGO and Ag nanoparticles via one-pot self-assembly and photoreduction method. The BET surface area slightly decreased from  $755$   $m^2/g$

for pristine MIL-125(Ti) to  $730 \text{ m}^2/\text{g}$  for Ag/rGO/MIL-125(Ti) with negligible influence on average pore diameter (2.2 nm vs 2.3 nm), indicating the maintenance of microporous structure. Besides, the presence of Ag nanoparticles and rGO can promote the separation of photogenerated charges, which was elucidated by PL spectra. Thus, under visible light irradiation, Ag can be excited to generate  $e^-h^+$  pairs due to plasmonic effect (Fig. 35D). Due to the presence of rGO, the electrons can be more easily transferred to  $\text{Ti}^{4+}$  metal center in MIL-125(Ti). The reduced intermediate  $\text{Ti}^{3+}$  will be re-oxidized by  $\text{O}_2$  generating reactive  $\text{O}_2^{\bullet-}$ . rGO can also facilitate the interfacial electron transfer from Ag plasma to  $\text{O}_2$ . Meanwhile,  $\text{HO}^\bullet$  can be generated by capturing  $h^+$ . Thus, due to the formation of the above active species, the photocatalytic performance for RhB degradation was accelerated on co-modified MIL-125(Ti) relative to single strategy modified MOFs. The rate constant was in the order of Ag/MIL-125(Ti) ( $0.052 \text{ min}^{-1}$ ) < rGO/MIL-125(Ti) ( $0.0595 \text{ min}^{-1}$ ) < Ag/rGO/MIL-125(Ti) ( $0.0644 \text{ min}^{-1}$ ).

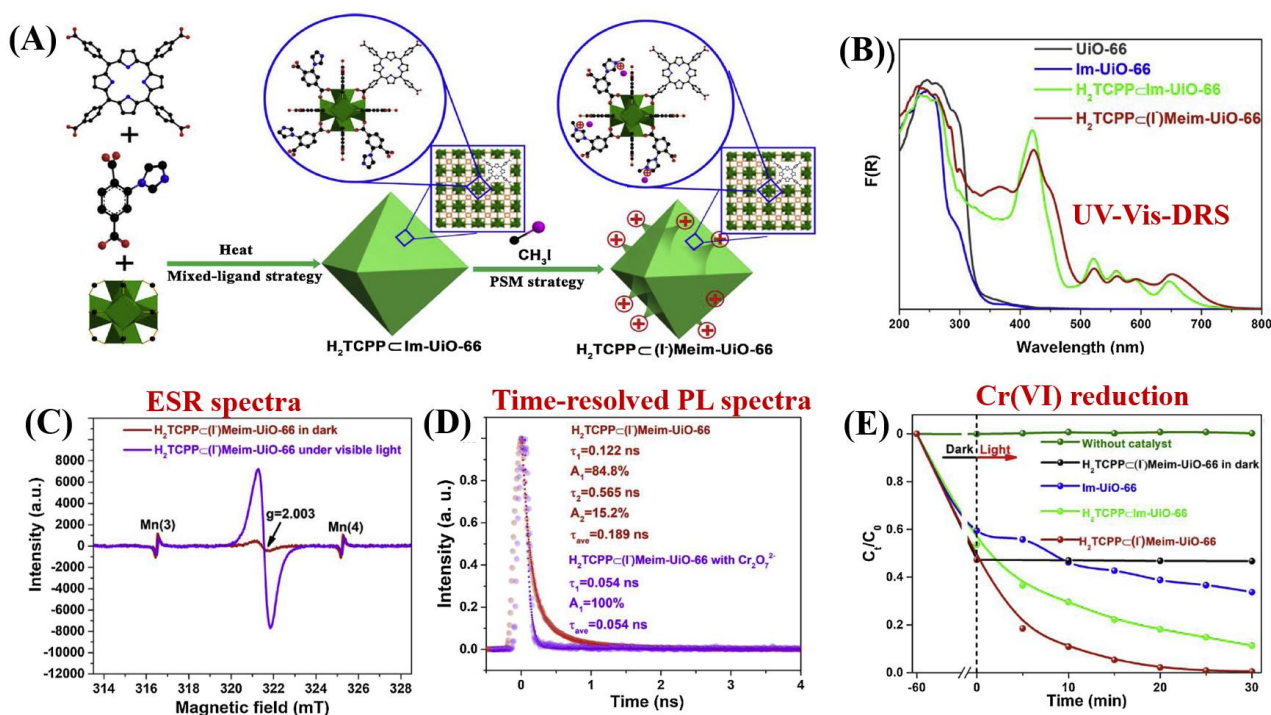


**Fig. 36.** (A) Schematic processes for the preparing of  $\text{H}_2\text{TCPP}-(\text{I})\text{Meim-Uio-66}$ ; (B) UV-vis-DRS of different samples; (C) ESR analyses of  $\text{H}_2\text{TCPP}-(\text{I})\text{Meim-Uio-66}$  with Mn as internal standard; (D) Time-resolved PL spectra of  $\text{H}_2\text{TCPP}-(\text{I})\text{Meim-Uio-66}$  suspensions with and without the presence of  $\text{Cr}_2\text{O}_7^{2-}$  at emission of 650 nm ( $\lambda_{\text{ex}}=400 \text{ nm}$ ); (E) Photocatalytic reduction of Cr(VI) by different samples under visible light irradiation. Adapted with permission from ref. <sup>279</sup>, © 2019 Elsevier B.V.

Generally, the starting point of most hybrid modification strategies is focused on the formation, separation and transfer of charge carriers, which finally led to enhanced performance for removal of pollutants. Whereas, the design of proper modification strategy according to the characteristics of target pollutants, may be a more promising way. For example, for efficient reduction of Cr(VI) (in the form of anionic  $\text{Cr}_2\text{O}_7^{2-}$  at neutral pH), visible light-harvesting unit (porphyrin) and Cr(VI) adsorption site ( $\text{CH}_3^+$ ) were simultaneously integrated into single MOFs (UiO-66). As illustrated in Fig. 36A,  $\text{H}_2\text{TCPP}(\Gamma)\text{Meim-UiO-66}$  ( $\Gamma^-$  as mobile counter anion) was fabricated via sequential mixed-ligand and ionization routes. The incorporation of  $\text{H}_2\text{TCPP}$  ligand with porphyrin unit could extend the absorption of UiO-66 from UV to visible region (Fig. 36B). Meanwhile, the cationic struts could lead to enhanced adsorption of anionic  $\text{Cr}_2\text{O}_7^{2-}$ . Besides, the generation, separation and transfer of charge carriers in UiO-66 were also promoted after co-modification. Furthermore, the electron transfer from excited porphyrin to  $\text{Zr}^{4+}$  centers can be confirmed from the greatly enhanced ESR signals ( $g = 2.003$ ) under visible light (Fig. 36C). Time-resolved PL spectra were also applied to track the photoexcited carrier in  $\text{H}_2\text{TCPP}(\Gamma)\text{Meim-UiO-66}$  (Fig. 36D). After in-situ addition of Cr(VI), the long time constant ( $\tau_2$ ) totally disappeared, indicating fast transfer of electrons from  $\text{H}_2\text{TCPP}$  to Cr(VI). Thus, due to the above synergistic effect, the photocatalytic reduction of Cr(VI) was significantly boosted (Fig. 36E). After 30 min visible light irradiation, 100 mg/L Cr(VI) can be completely removed *via* adsorption and photoreduction by 0.25 g/L  $\text{H}_2\text{TCPP}(\Gamma)\text{Meim-UiO-66}$ . Herein, the concentration of Cr(VI) was far higher than most studies (10 mg/L). In other words, the rate for Cr(VI) reduction in the present system was  $13.3 \text{ mg}_{\text{Cr(VI)}}/\text{g}_{\text{catalyst}}/\text{min}$ , which was far higher than previous reported MOFs-based systems. For example, the value was  $0.2 \text{ mg}_{\text{Cr(VI)}}/\text{g}_{\text{catalyst}}/\text{min}$  for  $\text{NH}_2\text{-UiO-66(Zr)}$  and  $1.6 \text{ mg}_{\text{Cr(VI)}}/\text{g}_{\text{catalyst}}/\text{min}$   $\text{NH}_2\text{-MIL-125(Ti)}$ , respectively. Thus, for the removal of environmental pollutants, targeted modification strategies deserve intensive study.

### 3.10 Carrier loading and magnetic recovery

In addition to high reactivity, good recyclability also played an important role for further large-scale industrial applications. Since most pristine MOFs are highly dispersive in water and difficult to be separated, it is therefore desirable to enhance the recyclability. Typically, immobilization on an inert carrier or introducing a magnetic component were proved to be two promising approaches. As listed in Table 8, Resin and SBA-15 were applied as supports to immobilize MOFs

with enhanced stability and photocatalytic performance.

**Table 8.** MOFs-based composites with easy recyclability for photocatalytic removal of environmental pollutants.

Composite	<sup>a</sup> <i>S</i> <sub>BET</sub> Variation (m <sup>2</sup> /g)	Pollutant	<i>C</i> <sub>pollutant</sub> (mg/L)	<i>C</i> <sub>catalyst</sub> (g/L)	Time (min)	<sup>b</sup> <i>η</i> Variation (%)	Ref.
<b><u>Immobilization on inert carriers</u></b>							
Resin/MIL-53 (Fe)	NA	SRB	3.3 <sup>c</sup>	0.17	120	24→96	292
A@FeBTC <sup>d</sup>	NA	RhB	35	0.4	60	69→99	293
HKUST-1/SBA-15	197→532	MG	10	0.25	80	NA→99	70
		SO	15	0.25	80	NA→88	
<b><u>Combined with magnetic component</u></b>							
Fe <sub>3</sub> O <sub>4</sub> @ZIF-67	301	CR	7	0.5	30	NA→95	294
Fe <sub>3</sub> O <sub>4</sub> /MIL-53(Fe)	NA	RhB <sup>e</sup>	10	0.4	70	99→99	295
γ-Fe <sub>2</sub> O <sub>3</sub> /MIL-53(Fe)	1835→60	MB	10	0.4	240	87→72	296
Fe <sub>3</sub> O <sub>4</sub> @MIL-100(Fe)	1766→1245	DCF <sup>e</sup>	60	0.1	120	100→91	297
Fe <sub>3</sub> O <sub>4</sub> @MIL-100(Fe)	1646→213	MB <sup>e</sup>	50	0.1	120	68→99	298
MIL-100(Fe)@Fe <sub>3</sub> O <sub>4</sub> /CA <sup>f</sup>	725→390	TC	10	0.2	180	42→85	276

NA: no experimental data available; <sup>a</sup> *S*<sub>BET</sub> variation indicates the surface area of MOFs before and after forming composite; <sup>b</sup> Removal efficiencies (*η*) for pollutants were used received or estimated from the figures in reference and presented in integer numbers, *η* variation indicated the performance of MOFs before and after forming composite; <sup>c</sup> mM; <sup>d</sup> Amberlite IRA-200 resin; <sup>e</sup> Addition of H<sub>2</sub>O<sub>2</sub>; <sup>f</sup> CA: carbon aerogel.

For example, Huang's group investigated the immobilization of MIL-53(Fe) with anionic resin (Amberlite IRA 200) and cationic resin (Amberlite IRA 900), respectively. The resulting AMIL-53(Fe) and DMIL-53(Fe) behaved negligible changes in UV-Vis DRS spectra and Flat band potential measurements, indicating that the optical properties and electronic properties were not influenced after immobilization. Decreased charge transfer resistance can be deduced from EIS Nyquist plot with smaller radius of curvature. The different charge characteristic of AMIL-53(Fe)

and DMIL-53(Fe) led to prior adsorption and degradation of RhB and SRB, respectively. Especially, dramatic difference can be observed in the stability of MIL-53. As shown in Fig. 37, the leaching of Fe(III) ion from MIL-53 can be significantly inhibited on AMIL-53(Fe). The reason may be ascribed to the chelation effect between  $-\text{SO}_3^-$  group of Amberlite IRA200 and Fe(III). Accordingly, for the degradation of RhB, AMIL-53 exhibited highest stability after 5 cyclic runs.

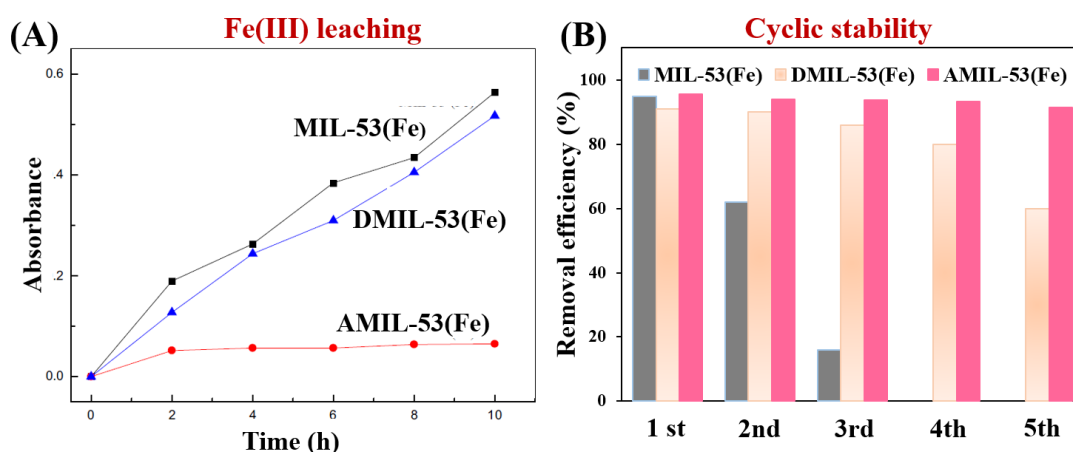


**Fig. 37.** (A) Comparison of Fe(III) ion leaching from MIL-53 (Fe), DMIL-53(Fe) and AMIL-53(Fe) in water under visible light irradiation; (B) Comparison of cyclic stability for RhB degradation over recycled MIL-53(Fe), DMIL-53(Fe) and AMIL-53(Fe). Adapted with permission from ref. <sup>292</sup>, © 2017 Elsevier.

As for preparing magnetically recyclable MOFs,  $\text{Fe}_3\text{O}_4$  nanoparticles with good magnetic properties and low toxicity were frequently applied to form composite with MOFs. However, due to easy photo-dissolution of  $\text{Fe}_3\text{O}_4$ , MOFs were designed as shell with  $\text{Fe}_3\text{O}_4$  as core. The as-prepared core-shell structure displayed good stability and recyclability. For example, Zhao's group reported the fabricating of core-shell  $\text{Fe}_3\text{O}_4@\text{MIL-100}(\text{Fe})$  microspheres (Fig. 38A-C).<sup>298</sup> Among the as-prepared  $\text{Fe}_3\text{O}_4@\text{MIL-100}(\text{Fe})$  samples, the one with 20 cycles exhibited highest photocatalytic performance for MB degradation in the presence of  $\text{H}_2\text{O}_2$  under visible light. Moreover, the performance of magnetic  $\text{Fe}_3\text{O}_4@\text{MIL-100}(\text{Fe})$  can be well maintained after four cyclic runs with negligible change in crystalline structure (Fig. 38D-E). Besides, Fe(III) ion leaching can be greatly inhibited after covering a MOF shell, and thicker shell is more beneficial (Fig. 38F). For example, the value for Fe(III) ion leaching decreased from 1.96 ppm on pristine MIL-100(Fe) to 0.41 ppm on  $\text{Fe}_3\text{O}_4@\text{MIL-100}(\text{Fe})$  prepared with 40 cycles. Mechanism study further indicated that the photogenerated  $\text{h}^+$  in the MOF shell can access the  $\text{Fe}_3\text{O}_4$  core, leading to efficient separation of

$e^-$ - $h^+$  pairs. The separated  $e^-$  can react with  $H_2O_2$  forming active  $HO\cdot$  radicals, which finally lead to degradation of MB dye (Fig. 38G).

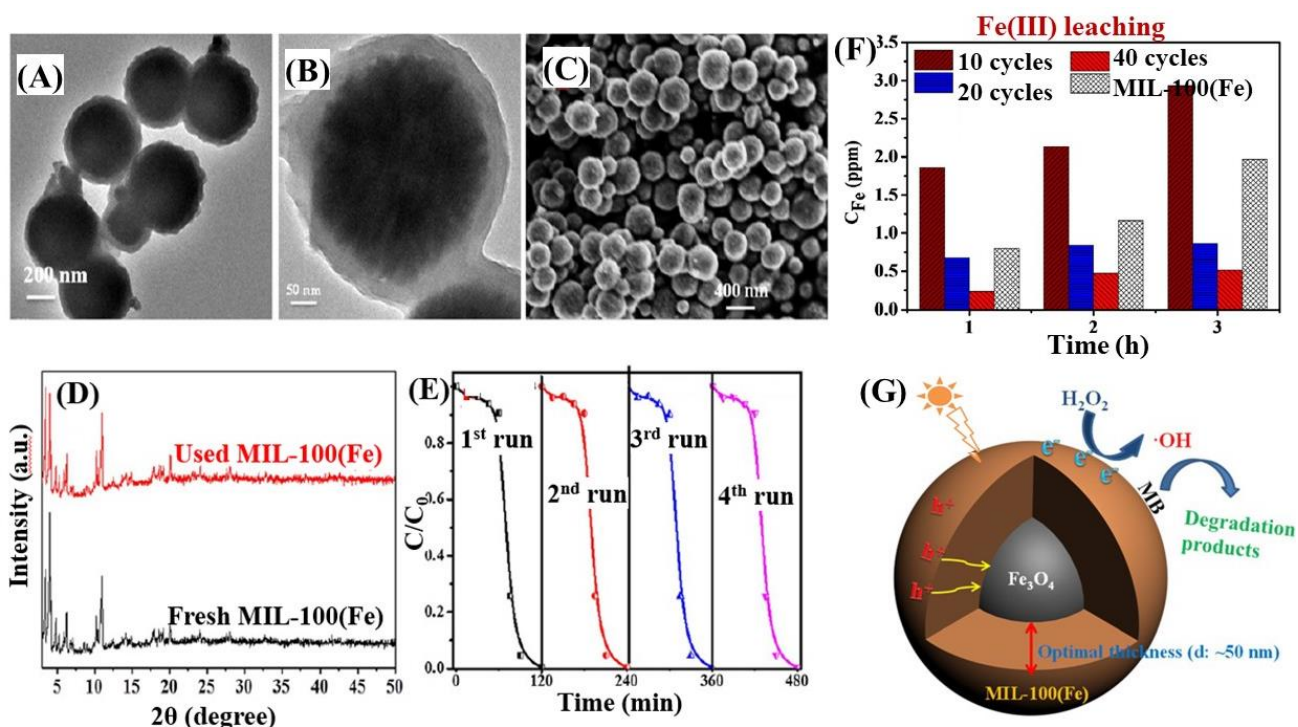


**Fig. 38.** The TEM (A-B) and SEM (C) images of used  $Fe_3O_4@MIL-100$  with 20 assembly cycles, which had been reacted with  $H_2O_2$  for 180 min at pH 3.00; (D) Comparison of XRD patterns between fresh MIL-100(Fe) and used MIL-100(Fe); (E) Cyclic degradation of MB using  $Fe_3O_4@MIL-100$  with 20 assembly cycles; (F) Comparison of Fe(III) ion leaching in water from different  $Fe_3O_4@MIL-100(Fe)$  samples; (G) Proposed mechanism for MB degradation. Adapted with permission from ref. <sup>298</sup>, © 2015 Wiley-VCH.

#### 4. Conclusions and Outlook

In this review, we summarize and illustrate recent progress in MOF-based photocatalysis for environmental remediation. The unparalleled versatility of MOFs allows many strategies to modify and regulate pristine MOFs for enhanced photocatalytic performance under visible light. However, MOF-based environmental photocatalysis is currently in the stage of infancy, which needs to be further developed as amiable and stable technology for low cost practical applications in the future. In general, intensive research work should be carried out to overcome the following challenges and obstacles:

- (1) Most photo-active MOFs are still at the stage of lab-scale, which cannot be fabricated by

one-time high-throughput synthesis. Besides, some preparing methods are complicate and difficult to control. The development of more facile synthetic routes, especially one-step approach under mild conditions, will be highly desirable for future large-scale applications.

(2) Although there are many reports on water-resistant MOFs, such as UiO-66, MIL-125, MIL-101 and ZIF series, the stability under harsh conditions (strong acidic and alkaline pH) still need to be improved. Besides, according to metal–ligand bond strengths and the HSAB (hard/soft acid/base) principle,<sup>5</sup> the selection of high-valent metal ions (such as Mo<sup>6+</sup>, W<sup>6+</sup>, and etc.) as metal centers may arose great interest for fabricating novel stable MOFs.

(3) As for MNPs/MOFs composites, most of the loaded metal nanoparticles were precious metals (such as Pd, Pt, Au, and Ag). More researches on non-precious metals (such as Cu and Bi) deserve exploring.

(4) In addition to immobilization on inert carrier and introducing magnetic component, the fabrication of MOFs films is another attractive way for the recycling of MOFs. However, the utilization of MOFs films for environmental photocatalysis was very limited. Especially, the fabricating of MOFs films on conductive substrate, need to be further developed for photoelectrocatalytic degradation of organic pollutants and reduction of heavy metal ions.

(5) Up to now, multi-functional applications of MOFs were limited. There are only sporadic reports on simultaneous photocatalytic oxidation of dyes and reduction of Cr(VI) or H<sup>+</sup> (H<sub>2</sub> production)<sup>47, 135, 150, 299</sup>. More efficient multi-functional MOFs are required for the simultaneous and synergistic removal of environmental pollutants and production of energy or valuable products in one system.

(6) For better regulation of MOFs photocatalysis, more efforts are needed to intensively explore the degradation processes. For example, the toxicity of degradation intermediates should be evaluated due to incomplete mineralization of organic pollutants under most circumstances.

(7) In addition to the detection of active species (such as HO•, O<sub>2</sub>•<sup>-</sup> and h<sup>+</sup>) during photocatalysis, more details associated with photocatalytic mechanism need in-depth investigation. For example, the adsorption sites of contaminants on the surface/in the channel of MOFs, interfacial electron transfer mechanism as well as the rate limiting step should be identified. Based on these, the design of appropriate modification strategies will be more scientific and effective.

(8) Finally, there is still urgent need to develop novel robust MOFs with excellent light



harvesting property, high stability and easy recyclability through the engineering of metallic nodes and organic linkers.

In summary, although there are still many challenges to be solved, in the past two decades of development, researchers from all over the world have made great progress for MOFs materials from structural design, controllable modification to functional applications. We believe that with the joint efforts of researchers in many fields, the prospects of MOFs for environmental photocatalysis will be definitely bright.

## Acknowledgments

The authors are grateful for the financial support of National Natural Science Foundation of China (21876154), Zhejiang Provincial Natural Science Foundation of China (LR18B070001), the US National Science Foundation (CBET-1706025) and the University of South Florida. The authors also extend their appreciation to the Distinguished Scientist Fellowship Program (DSFP) at King Saud University for partial funding of this work.

## Reference

- 1 J. Schneider, M. Matsuoka, M. Takeuchi, J. Zhang, Y. Horiuchi, M. Anpo and D. W. Bahnemann, *Chem. Rev.* 2014, **114**, 9919.
- 2 M. N. Chong, B. Jin, C. W. K. Chow and C. Saint, *Water Res.* 2010, **44**, 2997.
- 3 H. C. Zhou and S. Kitagawa, *Chem. Soc. Rev.* 2014, **43**, 5415.
- 4 H. Furukawa, N. Ko, Y. B. Go, N. Aratani, S. B. Choi, E. Choi, A. Ö. Yazaydin, R. Q. Snurr, M. O'Keeffe, J. Kim and O. M. Yaghi, *Science* 2010, **329**, 424.
- 5 T. Devic and C. Serre, *Chem. Soc. Rev.* 2014, **43**, 6097.
- 6 E. M. Dias and C. Petit, *J. Mater. Chem. A* 2015, **3**, 22484.
- 7 J. Bedia, V. Muelas-Ramos, M. Peñas-Garzón, A. Gómez-Avilés, J. J. Rodríguez and C. Bolver, *Catalysts* 2019, **9**, 52.
- 8 C. C. Wang, X. D. Du, J. Li, X. X. Guo, P. Wang and L. Zhang, *Appl. Catal. B: Environ.* 2016, **193**, 198.
- 9 J. D. Xiao, D. Li and H. L. Jiang, *Sci. Sin. Chim.* 2018, **48**, 1058.
- 10 J. L. Wang, C. Wang and W. Lin, *ACS. Catal.* 2012, **2**, 2630.
- 11 J. He, Y. Zhang, J. He, X. Zeng, X. Hou and Z. Long, *Chem. Commun.* 2018, **54**, 8610.
- 12 M. A. Nasalevich, M. van der Veen, F. Kapteijn and J. Gascon, *CrystEngComm* 2014, **16**, 4919.
- 13 D. Wang, M. Wang and Z. Li, *ACS. Catal.* 2015, **5**, 6852.
- 14 C. Wang, X. Liu, N. Keser Demir, J. P. Chen and K. Li, *Chem. Soc. Rev.* 2016, **45**, 5107.
- 15 P. Li, J. Li, X. Feng, J. Li, Y. Hao, J. Zhang, H. Wang, A. Yin, J. Zhou, X. Ma and B. Wang, *Nat. Commun.* 2019, **10**, 2177.
- 16 Y. Shi, A. F. Yang, C. S. Cao and B. Zhao, *Coordin. Chem. Rev.* 2019, **390**, 50.
- 17 X. Ma, L. Wang, Q. Zhang and H. L. Jiang, *Angew. Chem. Int. Ed.* 2019, **58**, 12175.
- 18 C. C. Wang, Y. Q. Zhang, J. Li and P. Wang, *J. Mol. Struct.* 2015, **1083**, 127.

- 19 X. Yu, L. Wang and S. M. Cohen, *CrystEngComm* 2017, **19**, 4126.
- 20 S. N. Zhao, G. Wang, D. Poelman and P. Van Der Voort, *Molecules* 2018, **23**, 2947.
- 21 H. Liu, C. Xu, D. Li and H. L. Jiang, *Angew. Chem. Int. Ed.* 2018, **130**, 5477.
- 22 X. Liang, L. Chen, L. Zhang and C. Y. Su, *Chin. Sci. Bull.* 2018, **63**, 248.
- 23 Q. Xia, H. Wang, B. Huang, X. Yuan, J. Zhang, J. Zhang, L. Jiang, T. Xiong and G. Zeng, *Small* 2019, **15**, 1803088.
- 24 J. D. Xiao and H. L. Jiang, *Acc. Chem. Res.* 2019, **52**, 356.
- 25 L. Jiao, J. Y. R. Seow, W. S. Skinner, Z. U. Wang and H. L. Jiang, *Mater. Today* 2019, **27**, 43.
- 26 B. Pattengale, S. Yang, J. Ludwig, Z. Huang, X. Zhang and J. Huang, *J. Am. Chem. Soc.* 2016, **138**, 8072.
- 27 C. C. Wang, J. R. Li, X. L. Lv, Y. Q. Zhang and G. S. Guo, *Energy Environ. Sci.* 2014, **7**, 2831.
- 28 Y. Li, H. Xu, S. Ouyang and J. Ye, *Phys. Chem. Chem. Phys.* 2016, **18**, 7563.
- 29 J. Qiu, X. Zhang, Y. Feng, X. Zhang, H. Wang and J. Yao, *Appl. Catal. B: Environ.* 2018, **231**, 317.
- 30 J. Bedia, V. Muelas-Ramos, M. Peñas-Garzón, A. Gómez-Avilés, J. J. Rodríguez and C. Belder, *Catalysts* 2019, **9**, 52.
- 31 D. Wang and Z. Li, *Res. Chem. Interm.* 2017, **43**, 5169.
- 32 Z. Yan, H. Xi and L. Yuan, *Environ. Sci.* 2019, **40**, 1819.
- 33 Z. Zhang, X. Li, B. Liu, Q. Zhao and G. Chen, *RSC Adv.* 2016, **6**, 4289.
- 34 S. R. Thakare and S. M. Ramteke, *Catal. Commun.* 2017, **102**, 21.
- 35 H. Li, M. Eddaoudi, M. O'Keeffe and O. M. Yaghi, *Nature* 1999, **402**, 276.
- 36 S. Bordiga, C. Lamberti, G. Ricchiardi, L. Regli, F. Bonino, A. Damin, K. P. Lillerud, M. Bjorgen and A. Zecchina, *Chem. Commun.* 2004, 2300.
- 37 M. Alvaro, E. Carbonell, B. Ferrer, F. X. Llabres, I. Xamena and H. Garcia, *Chem. Eur. J.* 2007, **13**, 5106.
- 38 T. Tachikawa, J. R. Choi, M. Fujitsuka and T. Majima, *J. Phys. Chem. C* 2008, **112**, 14090.
- 39 S. Yuan, L. Feng, K. Wang, J. Pang, M. Bosch, C. Lollar, Y. Sun, J. Qin, X. Yang, P. Zhang, Q. Wang, L. Zou, Y. Zhang, L. Zhang, Y. Fang, J. Li and H. Zhou, *Adv. Mater.* 2018, **30**, 1704303.
- 40 J. H. Cavka, S. Jakobsen, U. Olsbye, N. Guillou, C. Lamberti, S. Bordiga and K. P. Lillerud, *J. Am. Chem. Soc.* 2008, **130**, 13850.
- 41 C. Gomes Silva, I. Luz, F. X. Llabrés i Xamena, A. Corma and H. García, *Chem. Eur. J.* 2010, **16**, 11133.
- 42 M. Dan-Hardi, C. Serre, T. Frot, L. Rozes, G. Maurin, C. Sanchez and G. Férey, *J. Am. Chem. Soc.* 2009, **131**, 10857.
- 43 L. Shen, R. Liang, M. Luo, F. Jing and L. Wu, *Phys. Chem. Chem. Phys.* 2015, **17**, 117.
- 44 J. Gascon, M. D. Hernández-Alonso, A. R. Almeida, G. P. M. van Klink, F. Kapteijn and G. Mul, *ChemSusChem* 2008, **1**, 981.
- 45 J. X. Liu, M. Y. Gao, W. H. Fang, L. Zhang and J. Zhang, *Angew. Chem. Int. Ed.* 2016, **55**, 5160.
- 46 H. Furukawa, K. E. Cordova, M. O'Keeffe and O. M. Yaghi, *Science* 2013, **341**, 1230444.
- 47 R. Liang, F. Jing, L. Shen, N. Qin and L. Wu, *J. Hazard. Mater.* 2015, **287**, 364.
- 48 Y. K. Seo, J. W. Yoon, J. S. Lee, Y. K. Hwang, C. H. Jun, J. S. Chang, S. Wuttke, P. Bazin, A. Vimont, M. Daturi, S. Bourrelly, P. L. Llewellyn, P. Horcajada, C. Serre and G. Férey, *Adv. Mater.* 2012, **24**, 806.
- 49 P. Horcajada, T. Chalati, C. Serre, B. Gillet, C. Sebrie, T. Baati, J. F. Eubank, D. Heurtaux, P. Clayette, C. Kreuz, J.-S. Chang, Y. K. Hwang, V. Marsaud, P.-N. Bories, L. Cynober, S. Gil, G. Férey, P. Couvreur and R. Gref, *Nat. Mater.* 2009, **9**, 172.
- 50 P. Horcajada, H. Chevreau, D. Heurtaux, F. Benyettou, F. Salles, T. Devic, A. Garcia-Marquez, C. Yu, H. Lavrard, C. L. Dutson, E. Magnier, G. Maurin, E. Elkaïm and C. Serre, *Chem. Commun.* 2014, **50**, 6872.
- 51 K. Leus, T. Bogaerts, J. De Decker, H. Depauw, K. Hendrickx, H. Vrielinck, V. Van Speybroeck and P. Van Der Voort, *Micropor. Mesopor. Mater.* 2016, **226**, 110.
- 52 Y. Fang, J. Wen, G. Zeng, F. Jia, S. Zhang, Z. Peng and H. Zhang, *Chem. Eng. J.* 2018, **337**, 532.
- 53 Y. K. Seo, J. W. Yoon, J. S. Lee, U. H. Lee, Y. K. Hwang, C. H. Jun, P. Horcajada, C. Serre and J. S. Chang, *Micropor.*

*Mesopor. Mater.* 2012, **157**, 137.

- 54 D. Wang, F. Jia, H. Wang, F. Chen, Y. Fang, W. Dong, G. Zeng, X. Li, Q. Yang and X. Yuan, *J. Colloid Interf. Sci.* 2018, **519**, 273.
- 55 M. C. Das, H. Xu, Z. Wang, G. Srinivas, W. Zhou, Y. F. Yue, V. N. Nesterov, G. Qian and B. Chen, *Chem. Commun.* 2011, **47**, 11715.
- 56 S. Pu, L. Xu, L. Sun and H. B. Du, *Inorg. Chem. Commun.* 2015, **52**, 50.
- 57 T. L. H. Doan, H. L. Nguyen, H. Q. Pham, N. N. Pham Tran, T. N. Le and K. E. Cordova, *Chem. Asian J.* 2015, **10**, 2660.
- 58 Y. Gao, S. Li, Y. Li, L. Yao and H. Zhang, *Appl. Catal. B: Environ.* 2017, **202**, 165.
- 59 L. Ai, C. Zhang, L. Li and J. Jiang, *Appl. Catal. B: Environ.* 2014, **148-149**, 191.
- 60 C. J. N. Liu, Z. Li, W. Huang, B. Gao, F. You and X. Zhang, *Mater. Lett.* 2019, **237**, 92.
- 61 W. Mei, D. Li, H. Xu, J. Zan, L. Sun, Q. Li, B. Zhang, Y. Wang and D. Xia, *Chem. Phys. Lett.* 2018, **706**, 694.
- 62 J. J. Du, Y. P. Yuan, J. X. Sun, F. M. Peng, X. Jiang, L. G. Qiu, A. J. Xie, Y. H. Shen and J. F. Zhu, *J. Hazard. Mater.* 2011, **190**, 945.
- 63 Y. Gao, G. Yu, K. Liu, S. Deng, B. Wang, J. Huang and W. Wang, *Chem. Eng. J.* 2017, **330**, 157.
- 64 R. Li, Z. Chen, M. Cai, J. Huang, P. Chen and G. Liu, *Appl. Surf. Sci.* 2018, **457**, 726.
- 65 F. Jing, R. Liang, J. Xiong, R. Chen, S. Zhang, Y. Li and L. Wu, *Appl. Catal. B: Environ.* 2017, **206**, 9.
- 66 B. Xu, H. Yang, Y. Cai, H. Yang and C. Li, *Inorg. Chem. Commun.* 2016, **67**, 29.
- 67 Y. Li, G. Hou, J. Yang, J. Xie, X. Yuan, H. Yang and M. Wang, *RSC Adv.* 2016, **6**, 16395.
- 68 W. T. Xu, L. Ma, F. Ke, F. M. Peng, G. S. Xu, Y. H. Shen, J. F. Zhu, L. G. Qiu and Y. P. Yuan, *Dalton Trans.* 2014, **43**, 3792.
- 69 A. M. G. Kirov, C. A. D. Caiuby, M. Díaz-García, I. Díaz and M. S-Sanchez, *Cryst. Growth. Des.* 2017, **17**, 1806.
- 70 S. Mosleh, M.R. Rahimi, M. Ghaedi, K. Dashtian and S. Hajati, *RSC Adv.* 2016, **6**, 17204.
- 71 H. X. M. C. Das, Z. Wang, G. Srinivas, W. Zhou, Y. Yue, V. N. Nesterov, G. Qian and B. Chen, *Chem. Commun.* 2011, **47**, 11715.
- 72 G. Wang, Q. Sun, Y. Liu, B. Huang, Y. Dai, X. Zhang and X. Qin, *Chem. Eur. J.* 2015, **21**, 2364.
- 73 A. N. Meng, L. X. Chaihu, H. H. Chen and Z. Y. Gu, *Scientific Reports* 2017, **7**, 6297.
- 74 Y. Fu, D. Sun, Y. Chen, R. Huang, Z. Ding, X. Fu and Z. Li, *Angew. Chem. Int. Ed.* 2012, **51**, 3364.
- 75 M. A. Nasalevich, M. G. Goesten, T. J. Savenije, F. Kapteijn and J. Gascon, *Chem. Commun.* 2013, **49**, 10575.
- 76 J. Gao, J. Miao, P. Z. Li, W. Y. Teng, L. Yang, Y. Zhao, B. Liu and Q. Zhang, *Chem. Commun.* 2014, **50**, 3786.
- 77 C. H. Hendon, D. Tiana, M. Fontecave, C. Sanchez, L. D'Arras, C. Sassoey, L. Rozes, C. Mellot-Draznieks and A. Walsh, *J. Am. Chem. Soc.* 2013, **135**, 10942.
- 78 K. Hendrickx, D. E. P. Vanpoucke, K. Leus, K. Lejaeghere, A. Van Yperen-De Deyne, V. Van Speybroeck, P. Van Der Voort and K. Hemelsoet, *Inorg. Chem.* 2015, **54**, 10701.
- 79 X. P. Wu, L. Gagliardi and D. G. Truhlar, *J. Am. Chem. Soc.* 2018, **140**, 7904.
- 80 A. Dhakshinamoorthy, Z. Li and H. Garcia, *Chem. Soc. Rev.* 2018, **47**, 8134.
- 81 R. Liang, R. Huang, X. Wang, S. Ying, G. Yan and L. Wu, *Appl. Surf. Sci.* 2019, **464**, 396.
- 82 L. Shi, T. Wang, H. Zhang, K. Chang, X. Meng, H. Liu and J. Ye, *Adv. Sci.* 2015, **2**, 1500006.
- 83 X. D. Du, X. H. Yi, P. Wang, W. W. Zheng, J. G. Deng and C. C. Wang, *Chem. Eng. J.* 2019, **356**, 393.
- 84 S. Hu, M. Liu, K. Y. Li, C. S. Song, G. I. Zhang and X. W. Guo, *RSC Adv.* 2017, **7**, 581.
- 85 S. Gao, W. Cen, Q. Li, J. Li, Y. Lu, H. Wang and Z. Wu, *Appl. Catal. B: Environ.* 2018, **227**, 190.
- 86 H. Wang, X. Yuan, Y. Wu, G. Zeng, X. Chen, L. Leng, Z. Wu, L. Jiang and H. Li, *J. Hazard. Mater.* 2015, **286**, 187.
- 87 R. W. Liang, L. J. Shen, F. F. Jing, W. M. Wu, N. Qin, R. Lin and L. Wu, *Appl. Catal. B: Environ.* 2015, **162**, 245.
- 88 J. Wang, J. Wu, L. Lu, H. Xu, M. Trivedi, A. Kumar, J. Liu and M. Zheng, *Front. Chem.* 2019, **7**,
- 89 L. F. Song, C. H. Jiang, C. L. Jiao, J. Zhang, L. X. Sun, F. Xu, W. S. You, Z. G. Wang and J. J. Zhao, *Cryst. Growth Des.* 2010, **10**, 5020.

- 90 S. Abednatanzi, P. G. Derakhshandeh, H. Depauw, F. X. Coudert, H. Vrielinck, P. V. D. Voort and K. Leus, *Chem. Soc. Rev.* 2019, **48**, 2535.
- 91 A. Dhakshinamoorthy, A. M. Asiri and H. Garcia, *Catal. Sci. Technol.* 2016, **6**, 5238.
- 92 M. Kim, J. F. Cahill, H. Fei, K. A. Prather and S. M. Cohen, *J. Am. Chem. Soc.* 2012, **134**, 18082.
- 93 L. G. Yu, Y. G. Sun and Z. L. Wang, *J. Mol. Struct.* 2019, **1180**, 209.
- 94 Y. Lee, S. Kim, J. K. Kang and S. M. Cohen, *Chem. Commun.* 2015, **51**, 5735.
- 95 D. Sun, W. Liu, M. Qiu, Y. Zhang and Z. Li, *Chem. Commun.* 2015, **51**, 2056.
- 96 A. Santiago Portillo, H. G. Baldoví, M. T. García Fernandez, S. Navalón, P. Atienzar, B. Ferrer, M. Alvaro, H. Garcia and Z. Li, *J. Phys. Chem. C* 2017, **121**, 7015.
- 97 J. Tu, X. Zeng, F. Xu, X. Wu, Y. Tian, X. Hou and Z. Long, *Chem. Commun.* 2017, **53**, 3361.
- 98 H. Yang, X. W. He, F. Wang, Y. Kang and J. Zhang, *J. Mater. Chem.* 2012, **22**, 21849.
- 99 S. Das, H. Kim and K. Kim, *J. Am. Chem. Soc.* 2009, **131**, 3814.
- 100 R. Li, X. Ren, H. Ma, X. Feng, Z. Lin, X. Li, C. Hu and B. Wang, *J. Mater. Chem. A* 2014, **2**, 5724.
- 101 D. Ao, J. Zhang and H. Liu, *J. Photochem. Photobio. A: Chem.* 2018, **364**, 524.
- 102 T. A. Vu, G. H. Le, C. D. Dao, L. Q. Dang, K. T. Nguyen, P. T. Dang, H. T. K. Tran, Q. T. Duong, T. V. Nguyen and G. D. Lee, *RSC Adv.* 2014, **4**, 41185.
- 103 J. Li, J. Yang, Y. Y. Liu and J. F. Ma, *Chem. Eur. J.* 2015, **21**, 4413.
- 104 A. Abbasi, M. Soleimani, M. Najafi and S. Geranmayeh, *Inorg. Chim. Acta* 2016, **439**, 18.
- 105 J. Cao, Z. H. Yang, W. P. Xiong, Y. Y. Zhou, Y. R. Peng, X. Li, C. Y. Zhou, R. Xu and Y. R. Zhang, *Chem. Eng. J.* 2018, **353**, 126.
- 106 M. Wang, L. Yang, C. Guo, X. Liu, L. He, Y. Song, Q. Zhang, X. Qu, H. Zhang, Z. Zhang and S. Fang, *ChemistrySelect* 2018, **3**, 3664.
- 107 A. S. Yasin, J. Li, N. Wu and T. Musho, *Phys. Chem. Chem. Phys.* 2016, **18**, 12748.
- 108 J. Klinowski, F. A. Almeida Paz, P. Silva and J. Rocha, *Dalton Trans.* 2011, **40**, 321.
- 109 Z. Ni and R. I. Masel, *J. Am. Chem. Soc.* 2006, **128**, 12394.
- 110 J. S. Choi, W. J. Son, J. Kim and W. S. Ahn, *Micropor. Mesopor. Mater.* 2008, **116**, 727.
- 111 T. W. Goh, C. Xiao, R. V. Maligal-Ganesh, X. Li and W. Huang, *Chem. Eng. Sci.* 2015, **124**, 45.
- 112 R. Grau-Crespo, A. Aziz, A. W. Collins, R. Crespo-Otero, N. C. Hernández, L. M. Rodríguez-Albelo, A. R. Ruiz-Salvador, S. Calero and S. Hamad, *Angew. Chem. Int. Ed.* 2016, **55**, 16012.
- 113 R. Navarro Amador, M. Carboni and D. Meyer, *RSC Adv.* 2017, **7**, 195.
- 114 L. Shi, L. Yang, H. Zhang, K. Chang, G. Zhao, T. Kaka and J. Ye, *Appl. Catal. B: Environ.* 2018, **224**, 60.
- 115 K. A. Kovalenko, N. V. Ruban, S. A. Adonin, D. V. Korneev, S. B. Erenburg, S. V. Trubina, K. Kvashnina, M. N. Sokolov and V. P. Fedin, *New J. Chem.* 2017, **41**, 2255.
- 116 H. Li, F. Zhai, D. Gui, X. Wang, C. Wu, D. Zhang, X. Dai, H. Deng, X. Su, J. Diwu, Z. Lin, Z. Chai and S. Wang, *Appl. Catal. B: Environ.* 2019, **254**, 47.
- 117 Y. P. Yuan, L. S. Yin, S. W. Cao, G. S. Xu, C. H. Li and C. Xue, *Appl. Catal. B: Environ.* 2015, **168-169**, 572.
- 118 E. H. Otal, M. L. Kim, M. E. Calvo, L. Karvonen, I. O. Fabregas, C. A. Sierra and J. P. Hinestroza, *Chem. Commun.* 2016, **52**, 6665.
- 119 J. Qin, S. Wang and X. Wang, *Appl. Catal. B: Environ.* 2017, **209**, 476.
- 120 S. Yang, B. Pattengale, E. L. Kovrigin and J. Huang, *ACS Energy Lett.* 2017, **2**, 75.
- 121 T. Zhou, Y. Du, A. Borgna, J. Hong, Y. Wang, J. Han, W. Zhang and R. Xu, *Energy Environ. Sci.* 2013, **6**, 3229.
- 122 C. Wang, K. E. deKrafft and W. Lin, *J. Am. Chem. Soc.* 2012, **134**, 7211.
- 123 S. R. Thakare and S. M. Ramteke, *J. Phys. Chem. Solids* 2018, **116**, 264.
- 124 Q. Liang, M. Zhang, Z. Zhang, C. Liu, S. Xu and Z. Li, *J. Alloys Compd.* 2017, **690**, 123.

- 125 Q. Li, Z. Fan, L. Zhang, Y. Li, C. Chen, R. Zhao and W. Zhu, *J. Solid State Chem.* 2019, **269**, 465.
- 126 L. H. Zhang, Y. Zhu, B. R. Lei, Y. Li, W. Zhu and Q. Li, *Inorg. Chem. Commun.* 2018, **94**, 27.
- 127 X. Han, X. Yang, G. Liu, Z. Li and L. Shao, *Chem. Eng. Res. Des.* 2019, **143**, 90.
- 128 Q. Yang, Q. Xu and H. L. Jiang, *Chem. Soc. Rev.* 2017, **46**, 4774.
- 129 T. Zhang, Y. Jin, Y. Shi, M. Li, J. Li and C. Duan, *Coordin. Chem. Rev.* 2019, **380**, 201.
- 130 D. N. Jiang, P. Xu, H. Wang, G. M. Zeng, D. L. Huang, M. Chen, C. Lai, C. Zhang, J. Wan and W. J. Xue, *Coordin. Chem. Rev.* 2018, **376**, 449.
- 131 X. Fang, Q. Shang, Y. Wang, L. Jiao, T. Yao, Y. Li, Q. Zhang, Y. Luo and H. L. Jiang, *Adv. Mater.* 2018, **30**, 1705112.
- 132 D. Sun and Z. Li, *J. Phys. Chem. C* 2016, **120**, 19744.
- 133 J. D. Xiao, L. Han, J. Luo, S. H. Yu and H. L. Jiang, *Angew. Chem. Int. Ed.* 2018, **57**, 1103.
- 134 D. Li, S. H. Yu and H. L. Jiang, *Adv. Mater.* 2018, **30**, 1707377.
- 135 L. Shen, W. Wu, R. Liang, R. Lin and L. Wu, *Nanoscale* 2013, **5**, 9374.
- 136 S. L. R. Liang, F. Jing, L. Shen, N. Qin, L. Wu, *Appl. Catal. B Environ.* 2015, **176-177**, 240.
- 137 R. Liang, F. Jing, L. Shen, N. Qin and L. Wu, *Nano Res.* 2015, **8**, 3237.
- 138 J. Qiu, L. Yang, M. Li and J. Yao, *Mater. Res. Bull.* 2019, **112**, 297.
- 139 T. Toyao, M. Saito, Y. Horiuchi, K. Mochizuki, M. Iwata, H. Higashimura and M. Matsuoka, *Catal. Sci. Technol.* 2013, **3**, 2092.
- 140 H. Guo, D. Guo, Z. Zheng, W. Weng and J. Chen, *Appl. Organomet. Chem.* 2015, **29**, 618.
- 141 R. M. Abdelhameed, M. M. Simoes, A. M. Silva and J. Rocha, *Chem. Eur. J.* 2015, **21**, 11072.
- 142 W. Zhang, L. Wang and J. Zhang, *Res. Chem. Interm.* 2019,
- 143 Y. Huang, Y. Zhang, X. Chen, D. Wu, Z. Yi and R. Cao, *Chem. Commun.* 2014, **50**, 10115.
- 144 Y. Zhang and S. J. Park, *Chem. Eng. J.* 2019, **369**, 353.
- 145 R. Liang, S. Luo, F. Jing, L. Shen, N. Qin and L. Wu, *Appl. Catal. B: Environ.* 2015, **176-177**, 240.
- 146 J. Zhang, M. Vasei, Y. Sang, H. Liu and J. P. Claverie, *ACS Appl. Mater. Inter.* 2016, **8**, 1903.
- 147 J. S. Lee, K. H. You and C. B. Park, *Adv. Mater.* 2012, **24**, 1084.
- 148 M. Han, S. Zhu, S. Lu, Y. Song, T. Feng, S. Tao, J. Liu and B. Yang, *Nano Today* 2018, **19**, 201.
- 149 Y. Zhang, G. Li, H. Lu, Q. Lv and Z. Sun, *RSC Adv.* 2014, **4**, 7594.
- 150 R. Liang, L. Shen, F. Jing, N. Qin and L. Wu, *ACS Appl. Mater. Inter.* 2015, **7**, 9507.
- 151 C. Yang, X. You, J. Cheng, H. Zheng and Y. Chen, *Appl. Catal. B: Environ.* 2017, **200**, 673.
- 152 T. A. Vu, G. H. Le, H. T. Vu, K. T. Nguyen, T. T. T. Quan, Q. K. Nguyen, H. T. K. Tran, P. T. Dang, L. D. Vu and G. D. Lee, *Mater. Res. Express* 2017, **4**, 035038.
- 153 Y. Wu, H. Luo and H. Wang, *RSC Adv.* 2014, **4**, 40435.
- 154 X. Li, Z. Le, X. Chen, Z. Li, W. Wang, X. Liu, A. Wu, P. Xu and D. Zhang, *Appl. Catal. B: Environ.* 2018, **236**, 501.
- 155 G. W. Q. Wang, X. Liang, X. Dong and X. Zhang, *Appl. Surf. Sci.* 2019, **467-468**, 320.
- 156 L. Shen, L. Huang, S. Liang, R. Liang, N. Qin and L. Wu, *RSC Adv.* 2014, **4**, 2546.
- 157 X. Wei, Y. Wang, Y. Huang and C. Fan, *J. Alloys Compd.* 2019, **802**, 467.
- 158 X. X. Xu, H. Y. Yang, Z. Y. Li, X. X. Liu and X. L. Wang, *Chem. Eur. J.* 2015, **21**, 3821.
- 159 Z. Zhang, T. Zheng, X. Li, J. Xu and H. Zeng, *Part. Part. Syst. Character.* 2016, **33**, 457.
- 160 X. Wu, J. Zhao, L. Wang, M. Han, M. Zhang, H. Wang, H. Huang, Y. Liu and Z. Kang, *Appl. Catal. B: Environ.* 2017, **206**, 501.
- 161 Y. Ma, X. Li, Z. Yang, S. Xu, W. Zhang, Y. Su, N. Hu, W. Lu, J. Feng and Y. Zhang, *Langmuir* 2016, **32**, 9418.
- 162 R. Miao, S. Zhang, J. Liu and Y. Fang, *Chem. Mater.* 2017, **29**, 5957.
- 163 Q. Wang, G. Wang, X. Liang, X. Dong and X. Zhang, *Appl. Surf. Sci.* 2019, **467-468**, 320.
- 164 H. Wang, L. Zhang, Z. Chen, J. Hu, S. Li, Z. Wang, J. Liu and X. Wang, *Chem. Soc. Rev.* 2014, **43**, 5234.

- 165 L. Xie, Z. Yang, W. Xiong, Y. Zhou, J. Cao, Y. Peng, X. Li, C. Zhou, R. Xu and Y. Zhang, *Appl. Surf. Sci.* 2019, **465**, 103.
- 166 Y. Han, C. Bai, L. Zhang, J. Wu, H. Meng, J. Xu, Y. Xu, Z. Liang and X. Zhang, *New J. Chem.* 2018, **42**, 3799.
- 167 A. A. Oladipo, *Process Saf. Environ. Prot.* 2018, **116**, 413.
- 168 H. Yang, X. Liu, X. Song, T. Yang, Z. Liang and C. Fan, *Trans. Nonferrous Met. Soc. China* 2015, **25**, 3987.
- 169 R. Chandra, S. Mukhopadhyay and M. Nath, *Mater. Lett.* 2016, **164**, 571.
- 170 Y. Xia, S. K. Shang, X. R. Zeng, J. Zhou and Y. Y. Li, *Nanomaterials* 2019, **9**, 545.
- 171 Y. Zhang and S. J. Park, *Appl. Catal. B: Environ.* 2019, **240**, 92.
- 172 M. Ciprian, P. Xu, S. Chaemchuen, R. Tu, S. Zhuiykov, P. M. Heynderickx and F. Verpoort, *Micropor. Mesopor. Mater.* 2018, **267**, 185.
- 173 Y. Si, Y. Li, J. Zou, X. Xiong, X. Zeng and J. Zhou, *Materials* 2017, **10**, 1161.
- 174 Y. Si, Y. Li, Y. Xia, S. Shang, X. Xiong, X. Zeng and J. Zhou, *Crystals* 2018, **8**, 432.
- 175 Y. H. Ding, X. L. Zhang, N. Zhang, J. Y. Zhang, R. Zhang, Y. F. Liu and Y. Z. Fang, *Dalton Trans.* 2018, **47**, 684.
- 176 J. Qiu, X. F. Zhang, X. Zhang, Y. Feng, Y. Li, L. Yang, H. Lu and J. Yao, *J. Hazard. Mater.* 2018, **349**, 234.
- 177 R. Panda, S. Rahut and J. K. Basu, *RSC Adv.* 2016, **6**, 80981.
- 178 L. Hu, G. Deng, W. Lu, S. Pang and X. Hu, *Appl. Surf. Sci.* 2017, **410**, 401.
- 179 N. Liu, W. Huang, M. Tang, C. Yin, B. Gao, Z. Li, L. Tang, J. Lei, L. Cui and X. Zhang, *Chem. Eng. J.* 2019, **359**, 254.
- 180 Q. Xia, B. Huang, X. Yuan, H. Wang, Z. Wu, L. Jiang, T. Xiong, J. Zhang, G. Zeng and H. Wang, *J. Colloid Interf. Sci.* 2018, **530**, 481.
- 181 R. Yuan, C. Yue, J. Qiu, F. Liu and A. Li, *Appl. Catal. B: Environ.* 2019, **251**, 229.
- 182 X. Liu, R. Dang, W. Dong, X. Huang, J. Tang, H. Gao and G. Wang, *Appl. Catal. B: Environ.* 2017, **209**, 506.
- 183 X. He, H. Fang, D. J. Gosztola, Z. Jiang, P. Jena and W. N. Wang, *ACS Appl. Mater. Inter.* 2019, **11**, 12516.
- 184 J. Huang, H. Song, C. Chen, Y. Yang, N. Xu, X. Ji, C. Li and J. A. You, *J. Environ. Chem. Eng.* 2017, **5**, 2579.
- 185 M. Ahmad, S. Chen, F. Ye, X. Quan, S. Afzal, H. Yu and X. Zhao, *Appl. Catal. B: Environ.* 2019, **245**, 428.
- 186 J. Zheng and Z. Jiao, *J. Colloid Interf. Sci.* 2017, **488**, 234.
- 187 J. Yang, X. Niu, S. An, W. Chen, J. Wang and W. Liu, *RSC Adv.* 2017, **7**, 2943.
- 188 A. Soheil, K. Elaheh, A. Moghaddam, M. Reza, S. Laura and J. Christoph, *J. Solid. State. Chem.* 2018, **266**, 54.
- 189 L. He, Y. Dong, Y. Zheng, Q. Jia, S. Shan and Y. Zhang, *J. Hazard. Mater.* 2019, **361**, 85.
- 190 Y. Xu, Q. Chen, H. Yang, M. Lv, Q. He, X. Liu and F. Wei, *Mater. Sci. Semicond. Process.* 2015, **36**, 115.
- 191 L. Wang and L. Zan, *Sci. Rep.* 2019, **9**, 4860.
- 192 Z. Sha, H. S. O. Chan and J. Wu, *J. Hazard. Mater.* 2015, **299**, 132.
- 193 Z. Sha, J. Sun, H. S. O. Chan, S. Jaenicke and J. Wu, *ChemPlusChem* 2015, **80**, 1321.
- 194 S. Li, X. Wang, Q. He, Q. Chen, Y. Xu, H. Yang, M. M. Lu, F. Y. Wei and X. T. Liu, *Chin. J. Catal.* 2016, **37**, 367.
- 195 Z. Sha and J. Wu, *RSC Adv.* 2015, **5**, 39592.
- 196 Z. Yang, X. Tong, J. Feng, S. He, M. Fu, X. Niu, T. Zhang, H. Liang, A. Ding and X. Feng, *Chemosphere* 2019, **220**, 98.
- 197 R. Zhang, B. Du, Q. Li, Z. Cao, G. Feng and X. Wang, *Appl. Surf. Sci.* 2019, **466**, 956.
- 198 Q. Zhang, J. Yang, M. Xu, J. Chen, Y. Lou, J. Zhou and L. Cheng, *J. Chem. Technol. Biotechnol.* 2018, **93**, 2710.
- 199 C. Cheng, J. Fang, S. Lu, C. Cen, Y. Chen, L. Ren, W. Feng and Z. Fang, *J. Chem. Technol. Biotechnol.* 2016, **91**, 2785.
- 200 Z. Sha, J. Sun, H. S. On Chan, S. Jaenicke and J. Wu, *RSC Adv.* 2014, **4**, 64977.
- 201 J. Ding, Z. Yang, C. He, X. Tong, Y. Li, X. Niu and H. Zhang, *J. Colloid Interf. Sci.* 2017, **497**, 126.
- 202 B. Liu, X. Liu, J. Liu, C. Feng, Z. Li, C. Li, Y. Gong, L. Pan, S. Xu and C. Sun, *Appl. Catal. B: Environ.* 2018, **226**, 234.
- 203 Q. Liang, S. Cui, C. Liu, S. Xu, C. Yao and Z. Li, *J. Colloid Interf. Sci.* 2018, **524**, 379.
- 204 H. Wang, X. Yuan, Y. Wu, G. Zeng, H. Dong, X. Chen, L. Leng, Z. Wu and L. Peng, *Appl. Catal. B: Environ.* 2016, **186**, 19.
- 205 S. R. Zhu, P. F. Liu, M. K. Wu, W. N. Zhao, G. C. Li, K. Tao, F. Y. Yi and L. Han, *Dalton Trans.* 2016, **45**, 17521.

- 206 L. Han, X. Zhang and D. Wu, *J. Mater. Sci.: Mater. Electron.* 2019, **30**, 3773.
- 207 Q. Hu, J. Di, B. Wang, M. Ji, Y. Chen, J. Xia, H. Li and Y. Zhao, *Appl. Surf. Sci.* 2019, **466**, 525.
- 208 R. M. Abdelhameed, D. M. Tobaldi and M. Karmaoui, *J. Photochem. Photobio. A: Chem.* 2018, **351**, 50.
- 209 N. A. Rodríguez, A. Savateev, M. A. Grela and D. Dontsova, *ACS Appl. Mater. Inter.* 2017, **9**, 22941.
- 210 K. R. Rana, R. K. Singh, V. A. Chhabra, K. H. Kim and A. Deep, *RSC Adv.* 2017, **7**, 29015.
- 211 S. Mosleh, M. R. Rahimi, M. Ghaedi and K. Dashtian, *RSC Adv.* 2016, **6**, 61516.
- 212 S. Mosleh and M. R. Rahimi, *Ultrason. Sonochem.* 2017, **35**, 449.
- 213 H. Ramezanalizadeh and F. Manteghi, *J. Photochem. Photobio. A: Chem.* 2017, **346**, 89.
- 214 H. Ramezanalizadeh and F. Manteghi, *J. Clean. Prod.* 2018, **172**, 2655.
- 215 Y. Liang, R. Shang, J. Lu, L. Liu, J. Hu and W. Cui, *ACS Appl. Mater. Inter.* 2018, **10**, 8758.
- 216 S. R. Zhu, M. K. Wu, W. N. Zhao, P. F. Liu, F. Y. Yi, G. C. Li, K. Tao and L. Han, *Cryst. Growth Des.* 2017, **17**, 2309.
- 217 S. Panneri, M. Thomas, P. Ganguly, B. N. Nair, A. P. Mohamed, K. G. K. Warriar and U. S. Hareesh, *Catal. Sci. Technol.* 2017, **7**, 2118.
- 218 D. Yuan, J. Ding, J. Zhou, L. Wang, H. Wan, W. L. Dai and G. Guan, *J. Alloys Compd.* 2018, **762**, 98.
- 219 X. H. Yi, F. X. Wang, X. D. Du, P. Wang and C. C. Wang, *Appl. Organomet. Chem.* 2019, **33**, e4621.
- 220 D. Guo, R. Wen, M. Liu, H. Guo, J. Chen and W. Weng, *Appl. Organomet. Chem.* 2015, **29**, 690.
- 221 W. Huang, L. Ning, X. Zhang, M. Wu and L. Tang, *Appl. Surf. Sci.* 2017, **425**, 107.
- 222 Y. F. Y. Li, Z. Cao, N. Li, D. Chen, Q. Xu and J. Lu, *Appl. Catal. B: Environ.* 2019, **250**, 150.
- 223 Z. Shao, D. Zhang, C. Su, X. Pu and Y. Geng, *Sep. Purif. Technol.* 2019, **220**, 16.
- 224 S. G. Khasevani and M. R. Gholami, *Inorg. Chem. Commun.* 2019, **102**, 221.
- 225 X. Li, Y. Pi, L. Wu, Q. Xia, J. Wu, Z. Li and J. Xiao, *Appl. Catal. B: Environ.* 2017, **202**, 653.
- 226 J. Hong, C. Chen, F. E. Bedoya, G. H. Kelsall, D. O'Hare and C. Petit, *Catal. Sci. Technol.* 2016, **6**, 5042.
- 227 X. Du, X. Yi, P. Wang, J. Deng and C. C. Wang, *Chin. J. Catal.* 2019, **40**, 70.
- 228 J. Huang, X. B. Zhang, H. Y. Song, C. X. Chen, F. Q. Han and C. C. Wen, *Appl. Surf. Sci.* 2018, **441**, 85.
- 229 Y. Gong, B. Yang, H. Zhang and X. Zhao, *J. Mater. Chem. A* 2018, **6**, 23703.
- 230 B. Liu, Y. Wu, X. Han, J. Lv, J. Zhang and H. Shi, *J Mater Sci: Mater Electron* 2018, **29**, 17591.
- 231 X. Zhang, Y. Yang, W. Huang, Y. Yang, Y. Wang, C. He, N. Liu, M. Wu and L. Tang, *Mater. Res. Bull.* 2018, **99**, 349.
- 232 Y. Zhang, J. Zhou, Q. Feng, X. Chen and Z. Hu, *Chemosphere* 2018, **212**, 523.
- 233 H. Jia, D. Ma, S. Zhong, L. Li, L. Li, L. Xu and B. Li, *Chem. Eng. J.* 2019, **368**, 165.
- 234 H. Wang, X. Yuan, Y. Wu, G. Zeng, X. Chen, L. Leng and H. Li, *Appl. Catal. B: Environ.* 2015, **174-175**, 445.
- 235 R. Abazari, A. R. Mahjoub and G. Salehi, *J. Hazard. Mater.* 2019, **365**, 921.
- 236 D. A. Giannakoudakis, N. A. Travlou, J. Secor and T. J. Bandosz, *Small* 2017, **13**, 1601758.
- 237 D. A. Giannakoudakis, Y. Hu, M. Florent and T. J. Bandosz, *Nanoscale Horiz.* 2017, **2**, 356.
- 238 K. Koh, A. G. Wong-Foy and A. J. Matzger, *Chem. Commun.* 2009, 6162.
- 239 Y. Yoo and H. K. Jeong, *Cryst. Growth Des.* 2010, **10**, 1283.
- 240 T. Fukushima, S. Horike, H. Kobayashi, M. Tsujimoto, S. Isoda, M. L. Foo, Y. Kubota, M. Takata and S. Kitagawa, *J. Am. Chem. Soc.* 2012, **134**, 13341.
- 241 S. Furukawa, K. Hirai, K. Nakagawa, Y. Takashima, R. Matsuda, T. Tsuruoka, M. Kondo, R. Haruki, D. Tanaka, H. Sakamoto, S. Shimomura, O. Sakata and S. Kitagawa, *Angew. Chem. Int. Ed.* 2009, **121**, 1798.
- 242 P. Á. Szilágyi, M. Lutz, J. Gascon, J. Juan-Alcañiz, J. van Esch, F. Kapteijn, H. Geerlings, B. Dam and R. van de Krol, *CrystEngComm* 2013, **15**, 6003.
- 243 T. Y. Luo, C. Liu, X. Y. Gan, P. F. Muldoon, N. A. Diemler, J. E. Millstone and N. L. Rosi, *J. Am. Chem. Soc.* 2019, **141**, 2161.
- 244 A. Knebel, P. Wulfert-Holzmann, S. Friebe, J. Pavel, I. Strauß, A. Mundstock, F. Steinbach and J. Caro, *Chem. Eur. J.*

- 2018, **24**, 5728.
- 245 X. Yang, S. Yuan, L. Zou, H. Drake, Y. Zhang, J. Qin, A. Alsalmeh and H. C. Zhou, *Angew. Chem. Int. Ed.* 2018, **57**, 3927.
- 246 T. Li, J. E. Sullivan and N. L. Rosi, *J. Am. Chem. Soc.* 2013, **135**, 9984.
- 247 N. Zhou, F. Su, C. Guo, L. He, Z. Jia, M. Wang, Q. Jia, Z. Zhang and S. Lu, *Biosens. Bioelectron.* 2019, **123**, 51.
- 248 Y. Gu, Y. Wu, L. Li, W. Chen, F. Li and S. Kitagawa, *Angew. Chem. Int. Ed.* 2017, **56**, 15658.
- 249 G. Jia, L. Liu, L. Zhang, D. Zhang, Y. Wang, X. Cui and W. Zheng, *Appl. Surf. Sci.* 2018, **448**, 254.
- 250 L. Liu, L. Zhang, F. Wang, K. Qi, H. Zhang, X. Cui and W. Zheng, *Nanoscale* 2019, **11**, 7554.
- 251 Y. Liu, A. J. Howarth, J. T. Hupp and O. K. Farha, *Angew. Chem. Int. Ed.* 2015, **54**, 9001.
- 252 S. Abdpour, E. Kowsari and M. R. A. Moghaddam, *J. Solid State Chem.* 2018, **262**, 172.
- 253 H. L. Tian, T. Araya, R. P. Li, Y. F. Fang and Y. P. Huang, *Appl. Catal. B: Environ.* 2019, **254**, 371.
- 254 P. Pachfule, A. Acharjya, J. Roeser, T. Langenhahn, M. Schwarze, R. Schomäcker, A. Thomas and J. Schmidt, *J. Am. Chem. Soc.* 2018, **140**, 1423.
- 255 Y. Zhi, Z. Li, X. Feng, H. Xia, Y. Zhang, Z. Shi, Y. Mu and X. Liu, *J. Mater. Chem. A* 2017, **5**, 22933.
- 256 P. F. Wei, M. Z. Qi, Z. P. Wang, S. Y. Ding, W. Yu, Q. Liu, L. K. Wang, H. Z. Wang, W. K. An and W. Wang, *J. Am. Chem. Soc.* 2018, **140**, 4623.
- 257 Y. Peng, M. Zhao, B. Chen, Z. Zhang, Y. Huang, F. Dai, Z. Lai, X. Cui, C. Tan and H. Zhang, *Adv. Mater.* 2018, **30**, 1705454.
- 258 S. J. He, Q. F. Rong, H. Y. Niu and Y. Q. Cai, *Appl. Catal. B: Environ.* 2019, **247**, 49.
- 259 G. D. Fan, X. M. Zheng, J. Luo, H. P. Peng, H. Lin, M. C. Bao, L. Hong and J. J. Zhou, *Chem. Eng. J.* 2018, **351**, 782.
- 260 J. X. Liu, R. Li, Y. F. Wang, Y. W. Wang, X. C. Zhang and C. M. Fan, *J. Alloys Compd.* 2017, **693**, 543.
- 261 J. Liu, R. Li, Y. Hu, T. Li, Z. Jia, Y. Wang, Y. Wang, X. Zhang and C. Fan, *Appl. Catal. B: Environ.* 2017, **202**, 64.
- 262 T. T. Isimjan, H. Kazemian, S. Rohani and A. K. Ray, *J. Mater. Chem.* 2010, **20**, 10241.
- 263 Q. Liu, C. Zeng, L. Ai, Z. Hao and J. Jiang, *Appl. Catal. B: Environ.* 2018, **224**, 38.
- 264 S. K. Patra, S. Rahut and J. K. Basu, *New J. Chem.* 2018, **42**, 18598.
- 265 W. Huang, C. Jing, X. Zhang, M. Tang, L. Tang, M. Wu and N. Liu, *Chem. Eng. J.* 2018, **349**, 603.
- 266 S. Gao, T. Feng, C. Feng, S. N and C. Wang, *J. Colloid Interf. Sci.* 2016, **466**, 284.
- 267 Z. Yang, X. Xu, X. Liang, C. Lei, Y. Cui, W. Wu, Y. Yang, Z. Zhang and Z. Lei, *Appl. Catal. B: Environ.* 2017, **205**, 42.
- 268 S. Feng, R. Wang, S. Feng, Z. Zhang and L. Mao, *Res. Chem. Interm.* 2018, **45**,
- 269 S. Jalali, M. R. Rahimi, K. Dashtian, M. Ghaedi and S. Mosleh, *Polyhedron* 2019, **166**, 217.
- 270 F. A. Sofi, K. Majid and O. Mehraj, *J. Alloys Compd.* 2018, **737**, 798.
- 271 S. Mosleh, M. R. Rahimi, M. Ghaedi, K. Dashtian, S. Hajati and S. Wang, *Chem. Eng. Process* 2017, **114**, 24.
- 272 X. Yuan, H. Wang, Y. Wu, G. Zeng, X. Chen, L. Leng, Z. Wu and H. Li, *Appl. Organomet. Chem.* 2016, **30**, 289.
- 273 Y. Wu, H. Luo and L. Zhang, *Environ. Sci. Pollut. Res.* 2015, **22**, 17238.
- 274 Y. Chen, J. Li, B. Zhai and Y. Liang, *Colloids Surf. A* 2019, **568**, 429.
- 275 X. Zhao, X. Liu, Z. Zhang, X. Liu and W. Zhang, *RSC Adv.* 2016, **6**, 92011.
- 276 H. U. Rasheed, X. M. Lv, S. Y. Zhang, W. Wei, N. Ullah and J. M. Xie, *Adv. Powder Technol.* 2018, **29**, 3305.
- 277 L. Qin, Z. W. Li, Z. H. Xu, X. W. Guo and G. L. Zhang, *Appl. Catal. B: Environ.* 2015, **179**, 500.
- 278 X. Y. Li, Y. H. Pi, Q. B. Xia, Z. Li and J. Xiao, *Appl. Catal. B: Environ.* 2016, **191**, 192.
- 279 X. S. Wang, C. H. Chen, F. Ichihara, M. Oshikiri, J. Liang, L. Li, Y. Li, H. Song, S. Wang, T. Zhang, Y. B. Huang, R. Cao and J. Ye, *Appl. Catal. B: Environ.* 2019, **253**, 323.
- 280 Y. Zhao, Y. Dong, F. Lu, C. Ju, L. Liu, J. Zhang, B. Zhang and Y. Feng, *J. Mater. Chem. A* 2017, **5**, 15380.
- 281 S. Gholizadeh Khasevani and M. R. Gholami, *Mater. Res. Bull.* 2018, **106**, 93.
- 282 S. Gholizadeh Khasevani, N. Mohaghegh and M. R. Gholami, *New J. Chem.* 2017, **41**, 10390.
- 283 T. Zhou, G. Zhang, H. Zhang, H. Yang, P. Ma, X. Li, X. Qiu and G. Liu, *Catal. Sci. Technol.* 2018, **8**, 2402.



- 284 Y. Chen, B. Y. Zhai, Y. N. Liang, Y. C. Li and J. Li, *J. Solid State Chem.* 2019, **274**, 32.
- 285 F. Wang, Y. T. Zhang, Y. Xu, X. Wang, S. Li, H. Yang, X. Liu and F. Wei, *J. Environ. Chem. Eng.* 2016, **4**, 3364.
- 286 Q. Liang, J. Jin, C. Liu, S. Xu, C. Yao and Z. Li, *Inorg. Chem. Front.* 2018, **5**, 335.
- 287 L. Qian, S. Cui, J. Jin, C. Liu, Song. Xu, C. Yao and Z. Li, *Appl. Surf. Sci.* 2018, **456**, 899.
- 288 S. Mosleh, M. R. Rahimi, M. Ghaedi, K. Dashtian and S. Hajati, *RSC Adv.* 2016, **6**, 63667.
- 289 S. Mosleh, M. R. Rahimi, M. Ghaedi and K. Dashtian, *Ultrason. Sonochem.* 2016, **32**, 387.
- 290 N. Liu, W. Huang, X. Zhang, L. Tang, L. Wang, Y. Wang and M. Wu, *Appl. Catal. B: Environ.* 2018, **221**, 119.
- 291 M. A. Henderson, W. S. Epling, C. H. F. Peden and C. L. Perkins, *J. Phy. Chem. B* 2003, **107**, 534.
- 292 T. Araya, M. Jia, J. Yang, P. Zhao, K. Cai, W. H. Ma and Y. P. Huang, *Appl. Catal. B: Environ.* 2017, **203**, 768.
- 293 T. Araya, C. C. Chen, M. Jia, D. Johnson, R. P. Li and Y. P. Huang, *Opt. Mater.* 2017, **64**, 512.
- 294 W. Guan, X. Gao, G. Ji, Y. Xing, C. Du and Z. Liu, *J. Solid State Chem.* 2017, **255**, 150.
- 295 C. Zhang, L. Ai and J. Jiang, *J. Mater. Chem. A* 2015, **3**, 3074.
- 296 X. Feng, H. Chen and F. Jiang, *J. Colloid Interf. Sci.* 2017, **494**, 32.
- 297 S. Li, J. Cui, X. Wu, X. Zhang, Q. Hu and X. Hou, *J. Hazard. Mater.* 2019, **373**, 408.
- 298 H. Zhao, L. Qian, H. Lv, Y. Wang and G. Zhao, *ChemCatChem* 2015, **7**, 4148.
- 299 S. Kampouri, T. N. Nguyen, M. Spodaryk, R. G. Palgrave, A. Züttel, B. Smit and K. C. Stylianou, *Adv. Fun. Mater.* 2018, **28**, 1806368.